THE EUROPEAN ENERGY RESEARCH ALLIANCE
DESIGN TOOLS FOR OFFSHORE WIND FARM CLUSTER

# D1.3 Benchmark report on wake models at the wind farm scale

*P.-E. Réthoré, K.S. Hansen, R.J. Barthelmie, S.C. Pryor, G. Sieros, J. Prospathopoulos, J.M.L.M. Palma, V.C. Gomes, G. Schepers, P. Stuart, T. Young, J.S. Rodrigo, G.C. Larsen, T.J. Larsen, S. Ott, O. Rathmann, A. Pena, M. Gaumond and C. B. Hasager*

June, 2013

| | |
|---|---|
| Agreement n.: | FP7-ENERGY-2011-1/ n°282797 |
| Duration | January 2012 to June 2015 |
| Co-ordinator: | DTU Wind Energy, Risø Campus, Denmark |

Support by:

SEVENTH FRAMEWORK PROGRAMME

PROPRIETARY RIGHTS STATEMENT
This document contains information, which is proprietary to the “EERA-DTOC” Consortium. Neither this document nor the information contained herein shall be used, duplicated or communicated by any means to any third party, in whole or in parts, except with prior written consent of the “EERA-DTOC” consortium.

## Document information

| | |
|---|---|
| **Document Name:** | Benchmark report on wake models at the wind farm scale |
| **Document Number:** | D1.3 |
| **Author:** | P.-E. Réthoré, K.S. Hansen, R.J. Barthelmie, S.C. Pryor, G. Sieros, J. Prospathopoulos, J.M.L.M. Palma, V.C. Gomes, G. Schepers, P. Stuart, T. Young, J.S. Rodrigo, G.C. Larsen, T.J. Larsen, S. Ott, O. Rathmann, A. Pena, M. Gaumond and C. B. Hasager |
| **Date:** | 30/06/2013 |
| **WP:** | 1 |
| **Task:** | 1.1 |

# TABLE OF CONTENTS

TABLE OF CONTENTS ..... 3

1 EXECUTIVE SUMMARY ..... 4

2 AN OVERVIEW OF SOME OF THE KEY REFERENCES FROM TASK 1.1 ..... 5
2.1 ICOWES Article: Benchmarking Of Wind Farm Scale Wake Models In The EERA_DTOC Project ..... 5
2.2 ICOWES Article: Modeling large offshore wind farms under different atmospheric stability regimes with the Park wake model ..... 5
2.3 Journal article: Atmospheric stability-dependent infinite wind-farm models and the wake-decay coefficient ..... 5
2.4 Technical Report: Wake Model Performance Validation Results For Horns Rev Offshore Wind Farm ..... 5
2.5 Technical Report: Wake Model Performance Validation Results For Lillgrund Offshore Wind Farm ..... 6
2.6 Journal Article: Evaluation of the wind direction uncertainty and its impact on wake modeling at the Horns Rev offshore wind farm ..... 6
2.7 Technical report: Evaluation of a RANS solver performance in offshore wind farms ..... 6
2.8 Journal Article: An Overview Of Data For Wake Model Evaluation In The Virtual Wakes Laboratory ..... 6

3 UNCERTAINTY FROM WAKE MODELS ON NET EFFICIENCY AND RECOMMENDATIONS FOR INDUSTRY USER ..... 8

4 REFERENCES ..... 9

5 APPENDIX: KEY REFERENCES FROM THE TASK ..... 10

# 1 EXECUTIVE SUMMARY

This report is a short summary of the activities done in the task T1.1 and an introduction to some of the articles and reports produced for the task 1.1.

Task 1.1 focuses on benchmarking the existing wind farm scale wake models of the EERA-DTOC partners. The ultimate goal of this task is to provide guidelines for the industry users on which model to use in a specific context and how to quantify the uncertainty of the results produced by the wind farm flow models. In order to draw this conclusion two benchmark campaigns on two different Danish offshore wind farms (Horns Rev and Lillgrund) were carried out in close collaboration with another international collaborative project the IEA-Task 31: WakeBench. The IEA-Task 31 has many similar goals as the Task 1.1 of EERA-DTOC, with a wider scope (also including wind farm in complex terrain, and in the vicinity of forest) and a wider range of participants (over 60 participants from various countries all over the world) that runs from 2012 to 2014. The purpose of the IEA-Task 31 is to reach an international consensus and establish guidelines on operation of wind farm flow models. Most participants in EERA-DTOC T1.1 are also participating in the IEA-Task 31, including CENER, which is leading the IEA-Task 31 and DTU, who processed the two common offshore wind farm benchmarking campaigns between the two projects. This gave EERA-DTOC a key position within IEA-Task 31 to influence the offshore benchmarks definitions and which metrics to use in the benchmark. It also provided an opportunity to EERA-DTOC participants to use datasets from offshore wind farms that are owned by companies that are not partners of EERA-DTOC (DONG Energy: Horns Rev and Vattenfall: Lillgrund).

The results of the two benchmarking campaigns indicate that many of the models significantly overpredict the maximum wake losses in comparison with the measurements. This is particularly the case for the CFD models that simulate the wake shape exactly, and less so for more empirically-based models. However, recent findings obtained within this project indicate that the discrepancy between the measurements and model results could be caused by a high uncertainty in the measurement of the wind direction. This high uncertainty causes the analysis of the measured data to produce artificially low power losses in the wake center because of direction variability. This finding challenges the traditional methods of comparing wind farm SCADA measurements with wind farm flow models. It has created a considerable amount of discussion within the wind farm flow modeler community, and this has been identified as one of the major tasks to be addressed within the IEA-Task 31: WakeBench project.

Because of this situation, we consider that it is necessary to reach some sort of an international consensus on how to properly validate wind farm flow models with measurements with high degree of uncertainty. We therefore recommend to the industry users to follow the guidelines planned to be established within the IEA-Task 31: WakeBench project.

# 2 AN OVERVIEW OF SOME OF THE KEY REFERENCES FROM TASK 1.1

## 2.1 ICOWES Article: Benchmarking Of Wind Farm Scale Wake Models In The EERA_DTOC Project

This article (Rethoré et al. 2013), presented at the ICOWES 2013 conference focuses on presenting the different wind farm wake models with their specific sub-model assumptions, the Horns Rev wind farm, the challenges of creating a reliable reference dataset for the comparison with the wind farm wake models, the different test cases and finally a discussion of the results. The wind farm scale wake models represent the current state of the art ranging from industry standard more highly parameterized models that have minimal computing requirements (WAsP is the classic example) through linearized CFD models such as FUGA to actuator disk models such as RANS that are more computationally demanding. As a general trend, most models seem to over-predict the wake deficit for small wind direction averaging window, and have a closer prediction to the observations with a larger direction-averaging window. This is consistent with the result that the maximum velocity deficit is under-represented in the observations because of directional variability. As the direction-averaging window increases, the velocity deficit decreases because more of the wake width (that is approximately Gaussian in shape) is incorporated.

## 2.2 ICOWES Article: Modeling large offshore wind farms under different atmospheric stability regimes with the Park wake model

This paper (Peña et al. 2013), presented at the ICOWES 2013 conference, illustrates an evaluation of a modified version of the Park wake model against data of the Horns Rev I wind farm classified into four different stability conditions. The simulations are post-processed to account for some of the wind direction uncertainty and compared to the observations they show good agreement. Although the wind conditions under the different stability regimes are different, the trend is that the power deficits will be higher under stable compared to unstable conditions.

## 2.3 Journal article: Atmospheric stability-dependent infinite wind-farm models and the wake-decay coefficient

This peer-reviewed paper in press (Peña and Rathmann 2013) extends the infinite wind farm boundary layer model of Frandsen to account for stability and the model is compared to other boundary layer and wake engineering models. All models show a similar behavior for the wind speed reduction under a variety of surface roughness values, turbine separations and wind speeds. The dependency of the model on stability is much higher than on roughness. The wake decay coefficient of the engineering model is also found to be highly dependent on stability, roughness, and turbine separation.

## 2.4 Technical Report: Wake Model Performance Validation Results For Horns Rev Offshore Wind Farm

This technical report (Hansen 2013a) presents the results from the Horns Rev wind farm benchmark campaign. The description of the benchmark follows closely the benchmark organized in the international project IEA-Task 31: WakeBench. Five individual benchmarks were organized based on an extensive, quality-controlled dataset from Horns Rev; flow sector variation, atmospheric stratification, turbulence intensity, turbine spacing and park efficiency. This represents the most comprehensive set of benchmarking as yet undertaken for wake model evaluation. A total of 11 models participated in the benchmarking.

## 2.5 Technical Report: Wake Model Performance Validation Results For Lillgrund Offshore Wind Farm

This technical report presents the results from the Lillgrund wind farm benchmark campaign (Hansen 2013b). The description of the benchmark is following closely the benchmark organized in the international project IEA-Task 31: WakeBench and was presented at the IEA Wakebench meeting in July. The advantages of the Lillgrund test cases are the close spacing of the turbines (3.2-4.2 rotor diameters) and the row with missing turbines providing an extension of the turbine spacing available for wake model evaluation at Horns Rev.

## 2.6 Journal Article: Evaluation of the wind direction uncertainty and its impact on wake modeling at the Horns Rev offshore wind farm

During the project course we identified the impact of the wind direction uncertainty on the data processing quality of the wind farm SCADA measurements. The main issue is that the uncertainty in wind direction artificially reduces the wind farm wake effect by smearing the maximum wake deficits across a wider range of wind directions than the 'true' centerline of the velocity deficit. The wind direction uncertainty arises from different sources, such as the wind direction sensor accuracy, and the time and space variability of the wind direction. The result of this analysis is that traditional statistical methods used until now to process the wind farm SCADA data are not adapted to extract accurately the signal from the noise. The approach investigated in the published peer-reviewed article (Gaumond et al. 2013) is to instead of attempting to remove the noise (e.g. the wind direction uncertainty), trying to propagate this uncertainty through the wake models to quantify how this uncertainty impact the performance of the wind farm wake model in comparison with the measurements. This method yields promising results that should be investigated further in the parallel running project IEA-Task 31: WakeBench in order to establish an international agreement on how to deal with this issue.

## 2.7 Technical report: Evaluation of a RANS solver performance in offshore wind farms

This technical report (Prospathopoulos et al, 2013) evaluates the performance of the CRES-flowNS RANS solver in modeling large wind farms through the benchmark studies for the Horns Rev and Lillgrund wind farms. The comparison indicates that predictions significantly overestimate the power deficit when the wind sector is narrow (*±2.5°*). As the size of the sector increases the agreement between predictions and measurements becomes better and for the wide sector of *±15°* it can be considered quite satisfactory, even in the cases of incomplete wind turbine rows. The systematic over-prediction for narrow sectors raises the question if the uncertainty in the measurement of the wind direction produces artificially low power losses in the wake center. The park efficiency of the Horns Rev wind farm for the whole range of wind directions (*0-360°*) was well estimated using the amended GCL model calibrated with the CRES-flowNS predictions in three wind directions. Calibration was made in the sense that the maximum velocity deficit approach was used for sectors centered in the directions of the maximum shadowing between the wind turbines.

## 2.8 Journal Article: An Overview Of Data For Wake Model Evaluation In The Virtual Wakes Laboratory

This peer-reviewed published paper ((Barthelmie; Pryor 2013) describes an open access web resource that contains a variety of offshore wind turbine wake data including time series/SCADA data from the small offshore wind farms at Vindeby and Middelgrunden and some wake case studies from Horns Rev and Nysted. It also describes some of the advantages and disadvantages of different measurement methods for studying wakes. In agreement with the articles described above, it is clear that two significant issues remain relating to wake studies that make the benchmarking difficult. The first is the small signal-to-noise ratio of wind speed and turbulence

measured in wind turbine wakes. The second is the need for multiple metrics to cover a number of wake characteristics including the wake width, the variability of power in a row of turbines under a range of conditions and the total power out of a wind farm by direction or the overall efficiency.

# 3 UNCERTAINTY FROM WAKE MODELS ON NET EFFICIENCY AND RECOMMENDATIONS FOR INDUSTRY USER

The benchmark results are inconclusive on which model performs best because of the high degree of noise in the measurement datasets. More work is needed to be able to fairly compare the models with the measurements. Two directions will be investigated in the parallel international project IEA-task 31: WakeBench:

- Moving towards more sophisticated noise filtering data processing methods to extract the wake signal from the data noise. Such method could for instance be based on Bayesian data mining approaches.
- Investigating more systematically the effect of the propagation of the input uncertainties (e.g. the wind direction uncertainty) on the power production of the wind turbines and the wind farm in general, following the direction drafted by (Gaumond et al. 2013).

At the time of writing this report, our best attempt to model the uncertainty of the wake models could be to estimate the ensemble spread of the different wake model tested. In this sense, the distribution of the model gives us a confidence interval for the wind farm power production. There is currently an ongoing effort for establishing a consistent standard method for estimating the uncertainty quantification of wind farm flow models, in which the EERA-DTOC project is centrally involved. The IEA-Task 31 will be completed before the end of EERA-DTOC. Our recommendations for the industry user is therefore to follow closely the conclusions of the international project IEA-Task 31: WakeBench.

Concerning the question of the complexity of the model needed to perform an adequate prediction, the benchmark results do not seems to favor particularly the full CFD RANS wake models. While they produce some very acceptable results in most benchmark test cases, they have not distinguished themselves significantly better than the other, much less computationally expensive, wind farm flow models. Until a method has been established to compare the models with the wind farm measurements in a robust and consistent way, we have no direct conclusive evidence to justify a preference for any individual model or any particular group of models.

# 4 REFERENCES


Barthelmie, R. J., and S. C. Pryor, 2013: Wake model evaluation using data from the Virtual Wakes Laboratory. *Applied Energy*, **104,** 834-844.

Gaumond, M., P. E. Réthoré, S. Ott, A. Peña, A. Bechmann, and K. S. Hansen, 2013: Evaluation of the wind direction uncertainty and its impact on wake modeling at the Horns Rev offshore wind farm. *Wind Energy*, n/a-n/a.

Hansen, K. S., 2013a: WP1 wake model performance validation results for Horns Rev offshore wind farm, 24 pp.

——, 2013b: WP1 wake model performance validation results for Lillgrund offshore wind farm, In progress pp.

Pena, A., Réthoré, P.-E., & Rathmann, O. 2013: Modeling large offshore wind farms under different atmospheric stability regimes with the Park wake model. *Proceedings of the 2013 International Conference on Aerodynamics of Offshore Wind Energy Systems and Wakes (ICOWES2013), Lyngby, June 2013*

Peña, A., & Rathmann, O. 2013: Atmospheric stability-dependent infinite wind-farm models and the wake-decay coefficient. Wind Energy. doi:10.1002/we

Prospathopoulos, J., Sieros, G., & Chaviaropoulos, P. 2013: Evaluation of a RANS solver performance in offshore wind farms . (pp. 1–27).

Rethoré, P. E., and Coauthors, 2013: Benchmarking of wind farm scale wake models in the EERA-DTOC project. *Proceedings of the 2013 International Conference on Aerodynamics of Offshore Wind Energy Systems and Wakes (ICOWES2013), Lyngby, June 2013*, 38-52.

# 5 APPENDIX: KEY REFERENCES FROM THE TASK

# BENCHMARKING OF WIND FARM SCALE WAKE MODELS IN THE EERA - DTOC PROJECT

**P.-E. Réthoré[1], K.S. Hansen[1], R.J. Barthelmie[2], S.C. Pryor[2], G. Sieros[5], J. Prospathopoulos[5], J.M.L.M. Palma[4], V.C. Gomes[4], G. Schepers[3], P. Stuart[6], T. Young[6], J.S. Rodrigo[7], G.C. Larsen[1], T.J. Larsen[1], S. Ott[1], O. Rathmann[1], A. Peña[1], M. Gaumond[1] and C. B. Hasager[1]**

[1]DTU, Wind Energy, Denmark, pire@dtu.dk
[2]Indiana University, Department of Geological Sciences, USA
[3]ECN, The Netherland, [4]University of Porto, Portugal
[5]CRES, Greece, [6]RES, United Kingdom, [7]CENER, Spain

## ABSTRACT

Designing offshore wind farms next to existing or planned wind farm clusters has recently become a common practice in the North Sea. These types of projects face unprecedented challenges in term of wind energy siting. The currently ongoing European project FP7 EERA - DTOC (Design Tool for Offshore wind farm Clusters) is aiming at providing a new type of model work-flow to address this issue. The wake modeling part of the EERA - DTOC project is to improve the fundamental understanding of wind turbine wakes and modeling. One of these challenges is to create a new kind of wake modeling work-flow to combine wind farm (micro) and cluster (meso) scale wake models. For this purpose, a benchmark campaign is organized on the existing wind farm wake models available within the project, in order to identify which model would be the most appropriate for this coupling. A number of standardized wake cases for large offshore wind farms will be analyzed, which provide a reasonable range of conditions likely to be experienced in offshore wind farms. The systematic evaluation is based upon high - quality input data that is selected in the sister project IEA - Task 31 “WakeBench”.

## INTRODUCTION

With the large offshore wind farms becoming common practice in Northern Europe, the need for reliable wind farm wake models has never been as critical as today. There exists many different

types of wind farm wake models that have been developed during the last three decades, some more complex than others. The wind industry is now to routinely calculating wind farms annual energy production (AEP) using more and more complex wind farm wake models. For instance, running non-linear Reynolds Averaged Navier-Stokes Computational Fluid Dynamics (CFD) actuator disc model has become practical for most medium size companies. In parallel, the amount data and understanding of the wind farm power production has increased significantly during the last 5 years.

The EERA-DTOC project (European Energy Research Alliance - Design Tool for Offshore wind farm Clusters) is focusing on providing a tool to design wind farm clusters, which is a combination of several offshore wind farms. An important element in this tool will be the wind farm annual production estimate, which will rely on one or several state of the art wind farm wake models. The different partners in the project have developed over the years many different offshore wind farm wake models that could be (one of) the potential candidate(s) to be implemented in the EERA-DTOC software. In order to select the right wake models a series of benchmarks are currently underway in collaboration with the IEA-Task 31 ”WakeBench” project.

While previous offshore wind farm wake benchmark comparisons have been carried out during the past decade in the ENDOW project [19] and UpWind project [18], the new and refined models available for the industry combined with the better understanding and refined data of the wind farm SCADA make it relevant now to initiate a new benchmark based on the Horns Rev wind farm within the EERA-DTOC project.

This article will focus on presenting the different models with their specific sub-model assumptions, the Horns Rev wind farm, the challenges of creating a reliable reference dataset for the comparison with the wind farm wake models, the different test cases and finally a discussion of the results.

## WAKE MODELS

The wind farm wake models present in the EERA-DTOC project are presented in tb. 1.

- **SCADA** is the processed wind farm data to be compared with the other wind farm wake models. Wind farm SCADA data are not usually referred in the literature as a model result. However, considering the amount of assumptions and processing methods that have to be applied in order to produce comparable results with a wind farm wake model, a processed SCADA data should in all fairness be treated as a model result. This point is further detailed in the following section.

- **Ainslie** is an eddy-viscosity wake model developed by RES-LTD [5-6] based on the original Ainslie model [8].

- **FarmFlow** is a parabolized $k$-$\varepsilon$ actuator disc CFD model tailored for offshore wake simulation developed by ECN, based on the original UPM wind farm wake model from Crespo [9] combined with a vortex wake model in the close wake.

- **RANS** is an elliptic $k$-$\varepsilon$ actuator disc CFD model tailored for offshore wake simulation developed by Porto University.
- **CRESflowNS** is an elliptic $k$-$\omega$ actuator disc CFD model tailored for offshore wake simulation developed by CRES [13-14].
- **WAsP/NOJ** is the PARK wake model of WAsP commercial software developed by DTU [10] and based on the original wake model from N.O. Jensen [11].
- **NOJ** is the original N.O Jensen model [11], using the mozaic tile methode of Rathmann [21].
- **DWM** is the Dynamic Wake Meandering model developed by DTU [16-17]. This model is the only dynamic model presented in this paper.
- **GCL** is the G.C. Larsen eddy-viscosity wake model v2009 developed by DTU [15].
- **FUGA** is a linearized actuator disc eddy-viscosity CFD model for offshore wind farm wake developed by DTU [12].

The wind farm wake models compared in this work can be categorized in different ways according to their sub-model assumptions. The sub-models considered in this analysis are:

- Inflow model: How the inflow wind speed is described
  - Log law: The log law is used to create the inflow condition, based on the sea roughness, the hub height and hub wind speed.
  - Homogeneous: The inflow is assumed to be homogeneous. Only the hub wind speed is needed.
  - TI: The turbulence intensity is needed.
  - Stability: The inflow conditions are dependent of atmospheric parameters
  - Mann: The inflow is generated through the Mann turbulence model. It can also be tuned to generate different inflow stability conditions and turbulence intensities.
- Hub wind speed model: How the wind speeds generated by the wake model are combined into an input to the wind turbine model. Here the number of points are indicated as a reference for how the turbines take into account the inflow partial wakes. The NOJ model is using a mosaic tile approach, weighting the wake wind speed with the intersectional area between the rotor and the upstream wake deficits.
- Wind turbine model: How the power and thrust are calculated:
  - HAWC2 is an aero-elastic model developed at DTU [7]
  - PTC: The Power and Thrust coefficient Curves, that takes the free-stream wind speed as a reference. Note that an additional method is required when used in combination with an elliptic CFD code in order to estimate this free-stream wind speed in wake conditions. This additional method is not considered in the present analysis.

Table 1: Sub-models assumptions

| Institute | Model Name | Inflow | Hub WS | Turbine | Wake acc | Wake flow |
|---|---|---|---|---|---|---|
| DTU WE | SCADA | Processed wind farm SCADA measurements | | | | |
| DTU WE | FUGA | Log law | 7P | PTC | Linear | FUGA |
| DTU WE | GCL | Log law+TI | 16P | PTC | Linear | GCL |
| DTU WE | DWM | Mann | $>$ 100P | HAWC2 | Max. | DWM |
| DTU WE | NOJ | Homog. | Mosaic | PTC | RSS | NOJ |
| Indiana Uni | WAsP/NOJ | Homog. | Mosaic | PTC | RSS | NOJ+GPR |
| RES-LTD | Ainslie | Homog.+TI | 1P | PTC | ARL | Ainslie+GPR |
| CRES | CRESflowNS | Log law | 1P | PTC | Elliptic $k$-$\omega$ | |
| Porto Uni | RANS | Log law | 1P | PTC | Elliptic $k$-$\varepsilon$ | |
| ECN WE | FarmFlow | Stability | 1P | PTC | Vortex + Parabolic $k$-$\varepsilon$ | |

- Wake accumulation model: How the wake contributions are accumulated
  - Linear: add the velocity deficits.
  - RSS: Root-Sum-Square (i.e. Quadratic).
  - $k$-$\omega$ or $k$-$\varepsilon$ : The accumulation is done by solving the Reynolds Averaged Navier-Stokes equations.
  - Maximum: The maximum wake deficit is used.
  - ARL: Average RSS and Linear velocity deficits.
- Wake flow model: How the wake of one or several wind turbines is calculated. Each model has a different way to solve the momentum and mass flow conservation equation and to account for the inflow and wake generated turbulence. The CFD type models account directly for the ground plane through the Navier-Stokes equations (i.e. FUGA, RANS, CRESflowNS, FarmFlow); some use a Ground Plane Reflection (GPR) method (i.e. Ainslie, WAsP/NOJ); finally, some do not account for the ground surface (i.e. NOJ, GCL and DWM).

## DATA PRESENTATION AND ANALYSIS

### Horns Rev Wind Farm

The Horns Rev wind farm (HR) has a shared ownership by Vattenfall AB (60%) and DONG Energy AS (40%). It is located 14 km from the west coast of Denmark, with a water depth of 6-14 m. The wind farm has a rated capacity of 160 MW comprising 80 wind turbines, which

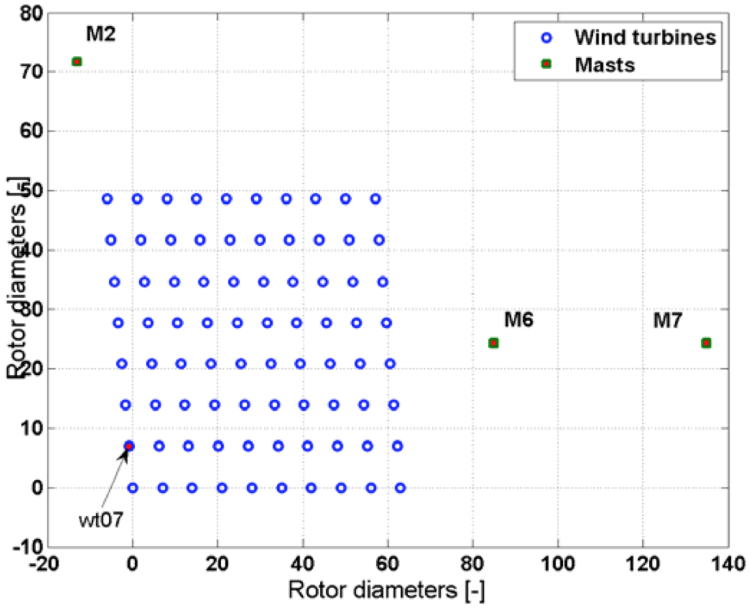


Figure 1: Horns Rev wind farm layout

are arranged in a regular array of 8 by 10 turbines, with a spacing of 560 m in both directions covering an area of 5x3.8 km2. The layout of the wind farm, fig. 1, is not completely rectangular, while the direction of the N-S columns is 353°. The wind turbines are installed with an internal spacing along the main directions of 7D. The diagonal wind turbine spacing is either 9.4 D or 10.4 D. Fig. 1 illustrates the location of the three offshore meteorological masts associated with the wind farm. Mast M2, with a height of 62m, was installed prior to the wind farm installation to document the wind conditions. Two identical masts M6 and M7 were installed as part of the Horns Rev wind farm wake measurements program with a height equal to the hub height of 70m. The wind farm comprises VESTAS V80 turbines, which are 2 MW pitch controlled, variable speed wind turbines with a diameter of 80 m and 70 m hub height. The wind farm has been in operation since 2004 and the SCADA statistics from 2005 – 2007 is available for the wake analysis [1].

The dataset for the current wake analysis was limited to three years, from 2005 to 2007, and includes the SCADA data from the 80 wind turbines and the two downstream wake masts (M6 & M7). Due to the local wind rose, the wake analysis shall be concentrated to westerly and easterly inflow sectors centered at 270° and 90° respectively. Because M6 & M7 are located inside the wind farm wake for the 270° sector, a flow reference has been establish based on wt07 (located in the most western row of the wind farm) in terms of wind speed derived from electrical power and wind direction derived from the calibrated wind turbine yaw position. For the western flow sector, the power curve of wt07 has been validated with wind speed measurements from M2, 62 m level [1]. None of the wind turbine yaw position sensors have been calibrated while these are not used in the wind turbine control, but the yaw position offset for wt07 has been calibrated

and found to be constant during the period, according to the guidelines in [2]. The estimated uncertainty of the wind direction is 5°. For the eastern flow sector, the measured wind speed and wind directions are recorded at 70 m level on either M6/M7.

### Definition of power deficit

For westerly inflow, the power deficit is determined with respect to the reference wt07:

$$\text{Power Deficit} = \frac{P_{\text{wt07}} - P_{\text{wt}}}{P_{\text{wt07}}} \tag{1}$$

For easterly inflow, the power deficit is determined with respect to the reference wt95:

$$\text{Power Deficit} = \frac{P_{\text{wt95}} - P_{\text{wt}}}{P_{\text{wt95}}} \tag{2}$$

### Definition of the error bars

In the plots presented in this article, the error bars on the SCADA plots are the standard uncertainty defined as

$$u = \frac{\sigma}{\sqrt{n}}, \tag{3}$$

with $\sigma$ the standard deviation and $n$ the number of 10-minute data points available for doing the averaging. Note that this value quantifies the level of confidence in the statistical representativity of the averaging, and not the amount of data spreading.

### Data analysis

When looking at processed wind farm SCADA data it is quite important to keep in mind that it is the result of a number of assumptions and processing methods. For instance, fig. 2 illustrates the difference between three processing methods over the same test case: the single wake power deficit between two turbines (wt07 & wt17) in aligned in westerly inflow. All the curves are using the same data sample (2005-2009) but different wind direction sensors (the nacelle position of wind turbine wt07 (NP07) and the mast M7 wind vane), while the curve called we.512_ref is presenting the results using NP07 from another data sample, when the inflow wind was with stable stratification. The mast M7, as it can be seen in fig. 1 is located at more than 10km from the wind turbines wt07 and wt17. By using its wind vane as the sorting sensor, we make the assumption that the wind direction is the same over the distance of 10km. Because of the wind direction spatial/temporal variability, the further away the wind direction is measured, and the less likely this assumption is correct, which introduces an uncertainty in the wind direction correlated with the distance from the wind direction sensor to the wind turbine of interest. As discussed in [4], when considering ensemble average wake deficit data, an uncertainty in wind direction can have the same effect as introducing more partial wake and free wake cases into the ensemble average. So choosing M7 over a closer wind direction sensor, like NP07, gives an artificially lower wake maximum deficit.

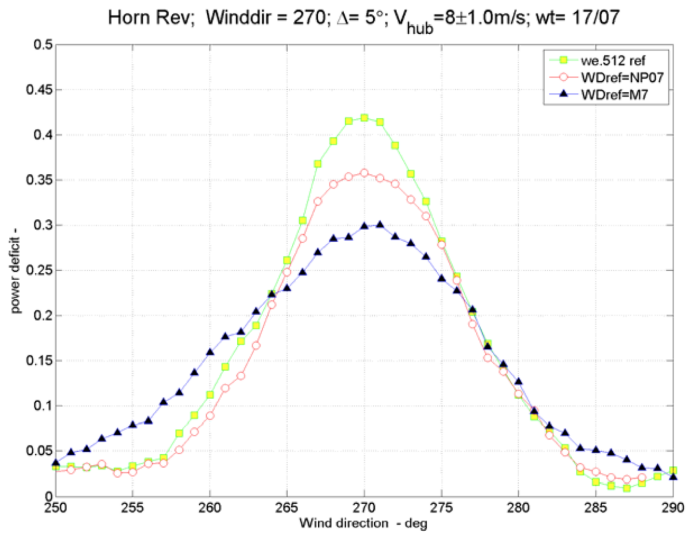


Figure 2: Wind turbine wake deficit using different inflow wind direction sensors (NP07 and M7). The single wakes are compared with a similar data presented in a reference article (we.512 ref).

The effect of wind direction spatial/temporal variability can also be seen by looking at the power deficit along different rows of wind turbines. In fig. 3, the wind direction is measured at the first turbine in the row 7. As the spatial/temporal variability is the lowest for the row 7, its power deficit is also the highest. The further away the rows are from the wind direction sensor, and the smaller the wake deficit appears to be. By taking the average of all the rows of wind turbines, the averaged line also have an artificially lower wake deficit compared with the row 7.

Even though the wind direction sensor is the closest possible, other sources of wind direction uncertainty can have a similar effect as the spatial/temporal variability over the processed wake data. Fig. 4 illustrates the probability density distribution of the power deficit along row 7 with a narrow wind direction angle bin. The results show that there is still a quite large spread of the power deficit, even though we saw previously that the results are better than in the other rows, or using another source of wind direction. Other unmeasured parameters, such as the large scale turbulence (with a time scale larger than the 10-minute averaging period) or the wind turbine yaw misalignment compared to the inflow wind direction, could introduce an uncertainty in wind direction that could cause these sort of spreading effects. Furthermore, the sub-10-minute inflow turbulence should cause a natural wake meandering of the wind turbines wake, which could also create this spreading effect. However, the wake meandering should be partially accounted for by the wake models, so it is quite difficult to dissociate the natural from the artificial spreading seen in the measurements.

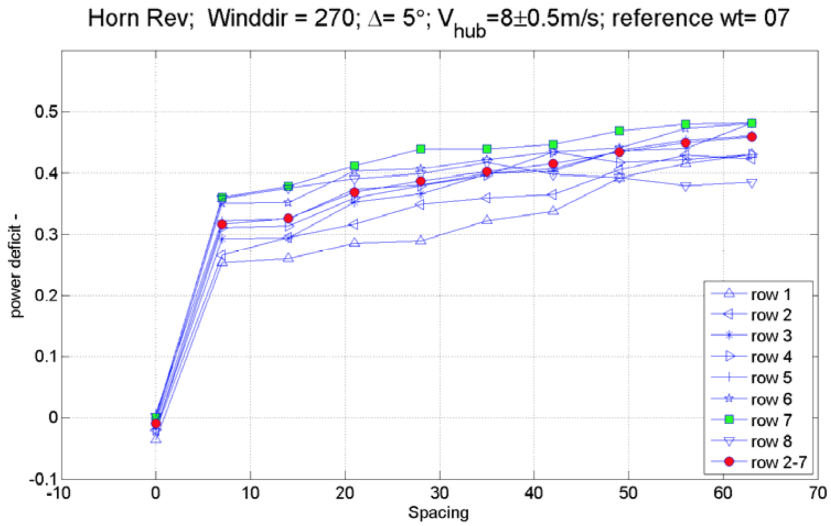


Figure 3: The power deficit along different lines of wind turbine in the westerly wind direction

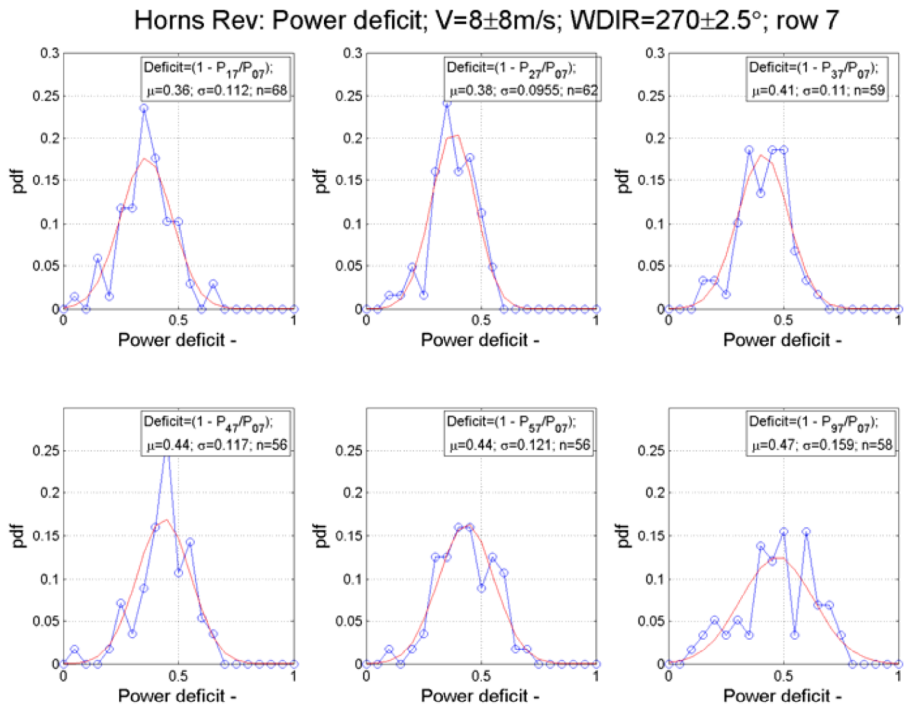


Figure 4: The probability distribution of the power deficit along the row 7.

## RESULTS

This article focuses on three benchmark test cases analyzed in the EERA-DTOC and IEA-Task 31 WakeBench projects. The first one is the single wake power deficit test case, the second one is the power deficit along a row of wind turbines for different inflow wind direction bins and the third one is the maximum power deficit, between two turbines, at different downstream distance as a function of the inflow turbulence intensity.

## Single wake power deficit test case

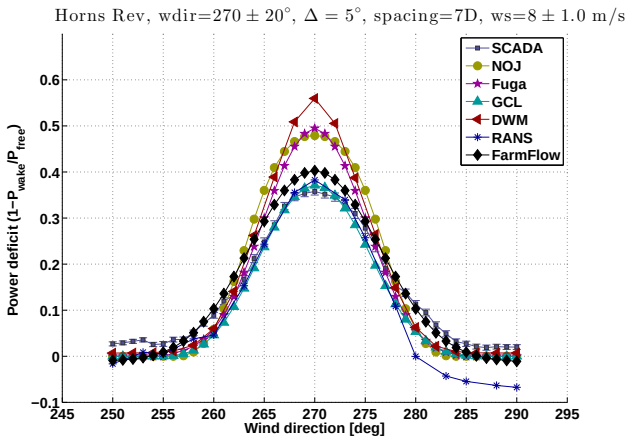


Figure 5: Single wake power deficit between pairs of wind turbines with a 5°averaging window.

The power deficit between wt17 and wt07 in the 270° wind direction, with an averaging window of 5° is illustrated in fig. 5. The wind direction is measured using the nacelle position of wt7 (NP07). The wind speed is measured using an inversed power curve using the power production of the first wind turbine in each row. When directly aligned in 270°, the wind turbines have a spacing of 7 rotor diameters.

GCL, RANS and FarmFlow seem to match the closest the SCADA wake deficit shape, while the other ones seem to over-predict the wake deficit. In the central part of the wake. The RANS model has an asymmetry on the right side that seems to indicate a speed up of the flow. This effect is not visible in the SCADA data.

Note that the SCADA point at 270° corresponds to the probability distribution data presented in top left fig. 4. This shows that even though the error bars are quite small (i.e the standard uncertainty is small), all the wake models are still within the SCADA measurement spreading.

## Power deficit along a row of turbines

The power deficit between wt07 and the downstream turbines in row7 in the 270° wind direction, with an averaging window of $\Delta = 5°$, 15°, and 30° is illustrated in fig. 6, 7 and 8. The wind direction is measured using the nacelle position of wt07 (NP07). The wind speed is measured

using an inversed power curve using the power production of wt07. When directly aligned in 270°, the wind turbines have a spacing of 7 rotor diameters.

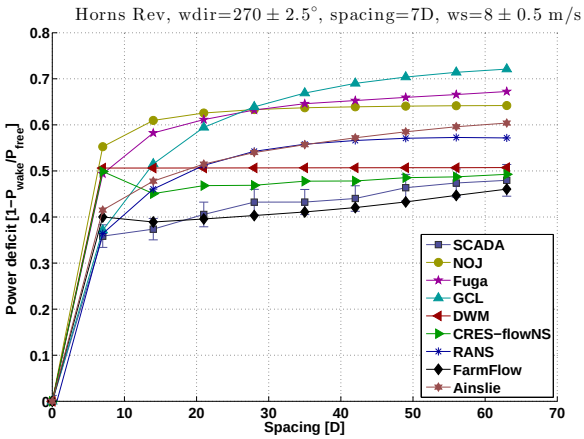


Figure 6: Power deficit along a row of turbine with and inflow wind direction bin of $\Delta = 5°$

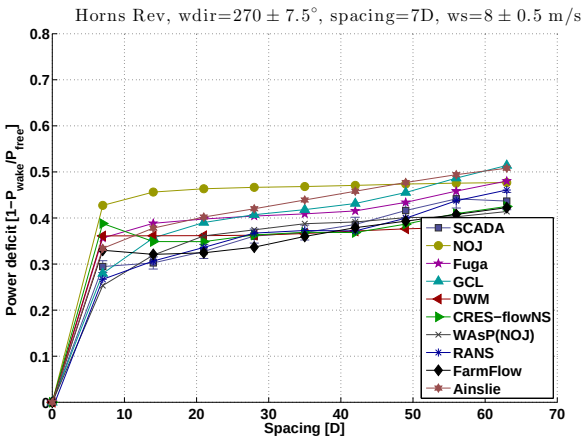


Figure 7: Power deficit along a row of turbine with and inflow wind direction bin of $\Delta = 15°$

As a general trend, most models seem to over-predict the wake deficit for small wind direction averaging window ($\Delta$), and have a closer prediction to the largest $\Delta$. Some of the models, like GCL and RANS have a close estimate of the first turbine downstream, and then seem to deviate gradually from the SCADA points for $\Delta = 5°$ (fig. 6). In the three $\Delta$s, FarmFlow seems to consistently match closely the shape of the SCADA points. Most models, except NOJ, WAsP/NOJ and DWM, seem to be very close to the SCADA point shape in $\Delta = 30°$ (fig. 8).

Note that the SCADA points with an averaging window of 5° fig. 6 corresponds to the

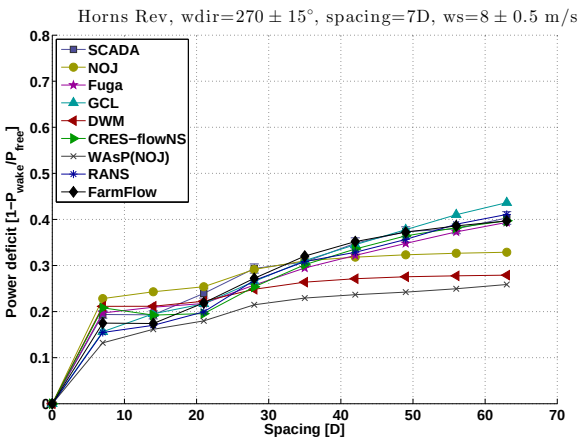


Figure 8: Power deficit along a row of turbine with and inflow wind direction bin of $\Delta = 30°$

probability distribution data plots in fig. 4. This shows that even though the error bars are quite small (i.e the standard uncertainty is small), all the wake models are still within the SCADA measurement spreading.

## Maximum power deficit for different inflow turbulence intensity

The maximum power deficit between two turbines for different inflow turbulence intensity is illustrated at 7 rotor diameters (fig. 9) ad 10.4 rotor diameters (fig. 10).

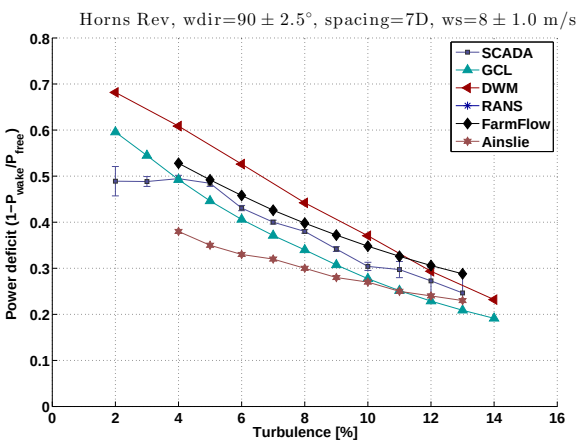


Figure 9: Maximum power deficit for different inflow turbulence intensity and a wind turbine spacing of 7 rotor diameters

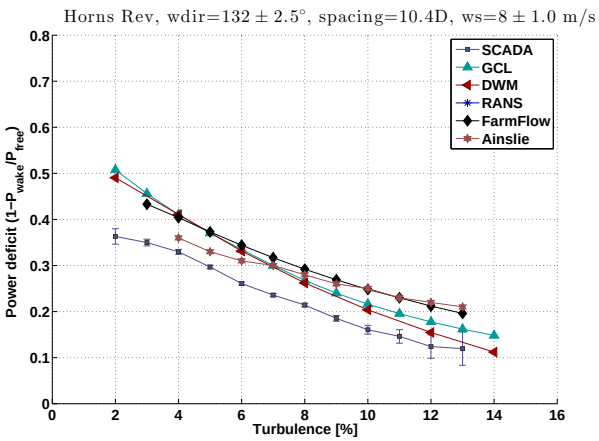


Figure 10: Maximum power deficit for different inflow turbulence intensity and a wind turbine spacing of 10.4 rotor diameters

Most models seem to capture the trend correctly.All the models have a tendency to over-predict the maximum wake deficit at 10.4D, even though some of the models (e.g. GCL and Ainslie) are under-predicting the wake deficit at 7D. There does not seem to be a model clearly better than the other ones in this benchmark.

## DISCUSSION

As discussed in the data analysis section, the small wind direction sectors $\Delta$s are very sensitive to the wind direction uncertainty used to select the data. As the uncertainty in wind direction is still quite high because of the sensor used (the nacelle position sensor follows the yaw misalignment), the benchmarks based on the small $\Delta$s might not give a good representation of the accuracy of the wake models. The uncertainty in wind direction creates an artificially lower wake deficit during the ensemble averaging. In these smaller $\Delta$s the models seem in majority to over-predict the wake deficit, which might be because the SCADA is heavily influenced by the wind direction uncertainty. When looking at the probability distribution of the SCADA measurements, most of the models do seem to remain within the spreading of the data. With this in mind, it is quite difficult to pick one model performing better than the other one over the test castes $\Delta = 5°$ and $\Delta = 15°$.

For modeling more fairly the small $\Delta$s, it could be necessary to post-process the wake models to account for the effect of wind direction uncertainty in the measurement averaging as proposed by Gaumond et al. [4].

The wind direction sector $\Delta = 30°$ is the $\Delta$ normally used for calculating the AEP. As estimating accurately the AEP is the main focus of the current EERA-DTOC project, it should be

here considered that $\Delta = 30°$ is the more important benchmark compared with the two others $\Delta$s benchmarks. So even thought most models seem to over-estimate the wake deficit in the smaller $\Delta$s, many are still performing quite well in $\Delta = 30°$ and could therefore still produce very accurate AEPs.

The results of fig. 6, 7 and 8 are very close to a previously published work on the same Horns Rev wind farm case in the UpWind project [18]. While since then the SCADA data have been refined (i.e the measurements points have a lower uncertainty), and some of the models have been re-factored for offshore conditions, the main conclusions stay the same. The wake model still over predict the narrow sectors, probably due to the wind direction uncertainty, while they perform satisfyingly for the larger sector.

Looking at the benchmark results, the wake accumulation method might have a strong influence the shape of the wake deficit along a row of turbine. The DWM (i.e. using the maximum) and NOJ flavors (i.e. using a RSS) seem to perform the least well to match the SCADA shape, even at large $\Delta$s. They both present flatter trends compared with the SCADA measurements, that seems to indicate that if the wind farm was larger their results would deviate even more strongly. This results are in agreement with previous studies [4,6].

It is somewhat difficult to judge the importance of the other sub-model assumptions as most models use quite different combinations. For instance, it is not clear how sensible the models are regarding the number of points needed to produce the hub wind speed. For answering this specific question, it would be more appropriate to carry out a sensitivity analysis on each specific model.

Similarly, only one model uses an advanced aero-elastic model with a controller for the wind turbine (DWM). It is not clear from the results that this would be giving a more realistic estimate of the wind farm annual energy production. Here again it would be interesting to test each model independently if they would benefit from a more sophisticated wind turbine model.

While they seem to perform satisfyingly in the first two test cases, the more computationally intensive non-linear CFD models such as RANS and CRESflowNS do not seem to show any more realistic behavior compared with the order of magnitude faster CFD models such as FarmFlow, FUGA or even the engineering models such as Ainslie or GCL.

## CONCLUSIONS AND FUTURE WORK

This article presented the results of a benchmark campaign carried on within the EERA-DTOC project, in collaboration with the IEA-Task 31 ”WakeBench” project. A wide scope of different wake models have been compared on different types of test cases. Because of the complexity of dealing with large offshore wind farm SCADA data, it is very challenging to create comparable results to the wind farm wake models. Especially, the issue of wind direction uncertainty is found to create an artificially lower wake deficit. As the models are not directly taking into account this uncertainty it is important to take a step back from the benchmarking results and being pragmatic about the performance of the different models. For instance, the performance of

the wake models in small wind direction averaging windows are not so critical when estimating the annual energy production, which is the focus of EERA-DTOC.

Within the EERA-DTOC project another test case is planned on the Horns Rev benchmark. The wind farm efficiency polar distribution, should give a more quantifiable metric of the accuracy of the wind farm wake models to estimate AEPs. Another benchmark is also planned on the Lillgrund wind farm in collaboration with the IEA-Task 31 ”WakeBench” and Vattenfall AB, the wind farm owner. The wind turbines are larger and more closely spaced, which should challenge the wake models in a different manner than the Horns Rev wind farm did.

## ACKNOWLEDGEMENTS

This work is supported by the EU EERA-DTOC project nr. FP7-ENERGY-2011/n 282797, and of the Danish EUDP-WakeBench project nr. 64011-0308. The Horns Rev data was gratefully provided through previous projects by the wind farm owners Vattenfall AB and DONG Energy AS.

## REFERENCES

[1] Hansen K., Barthelmie R.J., Jensen L., Sommer A., 2011a, The impact of turbulence intensity and atmospheric stability on power deficits due to wind turbine wakes at Horns Rev wind farm, Wind Energy, doi: 10.1002/we.512, 2001.
[2] Hansen K., et al., 2011b, Guideline to wind farm wake analysis. In UPWIND 1A2 Metrology, Final Report, Chapter 8, ECN-E–11-013, February 2011.
[3] Hansen K., et al., 2011c, Classification of atmospheric stability for offshore wind farms. In UPWIND 1A2 Metrology, Final Report, Chapter 10, ECN-E–11-013, February 2011.
[4] Gaumond M., et al., 2011c, Evaluation of the wind direction uncertainty and its impact on wake modelling at the Horns Rev offshore wind farm, Wind Energy, 2013.
[5] Anderson M., Simplified soultion to the eddy viscosity wake model, www.res-americas.com, 2009.
[6] Habenicht G. Offshore wake modelling, Presentation at Renewable UK Offshore Wind, www.res-group.com, 2011.
[7] Larsen T.J., Hansen A.M., How 2 HAWC2, the user’s manual. Technical Report, Risø-R-1597, DTU-Wind Energy, Risø, Denmark 2007.
[8] Ainslie J.F., Calculating the flow field in the wake of wind turbines, Journal of Wind Engineering and Industrial Aerodynamics, 27: p 213-224, 1988.
[9] Crespo, A., Hernández, J., Fraga, E., Andreu, C., Experimental validation of the UPM computer code to calculate wind turbine wakes and comparison with other models. Journal of Wind

Engineering, 27, p 77–88, 1998.
[10] Mortensen N.G., Heathfield D.N., Rathmann O., Nielsen M., Wind Atlas Analysis and Application Program: WAsP 10 Help Facility. Technical report, Risø National Laboratory, Roskilde, Denmark, December 2011.
[11] N.O. Jensen. A note on wind generator interaction. Technical Report Risø-M- 2411, Risø National Laboratory, Roskilde, Denmark, 1983.
[12] Ott S., Berg J., Nielsen M., "Linearised CFD Models for Wakes". Technical Univ. of Denmark, Risoe National Lab. for Sustainable Energy. Wind Energy Div. Risoe-R-1772(EN) ISBN 978-87-550-3892-9. Available online.
[13] Prospathopoulos, J. M. and Chaviaropoulos, P.K., "Numerical simulation of offshore wind farm clusters", European Wind Energy Association, Conference proceedings 2013.
[14] Chaviaropoulos P. K. and Douvikas D. I., "Mean-flow-field Simulations over Complex Terrain Using a 3D Reynolds Averaged NavierStokes Solver," Proceedings of ECCOMAS 98, Vol. I, Part II, pp. 842-848. 1998.
[15] Larsen GC. A simple stationary semi-analytical wake model. Technical Report, Risø-R-1713(EN) August, Risø DTU 2009.
[16] Larsen GC, Madsen HA, Thomsen K, Larsen TJ. Wake meandering: a pragmatic approach. Wind Energy Jul 2008; 11(4):377–395, doi:10.1002/we.267.
[17] Madsen HA, Larsen GC, Larsen TJ, Troldborg N, Mikkelsen R. Calibration and Validation of the Dynamic Wake Meandering Model for Implementation in an Aeroelastic Code. Journal of Solar Energy Engineering 2010; 132(4):041 014, doi:10.1115/1.4002555.
[18] Barthelmie R.J., Hansen K., Frandsen S.T., Rathmann O., Schepers J.G., Schlez W., Phillips J., Rados K., Zervos A., Politis E.S., Chaviaropoulos P.K., Modelling and Measuring Flow and Wind Turbine Wakes in Large Wind Farms Offshore. Wind Energy, doi:10.1002/we.348, 2009.
[19] Barthelmie R.J., Barthelmie, Larsen G.C., Pryor S., Jørgensen H.E., Bergström H., Schlez W., Rados K., Lange B., Vølund P., Neckelmann S., Mogensen S., Schepers G., Hegberg T., Folkerts L., Magnusson M., ENDOW (efficient development of offshore wind farms): modelling wake and boundary layer interactions. Wind Energy. 2004. DOI: 10.1002/we.121.
[20] Réthoré P.-E., Wind Turbine Wake in Atmospheric Turbulence, PhD Thesis, Aalborg University, 2009.
[21] Rathmann O, Ott S & Kelly MC , 'Wind farm wake effects estimations by a mosaic tile wake model'. in: Proceedings. EWEA 2011.

# Modeling large offshore wind farms under different atmospheric stability regimes with the Park wake model

**A. Peña[1], P.-E. Réthoré[1], O. Rathmann[1]**

[1]DTU Wind Energy, Risø campus, Frederiksborgvej 399, 4000 Roskilde, DK, aldi@dtu.dk

## ABSTRACT

Here, we evaluate a modified version of the Park wake model against power data from a west-east row in the middle of the Horns Rev I offshore wind farm. The evaluation is performed on data classified in four different atmospheric stability conditions, for a narrow wind speed range, and a wide range of westerly wind directions observed at the wind farm. Simulations (post-processed to partly account for the wind direction uncertainty) and observations show good agreement for all stability classes, being the simulations using a stability-dependent wake decay coefficient closer to the data for the last turbines and those using the WAsP recommended value closer to the data for the first turbines. It is generally seen that under stable and unstable atmospheric conditions the power deficits are the highest and lowest, respectively, but the wind conditions under both stability regimes are different. The simulations do not approach the limits of the infinite wind farm under any stability condition as winds are not parallel to the row.

## INTRODUCTION

In the last years, investigation of the effect of atmospheric stability on the production of wind farms has gained attention, partly because it has been observed, particularly at large offshore wind farms, that under stable and unstable atmospheric conditions, the wind farms under- and over-perform, respectively, when compared to wind farm data under neutral conditions [1]. Most wake models do not account for stability conditions other than neutral and, thus, model under-performance–when compared to wind farm data–is sometimes attributed to the effect of atmospheric stability.

The Park wake model [2] used in the Wind Atlas Analysis and Application Program (WAsP) [3] is based on the model of Jensen [4], which makes use of the wake decay coefficient $k_w$ to estimate the wind speed reduction for a given thrust coefficient, downstream distance, turbine diameter, and upstream wind speed. It is recommended in WAsP to use $k_w = 0.05$ for offshore wind farms (lower than the recommended value onshore of 0.075). This is because $k_w$ is related to the entrainment of the wake in the atmosphere (it is in fact the slope of the expansion of the wake) and as such it is a function of the surface roughness $z_o$ (the lower the roughness the less

wake expansion). Frandsen [5] by semi-empirical means suggested $k_w = 0.5/\ln(h/z_o)$, where $h$ is the turbine's hub height, which generally translates into lower $k_w$ values than the WAsP recommendations ($k_w = 0.039$ for a typical wind turbine offshore). Barthelmie and Jensen [6] found that using $k_w = 0.03$ adjusted well the results of the Park wake model at the Nysted wind farm when compared to data. Interestingly, at Nysted, i.e. in the South Baltic Sea, stable conditions are mostly observed.

Here, we present an analysis of wind farm data carried out at the Horns Rev I offshore wind farm, where we are able to classify wind turbine power data into different atmospheric stability classes. A set of simulations using a modified version of the Park wake model are performed using different $k_w$ values correspondent to particular atmospheric stability conditions. The simulations are post-processed in order to partly take into account the wind direction uncertainty and compared to the data. Since Horns Rev I is a rather large wind farm, for the wind directions analyzed we might expect that some cases will approach the limits of an infinite wind farm. Therefore, we also present the results of the Park wake model evaluated to its infinite theoretical limits.

## MODIFIED PARK WAKE MODEL

We implemented the Park wake model described in Katic et al. [2] in a Matlab script to run simulations for a wide variety of wind directions, wind speeds, wind farm layouts, wind turbine specifications, and $k_w$ values. We refer to it as "modified" because in WAsP the model has been extended to account for the effect of ground-reflected wakes from upwind turbines and our version takes into account the wakes upwind (directly or sideways) only.

Peña and Rathmann [7] showed that adjusting $k_w$ to match the wind speed reductions estimated by a stability dependent infinite wind farm boundary layer model (a totally different model based on the concept of Frandsen [5], which generally gives higher wind speed reductions in stable compared to unstable conditions) resulted in lower $k_w$ values under stable compared to unstable conditions. The adjustment was performed evaluating the Park wake model for an infinite wind farm. Similar results were found when evaluating this 'infinite' Park wake (IPW) model assuming,

$$k_w = u_{*free}/u_{hfree} = \kappa/\left[\ln(h/z_o) - \psi_m(h/L)\right], \tag{1}$$

where $u_{*free}$ and $u_{hfree}$ are the undisturbed friction velocity and hub-height wind speed, respectively, $\kappa = 0.4$ is the von Kármán constant, and $\psi_m(h/L)$ is the extension to the logarithmic wind profile to account for stability and depends on the height (in this case the hub-height) and atmospheric stability by means of $L$ (the Obukhov length). The expressions for $\psi_m$ can be found in Peña [8]. Expressions for the IPW model are also given in Peña and Rathmann [7]. Since our Matlab implementation only accounts for upwind wakes, we use the expressions for the same type of wakes.

## HORNS REV I WIND FARM

The Horns Rev I wind farm is located in the Danish North Sea at about 17 km west from the coast (from the wind farm's northwest corner). A layout of the wind farm showing the positions

of the 80 wind turbines (rows are named from A to H and columns from 1 to 10) and three meteorological (met) masts is shown in Fig. 1-left. The turbines are Vestas V80 2 MW machines of 80-m rotor diameter and 70-m hub height. Power and thrust-coefficient curves are illustrated in Fig. 1-right.

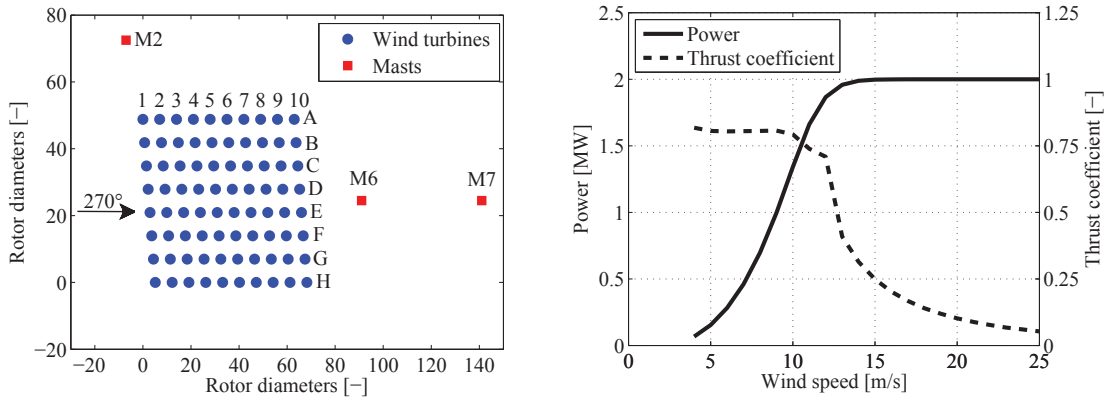


Figure 1: (left) The Horns Rev I offshore wind farm. (right) Power and thrust coefficients as function of wind speed for the Vestas V80 wind turbine (figures taken from [3])

A met mast (M2) is located about 2 km north from the northwest edge of the wind farm. Met data from this mast have been extensively analyzed for atmospheric stability studies (e.g. in Peña and Gryning [9], Peña et al. [10], and Peña and Hahmann [11]). Here we use measurements from the cup anemometers at 62 and 15 m above mean sea level (AMSL–all measurements are referred to AMSL hereafter unless otherwise stated), a wind vane at 43 m, temperature sensors at 13 and –4 m (the latter is below mean sea level), and humidity and pressure sensors at 13 and 55 m, respectively.

## DATA TREATMENT

Concurrent 10-min data from the wind turbines and M2 are used. Data from the turbines include a power quality signal indicating the status of the turbine and the power signal (stopped, down-regulated, etc). We choose to use data when all turbines show status equal to 1 (i.e. a validated measurement where the turbine does not stop and there are no spikes or drop outs).

Atmospheric stability at the wind farm is assessed using the observations at M2. In order to filter data where the climate/conditions are not similar at the two places, we first analyze the wind direction observed at M2 and that at turbine 07 (row G, column 1). For the latter we use the nacelle position, which was found to be optimal for analyzing the wake effect for wind directions $270 \pm 60°$ [12]. Figure 2 shows a scatter plot between the two measurements where it is observed a very good correspondence for most cases. We select cases where the difference between both signals is lower than 15° and where the wind direction at turbine 07 is $270 \pm 60°$ (the latter criterion also ensures that no wakes affect the stability estimations at M2 and might allow us to study the array in the limits of the infinite wind farm).

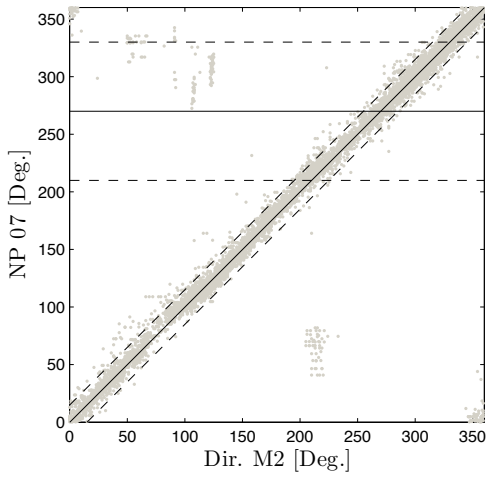


Figure 2: Wind direction observed at M2 at 43 m and the nacelle position (NP) of turbine 07. The lines illustrate the filtering criteria used for the data (see text)

We further study the agreement between the wind speeds observed at M2 at 62 m and the nacelle one at M7 at 70 m (Fig. 3-left). As illustrated both signals show very good agreement and so we use them to further filter data: we choose the wind speed range $5-10$ m s$^{-1}$ (since the thrust coefficient is nearly constant within this range) and the difference between both signals needs to be lower than 1 m s$^{-1}$. Before this 'filtering' step, we check the power performance using the wind speed and power signals of turbine 07, which as seen in Fig. 3 compares well with the one provided by the manufacturer (slightly over and under-estimating the power below and above $\sim 10$ m s$^{-1}$, respectively).

Our analysis is focused on the wind speed deficits of row E and so we extract power data correspondent to the turbines on that row only. We use another filtering criterion based on the standard deviation of the power signal. It is noted a good amount of data with negative power values and we were advised to use values higher than 5 kW for the standard deviation of the power for the analysis (Kurt Hansen, personal communication). We increase the criterion to 12 kW. These final reduced dataset is then complemented with the concurrent measurements from M2 (atmospheric static stability is derived as in Peña and Hahmann [11], i.e. estimating the bulk Richardson number, which translates into a measure of $L$), and the nacelle position and wind speed of turbine 05 (row E, column 1). Figure 4-left shows the power performance of turbine 05 where a very similar behavior to that observed for turbine 07 is found (Fig. 3-left). For the rest of the analysis, we use the wind speed resulting from converting the power to wind speed of turbine 05 (through the power curve in Fig. 1-right) as a proxy for the undisturbed wind speed. For completeness, we illustrate in Fig. 4-right that the nacelle position of turbine 05 cannot be used for wake analysis since it is rather different to that of turbine 07.

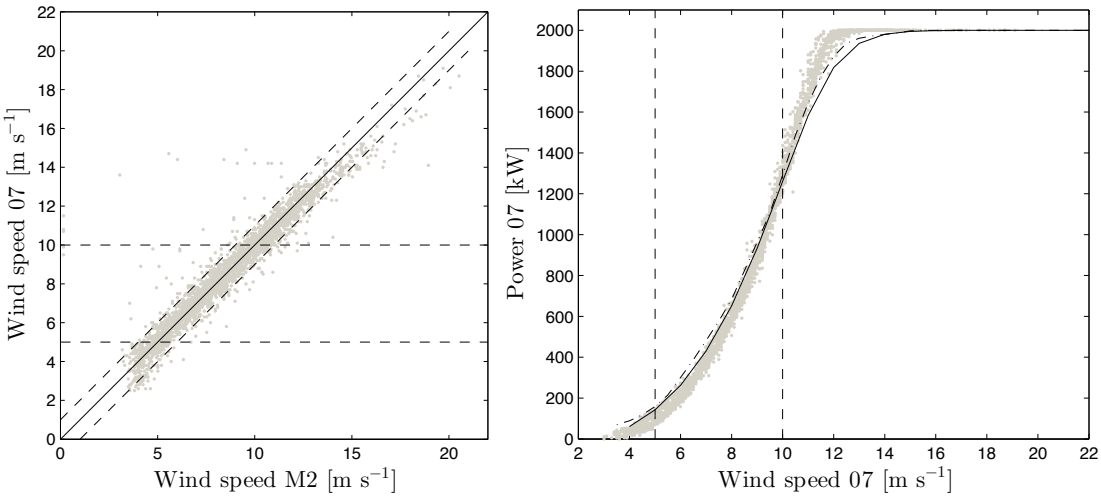


Figure 3: (left) Wind speeds at M2 at 62 m and that at the nacelle of turbine 07 at 70 m. The lines illustrate the filtering criteria used for the data (see text). (right) Power performance at turbine 07 based on its nacelle wind speed. The lines show two power curves: the one used in this study (solid line) and that from the offshore Vestas V80 wind generator in WAsP (dash-dotted line)

## RESULTS

The final dataset results in 1525 10-min values. The data is classified in four stability classes: very unstable ($-75$ m $\leq L \leq -10$ m), unstable ($-500$ m $\leq L \leq -75$ m), neutral ($|L| \geq 500$ m), and stable (500 m $\geq L \geq 5$ m). Figure 5-left shows the ensemble average of power deficits of row E (normalized with the power of turbine 05) for the different stability classes. Although it is observed a general higher power reduction in stable compared to unstable conditions, this type of comparison is misleading, since the wind speed and direction conditions under each stability class are not the same. Figure-5-right illustrates the histograms of wind speed for the different stability conditions and is noticed that they show different distributions. We further narrow the analysis to wind speeds of $8.5 \pm 0.5$ m s$^{-1}$ to reduce the variability of wind conditions maximizing the amount of data.

Although the reduction in the variability of power deficits, for each stability class the difference in the individual 10-min power deficit values is very large. One of the main reasons for this is that the observed wind direction range is rather broad and the distributions are different (Fig. 6). However we cannot narrow the range any further as we might find very few or no data: e.g. most very unstable and unstable conditions are seen within the range 290°–310°, whereas there are no data and nearly nothing for that range under neutral and stable conditions, respectively.

For each stability class we choose to run simulations using the Horns Rev I layout (thrust coefficient and power curves as in Fig.1) using the modified Park wake model for $u_{hfree} =$ 8.5 m s$^{-1}$ and a wide undisturbed wind direction range of 180°–360° (at a resolution of 0.5°). This is performed for $k_w$ values of 0.05, 0.0349, 0.0338, 0.0313, and 0.0231, which correspond,

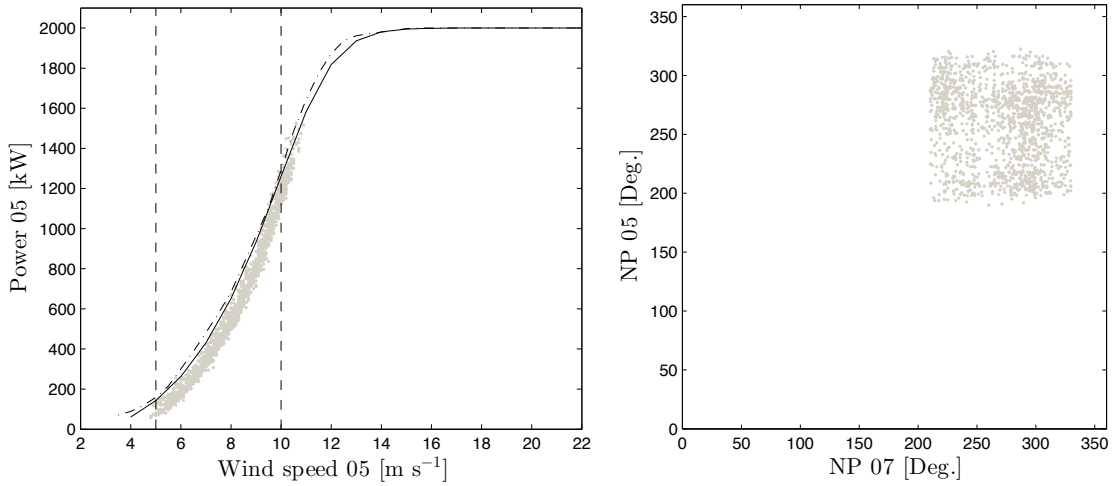


Figure 4: (left) As Fig. 3-right but for turbine 05. (right) Comparison of the nacelle position signals of turbines 05 and 07

respectively, to the WAsP recommended one, and those for very unstable, unstable, neutral, and stable conditions. For the estimation of these coefficients, we average the bulk Richardson number under each class, convert this average into a $L$ value, estimate the $\psi_m$ correction at hub height, and evaluate Eq. (1) assuming $z_o = 0.0002$ m.

The simulations are further post-processed to take into account part of the wind direction uncertainty as in Gaumond et al. [13], i.e. assuming that within a 10-min interval the wind direction distributes as a normal distribution with a given standard deviation $\sigma$ (we use a value of 2.5°). The procedure is briefly as follows: for each observed 10-min wind direction $\theta$ under each atmospheric stability class, we extract the simulations correspondent to the range $[\theta - 3\sigma, \theta + 3\sigma]$. We then weight each simulation using the normal probability distribution function. For each observed 10-min wind direction and speed deficit, there is therefore a single simulated wind speed deficit (derived from 31 gaussian-weighted simulations).

Figures 7–10 show the results of the comparison of the observed 10-min power deficits and those simulated at row 5 for the different stability classes. They are not shown in the same figure as they correspond to observations/simulations under different wind direction conditions. The ensemble average of both simulations (with a stability-specific $k_w$ value) and observations are also shown together with that of the simulations using $k_w = 0.05$. As the results of the simulations are wind speed deficits, we translate them into power deficits with the power curve in Fig. 1.

The results generally show a very good agreement between the ensemble averages of simulations and observations. For each stability condition the result using the stability-specific $k_w$ value shows higher power reductions compared to that using $k_w = 0.05$, as a lower $k_w$ value increases the wake effect. Particularly, under neutral stability conditions, the ensemble average of the simulations using both the stability-specific and WAsP recommended $k_w$ values shows that the model predict higher power deficits than observed for all turbines in the row. This is very

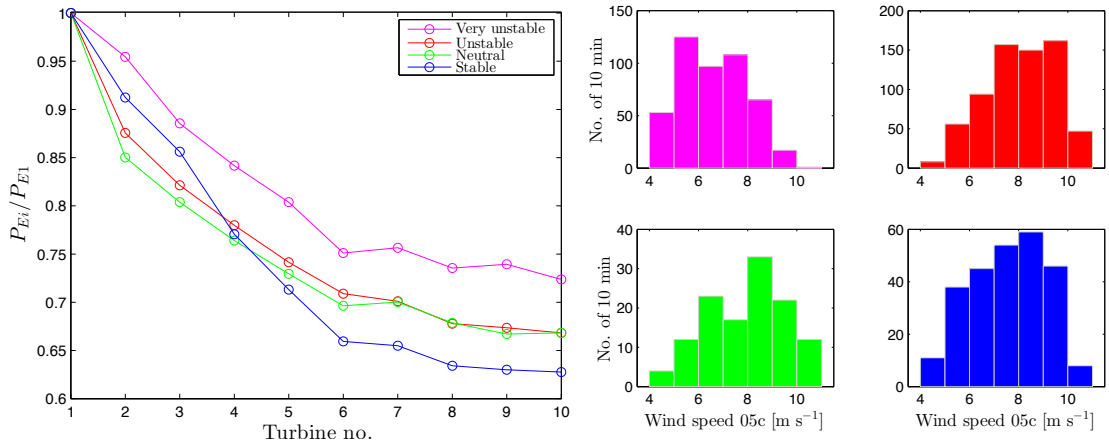


Figure 5: (left) Ensemble average power deficit of row E (normalized with the power of turbine 05 $P_{E1}$) for different atmospheric stability conditions. (right) Wind speed histograms (based on the power-converted value from turbine 05) for each stability condition

interesting because in most of the studies at Horns Rev I and at other large offshore wind farms where the Park wake model has been used, the results are normally the opposite: model under-prediction of the power deficits. This might be partly due to range of wind directions we use for our analysis and to the post-processing of the simulations accounting for the wind direction uncertainty.

Apart from the neutral case (which is the one with the less data), the simulation with the stability-dependent $k_w$ fits better the power deficit at the last turbines in the row compared to the simulations using $k_w = 0.05$, which in turn generally fit well the results of the first turbines in the row. However, most of the outliers (i.e. the individual 10-min power deficits where $P_{Ei}/P_{E1} > 1$) are found at those first turbines in the row (there are fewer outliers at the last turbines). Removing such 'outliers' brings the ensemble average closer to the simulation but there is no good reason to remove them as they seem to be good observed data.

We can also note that the range of the results of the simulations and that of the observations for each stability class is well predicted (except for the clear outliers). The cloud of observations (and simulations) of power deficits for unstable conditions is clearly between 0.5 and 0.8 and for very unstable conditions between 0.6 and 0.8.

The largest power deficit drop is observed at turbine E2 (as expected) and appears in the neutral class (this is the one where most of the observed wind comes from 270°). The infinite limits of power reduction are 0.26, 0.15, 0.28, 0.30, and 0.44 for neutral, stable, unstable, very unstable, and the WAsP-recommended $k_w$-values, respectively; none of the ensemble observed power deficits seem to approach the infinite limits.

Also interestingly, under very unstable atmospheric conditions the ensemble average of power deficit (simulated and observed) at turbine E2 is very similar to that at turbine E1; as shown in Fig. 6 for this atmospheric stability condition, there are no observation of winds parallel to the row and winds mostly come from 300°. Turbine E2 is thus mostly affected by partial wakes from turbines E1 and D1.

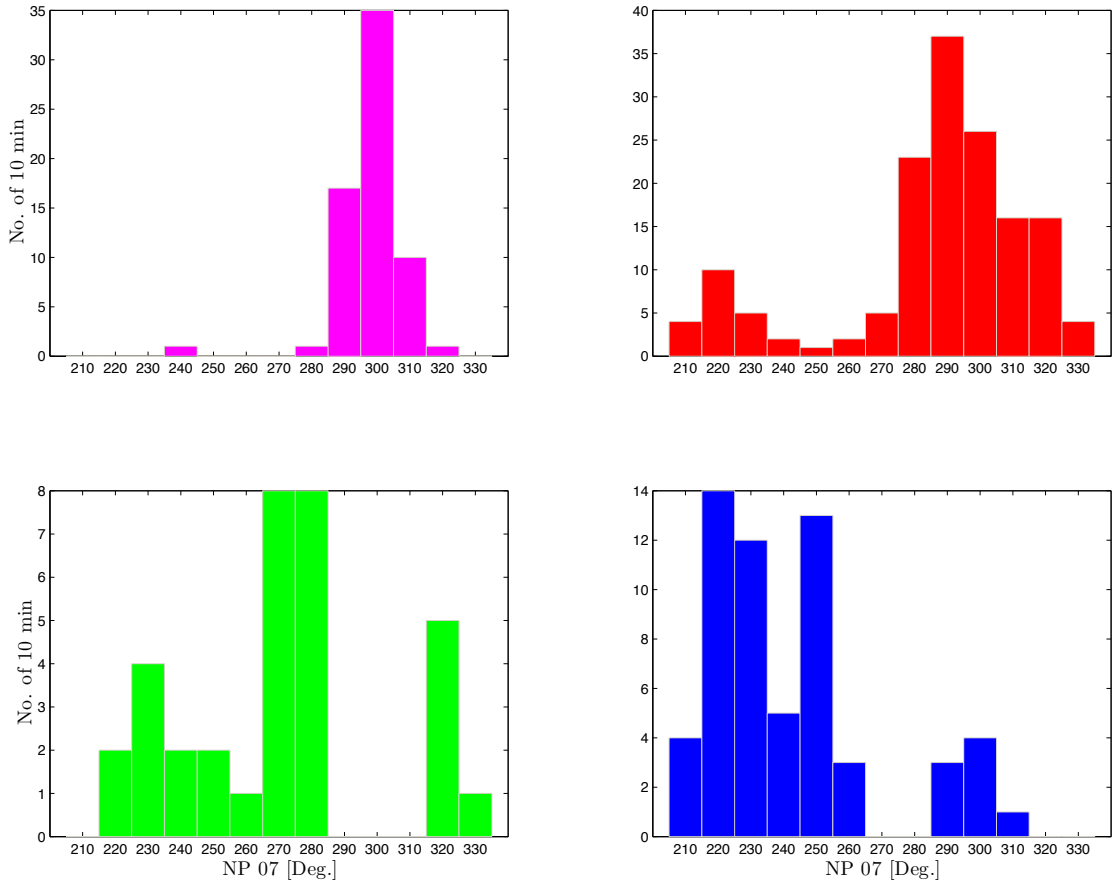


Figure 6: Wind direction histograms (based on the nacelle position of turbine 07) for each stability condition: very unstable (top left), unstable (top right), neutral (bottom left), and stable (bottom right)

## CONCLUSIONS

Power deficit data from the Horns Rev I offshore wind farm are analyzed under different atmospheric stability conditions, a nearly constant undisturbed wind speed, and a wide range of westerly wind directions. The resulting dataset is compared with simulations using a modified version of the Park wake model and the limits of the Park wake model when evaluated as an infinite wind farm.

It is found a very good agreement between simulations and observations for a west-east row in the middle of the wind farm. The simulations using a stability-dependent $k_w$ value are closer to the observations at the last turbines and those using the WAsP recommended $k_w$ value of 0.05 closer to the observations at the first turbines on that row.

Due to the range of observed and simulated wind directions, it is difficult to conclude whether under stable or unstable atmospheric conditions the wind farm, respectively, under-

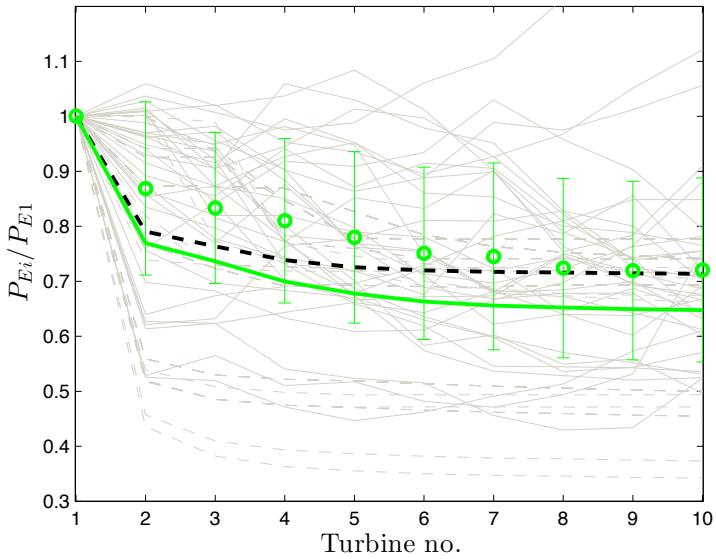


Figure 7: Power deficits of row E (normalized with the power of turbine 05 $P_{E1}$) for neutral conditions. The gray solid lines show the 10-min power deficits (in gray dashed lines for each simulation), the colored circles the ensemble average (error bars with $\pm$ the standard deviation), the solid colored line the ensemble average of the simulations with the stability-specific $k_w$ value, and the black dashed line that of the simulations with $k_w = 0.05$

or over-performs. However, it is seen higher power reductions under stable than unstable atmospheric conditions. In none of the conditions, the observations seem to approach the limits of the infinite wind farm.

## REFERENCES

[1] Jensen LE. Array efficiency at Horns Rev and the effect of atmospheric stability. *Proceedings of the European Wind Energy Association Conference & Exhibition*, Milano, 2007.

[2] Katic I, Højstrup J, Jensen NO. A simple model for cluster efficiency. *Proceedings of the European Wind Energy Association Conference & Exhibition*, Rome, 1986.

[3] Mortensen NG, Heathfield DN, Myllerup L, Landberg L, Rathmann O. Getting started with WAsP 9. *Technical Report Risø-I-2571(EN)*, Risø National Laboratory, Roskilde 2007.

[4] Jensen NO. A note on wind generator interaction. *Technical Report Risoe-M-2411(EN)*, Risø National Laboratory, Roskilde 1983.

[5] Frandsen S. On the wind speed reduction in the center of large clusters of wind turbines. *J. Wind Eng. Ind. Aerodyn.* 1992; **39**:251–265.

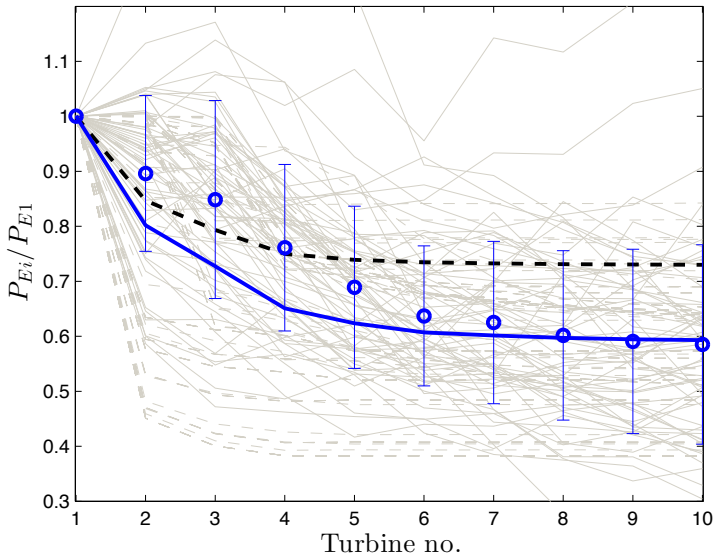


Figure 8: As Fig. 7 but for stable conditions

[6] Barthelmie R, Jensen LE. Evaluation of wind farm efficiency and wind turbine wakes at the Nysted offshore wind farm. *Wind Energy* 2010; **13**:573–586.

[7] Peña A, Rathmann O. Atmospheric stability dependent infinite wind farm models and the wake decay coefficient. *Wind Energy* 2013; In press.

[8] Peña A. Sensing the wind profile. *Technical Report Risø-PhD-45(EN)*, Risø DTU, Roskilde 2009.

[9] Peña A, Gryning SE. Charnock's roughness length model and non-dimensional wind profiles over the sea. *Bound.-Layer Meteorol.* 2008; **128**:191–203.

[10] Peña A, Gryning SE, Hasager CB. Measurements and modelling of the wind speed profile in the marine atmospheric boundary layer. *Bound.-Layer Meteorol.* 2008; **129**:479–495.

[11] Peña A, Hahmann AN. Atmospheric stability and turbulent fluxes at Horns Rev–an intercomparison of sonic, bulk and WRF model data. *Wind Energy* 2012; **15**:717–730.

[12] Hansen KS, Barthelmie RJ, Jensen LE, Sommer A. The impact of turbulent intensity and atmospheric stability on power deficits due to wind turbine wakes at horns rev wind farm. *Wind Energy* 2012; **15**:183–196.

[13] Gaumond M, Rethoré PE, Ott S, Peña A, Bechmann A, Hansen KS. Evaluation of the wind direction uncertainty and its impact on wake modelling at the horns rev offshore wind farm. *Wind Energy* 2013; In press.

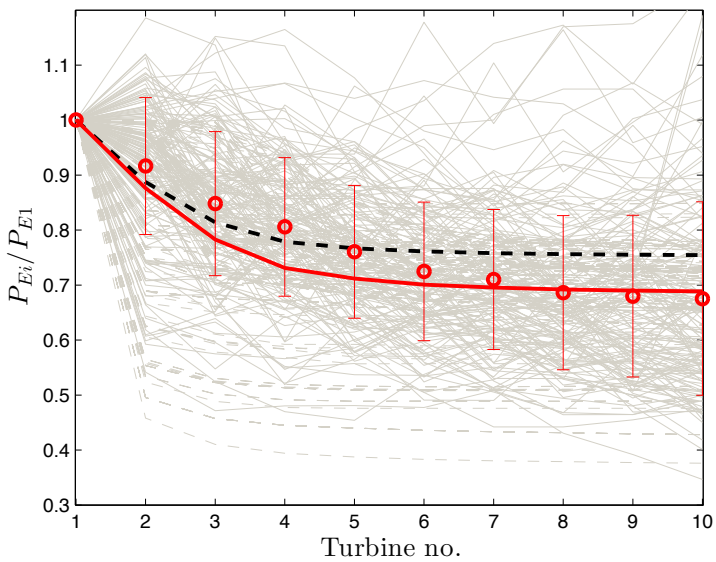


Figure 9: As Fig. 7 but for unstable conditions

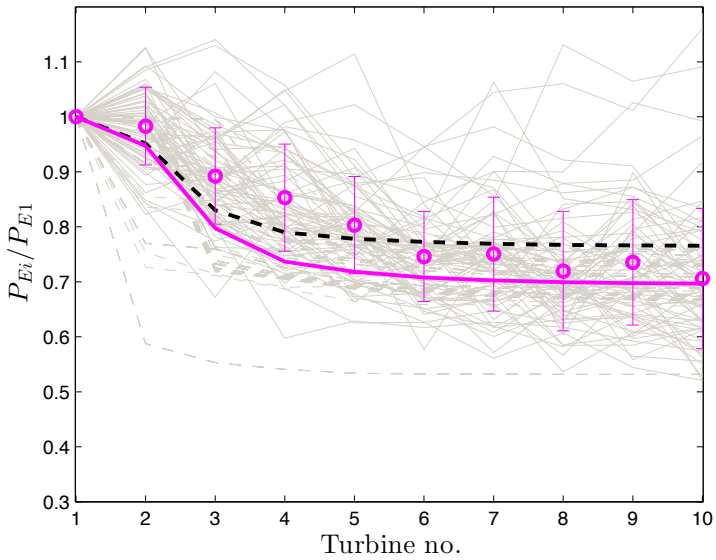


Figure 10: As Fig. 7 but for very unstable conditions

Wind Energy

WIND ENERGY
*Wind Energ.* (2013)
Published online in Wiley Online Library (wileyonlinelibrary.com). DOI: 10.1002/we.1632

RESEARCH ARTICLE

# Atmospheric stability-dependent infinite wind-farm models and the wake-decay coefficient

Alfredo Peña and Ole Rathmann

DTU Wind Energy, Risø Campus, Technical University of Denmark, Roskilde, Denmark

## ABSTRACT

We extend the infinite wind-farm boundary-layer (IWFBL) model of Frandsen to take into account atmospheric static stability effects. This extended model is compared with the IWFBL model of Emeis and to the Park wake model used in Wind Atlas Analysis and Application Program (WAsP), which is computed for an infinite wind farm. The models show similar behavior for the wind-speed reduction when accounting for a number of surface roughness lengths, turbine to turbine separations and wind speeds under neutral conditions. For a wide range of atmospheric stability and surface roughness length values, the extended IWFBL model of Frandsen shows a much higher wind-speed reduction dependency on atmospheric stability than on roughness length (roughness has been generally thought to have a major effect on the wind-speed reduction). We further adjust the wake-decay coefficient of the Park wake model for an infinite wind farm to match the wind-speed reduction estimated by the extended IWFBL model of Frandsen for different roughness lengths, turbine to turbine separations and atmospheric stability conditions. It is found that the WAsP-recommended values for the wake-decay coefficient of the Park wake model are (i) larger than the adjusted values for a wide range of neutral to stable atmospheric stability conditions, a number of roughness lengths and turbine separations lower than $\sim$ 10 rotor diameters and (ii) too large compared with those obtained by a semiempirical formulation (relating the ratio of the friction to the hub-height free velocity) for all types of roughness and atmospheric stability conditions. Copyright © 2013 John Wiley & Sons, Ltd.

**KEYWORDS**

atmospheric stability; boundary-layer model; infinite wind farm; Park wake model; wake-decay coefficient; wind-speed reduction

**Correspondence**

Alfredo Peña, DTU Wind Energy, Risø Campus, Technical University of Denmark, Roskilde, Denmark.
E-mail: aldi@dtu.dk

Received 13 September 2011; Revised 10 April 2013; Accepted 15 April 2013

## 1. INTRODUCTION

Most wind Park wake (WPW) models are able to estimate wind-speed reductions within the wind farm for a wide range of wind speeds, assuming neutral atmospheric conditions in most cases. These models, such as the Park wake model[1] implemented in the Wind Atlas Analysis and Application Program (WAsP),[2] predict well the energy yield losses due to wakes when analyzing long terms of meteorological (met) and wind-farm data. This is partly because in a long term, most atmospheric static stability conditions at wind turbine sites are generally close to neutral. According to Troen and Petersen,[3] the long-term atmospheric stability is just a little biased to the stable side over land and to the unstable side over water from the analysis of met stations over Northern Europe, which showed a higher amount of positive compared with negative surface heat fluxes at few offshore met masts, whereas for Peña and Hahmann[4] is slightly biased to the stable side over the North Sea on the basis of the analysis of the probability distribution function of stability measures.

When analyzing wind-farm and met data from the Horns Rev I wind farm in the Danish North Sea, Jensen[5] estimated that the annual mean array efficiency reduces from 91.5% under unstable to 85.3% under stable atmospheric conditions. Barthelmie and Jensen[6] also estimated wind-farm efficiency reductions in stable compared with unstable atmospheric conditions up to $\sim$ 9% for the wind-speed range 9–10 m s$^{-1}$ for the Nysted wind farm in the Danish Baltic Sea. Since wind-farm operators do not want to know the annual energy production of the wind farm only but would also like to forecast the wind-farm energy output for a given set of met conditions, which can rapidly change as shown in Vincent *et al.*,[7] we need to run the WPW models for different met conditions, which include the state of the atmosphere.

Copyright © 2013 John Wiley & Sons, Ltd.

Inclusion of the atmospheric stability dependency in the WPW models is not straightforward. Therefore, an alternative is to simply adjust the parameters in the models to match the observed/measured data. Barthelmie and Jensen[6] found better agreement when comparing the Park wake model with the Nysted wind-farm data by using a lower wake-decay coefficient (0.03) than that recommended in WAsP for offshore conditions (0.05). Interestingly, the amount of stable atmospheric conditions are relatively large at Nysted[6] compared with those in the North Sea,[8] implying that the more stable the atmosphere, the lower the wake-decay coefficient for the Park wake model.

In this paper, we adjust the wake-decay coefficient of the Park wake model, evaluated for an infinite array of wind turbines, to match the wind-speed reduction estimated by the infinite wind-farm boundary-layer (IWFBL) model of Frandsen.[9] The adjustment can be carried out for different wind speeds, turbine to turbine separations, surface roughness lengths and atmospheric stability conditions. Since Frandsen developed his model for neutral conditions only, we extend it for diabatic atmospheric conditions (assuming horizontal and vertical homogeneity of stability) by using local atmospheric stability corrections to the logarithmic (log) wind profile and the resistance law constants of the geostrophic drag law. The stability corrections to the log wind profile are limited to the range of atmospheric conditions and heights where the surface-layer theory is valid. Therefore, considerations should be made, particularly under stable conditions, where the theory is limited to a few tens of meters above the surface only and where the boundary-layer height (BLH) is about the size of the turbines and therefore influences the shape of the wind profile as shown in Peña *et al.*[10] and Sathe *et al.*[8] and when the atmospheric stability changes within the wind farm.

There are other techniques to study the wind-speed reductions due to wind turbine wakes.[11] Computational fluid dynamics (CFD) methods have been extensively applied for multiple wind turbines and in the last couple of years, large eddy simulation (LES) methods have gained popularity compared with the Reynolds averaged Navier–Stokes (RANS) turbulence models. This is partly due to the extension of LESs to account for atmospheric stability conditions other than neutral, which allows LES results to be compared with benchmark cases.[12] The LES technique has also been used to study large arrays of wind farms,[12–14] which can also provide the information needed to adjust the wake-decay coefficient of the Park wake model. However, RANS/LES-based wake models are about 6–7 orders of magnitude slower than the WPW or IWFBL models.

In the description of the model by Frandsen and its extension, we compare it with the results for the wind-speed reduction of an infinite array of turbines of the IWFBL model of Emeis and Frandsen (E&F)[15] and those of the Park wake model. We also show the differences between the WAsP-recommended, the semiempirical (described in Section 3) and the IWFBL-adjusted wake-decay coefficients. Results from the Park wake model are not compared with wind-farm data. Analysis of such data is as challenging as the modeling itself,[16] particularly for different atmospheric stability conditions because since most wind farms have no means to estimate stability, it is difficult to separate the effect on wind-farm power production of stability, wind speed and turbulence from real data[6] and because in large wind farms, turbines do not operate concurrently and optimally all the time.

## 2. IWFBL MODELS

### 2.1. Review

The IWFBL model of Frandsen[9] assumes that within an infinite wind farm with the same turbine type and dimensions, two layers in the atmospheric boundary layer (ABL) are distinguished, one above and one below the turbines' hub height $h$ as shown in Figure 1. At $h$, the shear of both layers is linked as

$$\rho \boldsymbol{u}_{*2}^2 = \rho \boldsymbol{u}_{*1}^2 + t, \tag{1}$$

where $\boldsymbol{u}_{*2}$ and $\boldsymbol{u}_{*1}$ are the friction velocities within the above and below layers, respectively, and $t$ is the jump in shear due to the turbines. The latter is given as $t = \rho c_t u_h^2$, $\rho$ being the air density, $u_h$ the hub-height spatial average wind speed within the wind farm and $c_t$ the areal homogenously distributed thrust coefficient,

$$c_t = \frac{\pi}{8} \frac{C_t}{s_r s_f}, \tag{2}$$

where $s_r = x/D_r$ and $s_f = y/D_r$, $x$ and $y$ being the along-wind and cross-wind turbine to turbine distances, respectively, $C_t$ the turbine's thrust coefficient and $D_r$ the rotor diameter.

Since the idea is to derive an expression for $u_h$ by using equation (1), Frandsen[9] applied the log wind profile to estimate $\boldsymbol{u}_{*1}$ and $\boldsymbol{u}_{*2}$ at hub height from the true ($z_o$) and the effective ($z_{oo}$) wind-farm roughness lengths, respectively.

$$\boldsymbol{u}_{*1} = \frac{u_h \kappa}{\ln(h/z_o)} \quad \text{and} \quad \boldsymbol{u}_{*2} = \frac{u_h \kappa}{\ln(h/z_{oo})}, \tag{3}$$

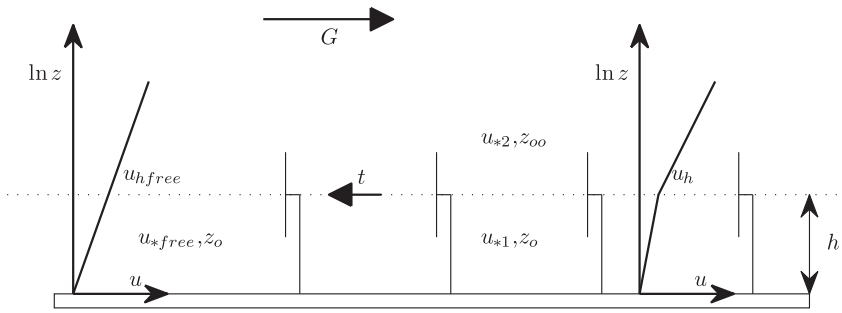


**Figure 1.** The infinite wind-farm boundary-layer model concept of Frandsen.[9] Upstream of the wind farm (free flow), there is one layer with the undisturbed stress scale and background roughness ($\boldsymbol{u}_{*\text{free}}$, $z_o$), and within the wind farm, two layers are assumed to meet at hub height $h$: the lowest with the background roughness and a low-stress-scale $\boldsymbol{u}_{*1}$, and the highest with the effective wind-farm roughness $z_{oo}$ and a high-stress-scale $\boldsymbol{u}_{*2}$.

where $\kappa$ is the von Kármán constant ($\approx 0.4$). Frandsen[9] used a corrected version of the simplified geostrophic drag law of Jensen,[17]

$$\boldsymbol{u}_* = \frac{\kappa G}{\ln\left(\frac{G}{f_p z_o}\right)}, \tag{4}$$

where $G$ is the geostrophic wind speed and $f_p = f_c \exp(A_*)$, $f_c$ being the Coriolis parameter and $A_*$ a modified $A$ parameter from the resistance-law constants, to derive an expression for the effective roughness as a function of the velocity scales:

$$z_{oo} = \frac{G}{f_p} \exp\left(\frac{-\kappa G}{\boldsymbol{u}_{*2}}\right). \tag{5}$$

Equation (5) is then used to eliminate the $\boldsymbol{u}_{*2}$ dependency on $z_{oo}$ in equation (3, right), which results in

$$\boldsymbol{u}_{*2} = \frac{\kappa\,(G - u_h)}{\ln\left(\frac{G}{h f_p}\right)}. \tag{6}$$

For a simple derivation of $u_h$ from equation (1), Frandsen[9] defined $K_2 = (1/\kappa)\ln[G/(h f_p)]$ and $K_1 = (1/\kappa)\ln(h/z_o)$, and thus,

$$\boldsymbol{u}_{*1} = \frac{u_h}{K_1} \quad \text{and} \quad \boldsymbol{u}_{*2} = \frac{G - u_h}{K_2}. \tag{7}$$

Substituting both forms in equation (7) into (1) leads to the solution for $u_h$, i.e., the IWFBL model of Frandsen where

$$u_h = \frac{G}{1 + K_2\sqrt{c_t + K_1^{-2}}}. \tag{8}$$

The wind-speed reduction $R_u$ for the IWFBL model of Frandsen is then given as

$$R_u = \frac{1 + K_2\sqrt{K_1^{-2}}}{1 + K_2\sqrt{c_t + K_1^{-2}}}, \tag{9}$$

which is the ratio of $u_h$ to the asymptotic overall mean wind speed at hub height, i.e., $u_h(c_t \neq 0)/u_h(c_t = 0)$. Equation (8) guarantees that $u_h(c_t = 0)$ is equal to $u_{h\text{free}}$, i.e., the undisturbed hub-height wind speed, as expected. It should be noted that by using any form of the geostrophic drag law, the ABL is assumed in this model to be barotropic and homogenous in terms of flow, atmospheric stability conditions and roughness (valid for large footprint areas).

Emeis and Frandsen[15] further developed another IWFBL model on the basis of the mixing-length theory. Shortly, they assumed the specific turbulent downward momentum flux, $\tau/\rho$, to be driven by the vertical wind-speed gradient above the

wind farm. Using a momentum exchange coefficient $K_m$ to parameterize this flux, E&F related it with the mixing length $l$ as

$$\tau/\rho = K_m \frac{u_o - u_h}{\Delta z} = \frac{l^2}{\Delta z^2}(u_o - u_h)^2, \tag{10}$$

where $u_o$ is the undisturbed wind speed at a height $z = h + \Delta z$ above the wind farm. This flux is assumed to be in balance with the momentum loss due to the turbines.

$$c_t' u_h^2 = \frac{l^2}{\Delta z^2}(u_o - u_h)^2, \tag{11}$$

where $c_t'$ is the drag coefficient of the turbines. The surface drag coefficient is defined as $c_s = u_*^2/u_h^2$ with $\boldsymbol{u}_* = u_h\, \kappa \ln(h/z_o)^{-1}$ (so it can be shown that $c_s = K_1^{-2}$). The effective drag coefficient, $c_{t\text{eff}}$, results from the combination of that of the surface and the one from the turbines, i.e., $c_{t\text{eff}} = c_t' + c_s$.

In E&F, there are two reductions: the first is given by estimating the ratio $u_h/u_o$ from equation 11; the second is found similarly but by replacing $c_t'$ by $c_{t\text{eff}}$. The wind-speed reduction equivalent to equation 9 is found from the ratio of the aforementioned two reductions.

$$R_u = \frac{1 + (\Delta z/l)\sqrt{c_s}}{1 + (\Delta z/l)\sqrt{c_{t\text{eff}}}}. \tag{12}$$

Since it is straightforward to derive $c_t$ from the thrust curve of the wind turbines in the wind farm, we assume that $c_t' = c_t$ in this study. When comparing equations (9) and (12), it can easily be demonstrated that they are identical if $\Delta z/l = K_2$. So, one of their main differences is that the IWFBL model of Frandsen depends on $u_{h\text{free}}$ through both $G$ (via $K_2$) and $C_t$ (which for a wind turbine varies with wind speed), whereas the IWFBL model of E&F, equation (12), is only dependent on $u_{h\text{free}}$ through $C_t$ provided that $l$ is wind-speed independent.

For neutral atmospheric conditions, E&F suggested $\Delta z/l \approx 2/\kappa$, which in terms of the IWFBL model of Frandsen means $\ln[G/(hf_p)] \approx 2$. Such approximation for a place in a rural area ($z_o = 0.025$ m) or at an offshore location ($z_o = 0.0002$ m), both assuming $h = 70$ m, $u_{h\text{free}} = 10$ m s$^{-1}$, $A_* = 4.53$ and latitude of 55.5°, is rather low, since $\ln[G/(hf_p)] = 3.54$ and 2.73, respectively*. Therefore, $R_u$ is generally lower for the IWFBL model of Frandsen than that for E&F. This, as shown later, is valid for a range of wind speeds and atmospheric stability conditions.

The main 'drawbacks' of the IWFBL model of E&F are that (i) $\Delta z$ is rather difficult to estimate and (ii) the mixing-length concept might be inappropriate when modeling wakes.[18] The approach by Frandsen also has drawbacks related to (i) the assumption that at some level above the hub height, the wind-farm wind speed approaches the geostrophic wind-speed value and (ii) the value of $A_*$, since as a modified $A$ parameter of the geostrophic drag law, it is rather uncertain and depends on atmospheric stability among others.[19]

Figure 2 shows the wind-speed reduction comparison between the IWFBL model of Frandsen and that of E&F for different turbine to turbine separations, $s$, and roughness lengths†. As mentioned, the values for $R_u$ from the IWFBL model of E&F are larger (lower reductions) than those from the approach by Frandsen, following its behavior with turbine to turbine distance. There is a faster change in wind-speed reduction with separation, and the differences (between models) are larger within the range of turbine separations where most wind farms lie, i.e., $s < 10$.

The previous comparison is based on a fixed undisturbed hub-height wind speed and thus on a fixed $C_t$ value. When performing a similar analysis (not shown) but for a fixed turbine to turbine separation and surface roughness and different undisturbed hub-height wind speeds, which translate into a range of $C_t$ values, we find similar wind-speed reductions for both IWFBL models, being the $R_u$ values of the E&F model generally larger than those of Frandsen (Frandsen's reductions are only lower for very low $u_{h\text{free}}$ values). For the analysis, we chose a $C_t$ curve from a 2 MW horizontal-axis wind turbine with a near-constant $C_t$ within the low-wind-speed range and decreasing values with increasing wind speed.

## 2.2. Atmospheric stability dependency

Emeis[20] extended the IWFBL model of E&F to account for diabatic atmospheric stability conditions. Since $R_u$ is a function of the mixing length $l$ in equation (12), it was rather simple to extend $l$ for diabatic conditions by using Monin–Obukhov similarity theory (MOST),[21] i.e., adding the dimensionless wind shear $\phi_m$, which is a function of the stability parameter $z/L$, where $z$ is the height above surface and $L$ the Obukhov length. $L$ is a local stability measure, which is assumed in

*$G$ is estimated from the simplified geostrophic drag law, equation (4), and related to $u_{h\text{free}}$ through the log wind profile similar to equation (3).

†For simplicity, it is hereafter always assumed that $s_r = s_f = s$.

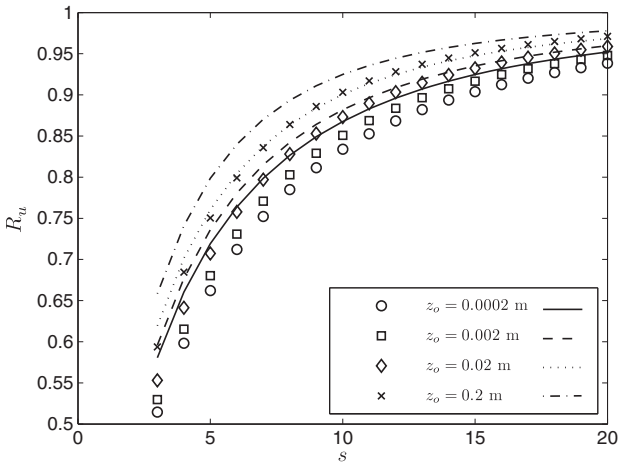


**Figure 2.** Wind speed reduction $R_u$ comparison between the IWFBL models of Frandsen[9] (in markers) and E&F[15] (in lines) for different dimensionless turbine to turbine separations $s$ and surface roughness values $z_o$ (see legend). The models are evaluated with $C_t = 0.88$, $h = 70$ m, $u_{h\text{free}} = 10$ m s$^{-1}$, $z_o = 0.0002$ m, $A_* = 4.53$ and latitude of 55.5°.

MOST to be constant with height within the surface layer; in Emeis[20] and in this study, by correcting the wind shear by using a local $L$ value, we extend its use beyond its original intend, since we further have to assume $L$ to be constant with height above the surface layer and within the wind farm (see more details on these issues in the Section 4).

Because of the different formulations of $l$,[22] this extension can be carried out in several ways, and Emeis[20] tried different forms including $l = \kappa z \phi_m^{-1}$, which was proven to be valid within the surface layer when compared with turbulence measurements and spectra.[23] Since $\Delta z/l$ and $K_2$ are equivalents, we can also extend equations (8) and (9) by using $\phi_m(h/L)$. Further, as Emeis did it for $c_s$, $K_1$ has to be extended for stability conditions by means of the stability correction of the log wind profile $\psi_m$, which comes from the integration of $\phi_m$, so $\psi_m$ is also a function of $z/L$. $u_h$, for example, becomes

$$u_h = \frac{G}{1 + \phi_m(h/L) K_2 \sqrt{c_t + K_1^{-2}}}. \tag{13}$$

However, there is an inconsistency in equation (13) because $u_h$ should equal $u_{h\text{free}}$ when $c_t = 0$. They are indeed equal under neutral conditions because $\phi_m = 1$ and $\psi_m = 0$ for $h/L = 0$. When $h/L \neq 0$, on the other hand, $u_h(c_t = 0)$ from equation (13) becomes $h$-dependent and does not approach the $u_{h\text{free}}$ value.

One way to avoid such 'inconsistency' is by including the stability correction function ($\psi_m$) to the log wind profiles within the two layers in equation (3), so that within the wind farm and at hub height,

$$\boldsymbol{u}_{*1} = \frac{u_h \kappa}{\ln(h/z_o) - \psi_m(h/L)} \tag{14}$$

and

$$\boldsymbol{u}_{*2} = \frac{u_h \kappa}{\ln(h/z_{oo}) - \psi_m(h/L)}. \tag{15}$$

In the absence of a local stability measure at hub height within the wind farm, it is assumed that $L$, in equations 14 and 15, is equal to a stability input given upstream the wind farm. One can work out the derivation of $u_h$, in a similar way as that explained in Section 2.1 (see steps between equations 4–6) and finds (by inserting $z_{oo}$ in equation (5) into (15)).

$$\boldsymbol{u}_{*2} = \frac{\kappa(G - u_h)}{\ln\left(\frac{G}{h f_p}\right) + \psi_m(h/L)}. \tag{16}$$

Therefore, to solve $u_h$ in equation (1), $K_1$ and $K_2$ have to be redefined as $(1/\kappa)\left[\ln(h/z_o) - \psi_m(h/L)\right]$ and $(1/\kappa)\left[\ln[G/(h f_p)] + \psi_m(h/L)\right]$, respectively. The expressions for $u_h$ and $R_u$ are then formally the same as those in equations (8) and (9), also valid for neutral conditions.

However, $A_*$ (included in the modified Coriolis parameter $f_p$ in equation 4) also depends on the state of the atmosphere, as this is close related to the resistance law constants $A$ and $B$, which have been found to vary with stability. This dependency is classically described by extending $A$ and $B$ to be functions of the dimensionless stability parameter $\mu_o = \kappa \boldsymbol{u}_*/(f_c L)$. Despite disagreement among researchers on the forms of $A(\mu_o)$ and $B(\mu_o)$, due to the variety of data used in the different studies and their high uncertainty, it is possible to get empirical formulations for both.[24] On this basis, the dependency of $A_*$ on atmospheric stability, $A_*(\mu_o)$, can be derived (see Appendix A for details).

For a given $u_{h\text{free}}$ value and local stability condition (an $L$ value at a given height upstream the wind farm), $G$ can then iteratively be estimated using the simplified geostrophic drag law, equation (4) (now including the $A_*(\mu_o)$ stability dependence) and the upstream-undisturbed friction velocity $u_{*\text{free}}$ derived from the diabatic wind profile,

$$u_{*\text{free}} = \frac{u_{h\text{free}}\,\kappa}{\ln(h/z_o) - \psi_m(h/L)}. \tag{17}$$

Now, it is important to notice that in the non-neutral cases, $K_2$ depends on $\boldsymbol{u}_*$ through $A_*$:

$$K_2(\boldsymbol{u}_*) = \frac{1}{\kappa}\left[\ln\left(\frac{G}{hf_c}\right) - A_*(\mu_o) + \psi_m(h/L)\right]. \tag{18}$$

Thus, $R_u$ in equation (9) must be modified as

$$R_u = \frac{1 + K_2(u_{*\text{free}})\sqrt{K_1^{-2}}}{1 + K_2(u_{*2})\sqrt{c_t + K_1^{-2}}}, \tag{19}$$

where $\boldsymbol{u}_{*2}$ is found iteratively from the simplified geostrophic drag law but by using the expression for $z_{oo}$ for non-neutral conditions (see Appendix B for its derivation).

$$z_{oo} = h\exp\left[\frac{-\kappa}{\sqrt{c_t + K_1^{-2}}} - \psi_m(h/L)\right]. \tag{20}$$

This procedure ensures that $u_h$, in equation (8) evaluated for $c_t = 0$, gives $u_{h\text{free}}$.

### 2.2.1. Model behavior

Figure 3 shows the extended IWFBL model of Frandsen for a range of dimensionless atmospheric stabilities $h/L$, a number of roughness lengths and a fixed dimensionless turbine to turbine distance. For the range of atmospheric stabilities, $R_u$ always increases with high roughness length values (similar to Figure 2). The striking result is that the variation of

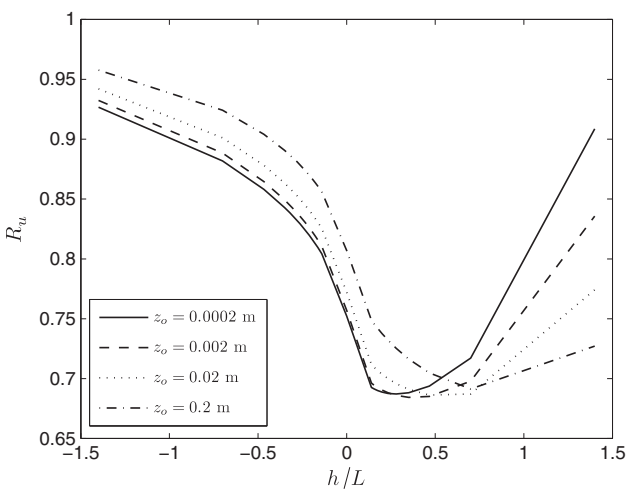


**Figure 3.** The wind-speed reduction $R_u$ of the extended IWFBL model of Frandsen for a range of dimensionless atmospheric stabilities $h/L$, a number of surface roughness values $z_o$ (see legend) and a fixed dimensionless turbine–turbine separation $s = 7$. The model is evaluated with $C_t = 0.88$, $h = 70$ m, $u_{h\text{free}} = 10$ m s$^{-1}$ and latitude of 55.5°.

$R_u$ is much higher for this broad range of atmospheric stabilities than for the rather wide range of roughness lengths, with general low-wind-speed and high-wind-speed reductions under unstable and stable atmospheric conditions, respectively.

At a given positive value of $h/L$ (dependent on the given $z_o$ value), $R_u$ starts to increase with increasing stable conditions. This is because $u_{h\text{free}}$ is used as the only wind-speed input parameter to the model and for this case ($h = 70$ m), and for stable and very stable conditions, such a height is comparable to the BLH that can indeed be below 50–70 m in stable and very stable conditions. MOST (strictly valid for $\sim 10\%$ of the BLH only) then predicts a too high and unrealistic stability correction when estimating $u_{*\text{free}}$ from $u_{h\text{free}}$, which is used for computing $G$ in a range where the stability corrections to the $A$ and $B$ functions and, thus, $A_*$ in the simplified geostrophic drag law is less applicable. A way to avoid the increasing $R_u$ values for stable conditions is by using, as an input parameter for the model, a wind speed not at hub height but at a height well inside the surface boundary layer, where MOST is well applicable.

We can also compare the results for the model of Emeis, i.e., the atmospheric stability-extended IWFBL model of E&F, and the extended IWFBL model of Frandsen for different atmospheric stability conditions and dimensionless turbine to turbine separations. This is illustrated in Figure 4 for an offshore site, where the models have the same behavior with turbine separation distances and atmospheric stability. As for the previous comparisons, the Frandsen's-type model shows larger wind-speed reductions than those from the Emeis'-type model for neutral conditions. For the computed stable and unstable conditions ($L = 100$ m and $L = -50$ m, respectively), the reductions are larger for the Emeis'-type model. This is partly due to the reference height used for the free wind speed; when using a low value for $h$, $R_u$ from Emeis' model becomes higher than that of the extended model of Frandsen under stable conditions.

## 2.3. Wind profiles

We can also compute the spatial average wind profiles within the wind farm (by assuming $L$ to be vertically and horizontally constant), which can be used to analyze the effect of the wind farm in the ABL (not only at hub height) and to compare with the LES results (e.g., those in Lu and Porté-Agel,[12] and Calaf *et al.*,[14]) by using similar functions as those in equations (14) and (15), first by estimating $u_{*\text{free}}$ for the different stability conditions, as in equation (17), which is then used for the estimation of $G$ (by using a stability-corrected $A_*$ value). $z_{oo}$ is directly computed from equation (20). They become

$$u(z \leq h) = \frac{\boldsymbol{u}_{*1}}{\kappa}\left[\ln\left(\frac{z}{z_o}\right) - \psi_m\left(\frac{z}{L}\right)\right] \tag{21}$$

and

$$u(z \geq h) = \frac{\boldsymbol{u}_{*2}}{\kappa}\left[\ln\left(\frac{z}{z_{oo}}\right) - \psi_m\left(\frac{z}{L}\right)\right]. \tag{22}$$

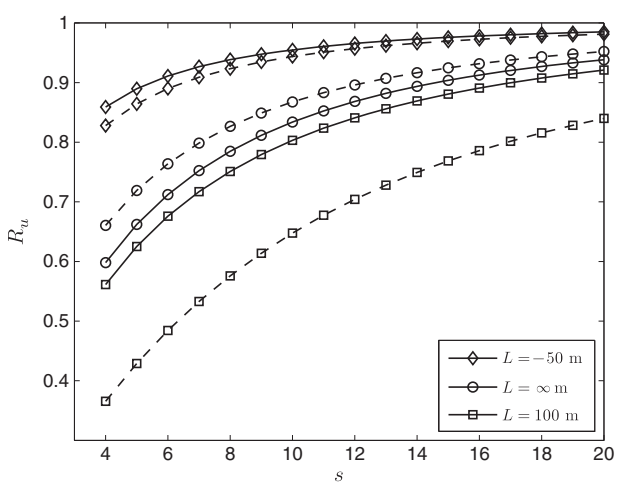


**Figure 4.** A comparison between the wind-speed reduction $R_u$ of the extended IWFBL model by Frandsen (solid lines) and the model by Emeis[20] (dashed lines) for different atmospheric stabilities (see legend) and dimensionless turbine–turbine distances $s$. The models are evaluated with $C_t = 0.88$, $h = 70$ m, $u_{h\text{free}} = 10$ m s$^{-1}$, $z_o = 0.0002$ m and latitude of 55.5°.

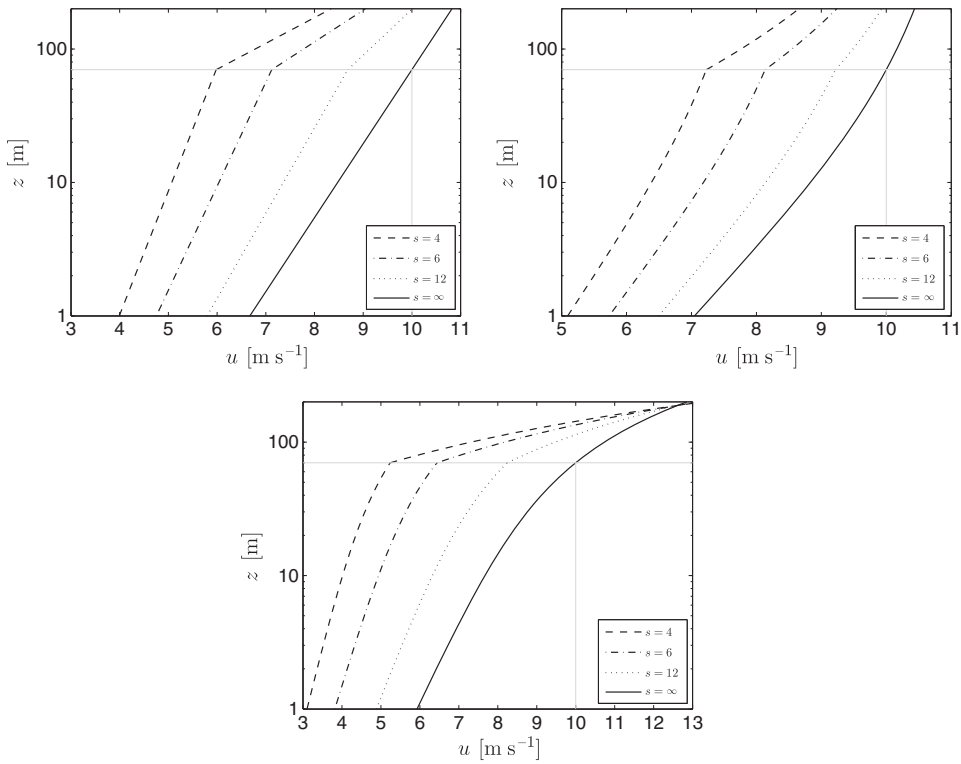


**Figure 5.** Variation of the spatial average wind speed $u$ with height $z$ for the extended IWFBL model by Frandsen within an offshore wind farm ($z_o = 0.0002$ m) for a number of dimensionless turbine–turbine separations $s$ and atmospheric stabilities (top left—$L = \infty$ m, neutral; top right—$L = -200$ m, unstable; and bottom—$L = 200$ m, stable). In gray dotted lines are indicated the hub height ($h = 70$ m) and hub-height free wind-speed ($u_{h\text{free}} = 10$ m s$^{-1}$) levels. The model is evaluated with $C_t = 0.88$ and latitude of 55.5°.

Figure 5 illustrates wind profiles within an offshore wind farm for different dimensionless turbine to turbine separations and atmospheric stability conditions. Except for $s = \infty$ ($c_t = 0$), a kink in the wind profile is distinguished at hub height ($h = 70$ m), as expected. It is interesting to note that all these wind profiles are computed using $u_{h\text{free}} = 10$ m s$^{-1}$, which is equal to the estimation of $u_h$ under all stability conditions and $s = \infty$.

It is important to notice that both layers (above and below $h$) are modeled using the approach of MOST. As $h$ increases, e.g., with larger turbines, the above-$h$ layer will be affected by the BLH and the baroclinicity (among others), and the MOST approach is less valid. Also, the stable corrections from MOST predict very large wind shears for the above-$h$ layer, which lead to wind speeds $u(s \neq 0)$ above the undisturbed ones $u(s = \infty)$ already at 200 m in Figure 5-bottom.

## 3. INFINITE PARK WAKE MODEL

The Park wake model implemented in WAsP is based on the momentum wake model by N. O. Jensen (hereafter known as NOJ),*[25] where the wind speed immediately before the first wake-affected turbine, $u_1$, can be estimated as (Figure 6)

$$u_1 = u_{\text{free}} \left[ 1 - \frac{a}{(1 + k_w\ x/r_o)^2} \right], \tag{23}$$

where $u_{\text{free}}$ is the upstream undisturbed wind speed, $a$ the induction factor ($a = 1 - \sqrt{1 - C_t}$), $k_w$ the momentum entrainment or wake-decay coefficient and $r_o$ the initial wake radius behind the rotor. In the Park wake model, $r_o$ is equal to the turbine's rotor radius $r_r$. Frandsen[9] proposed, by semiempirical means, $k_w \approx 0.5/\ln(h/z_o)$, which suggests that $k_w$ is related to the atmospheric turbulence characteristics because $0.5/\ln(h/z_o) \approx u_{*\text{free}}/u_{h\text{free}}$ under neutral stability conditions.

*Although commonly referred to as a momentum conservation model, NOJ model conserves mass and not momentum within the control volume.

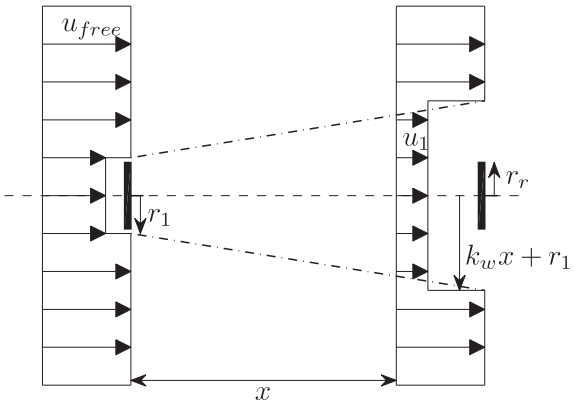


**Figure 6.** Momentum wake model concept by Jensen.[25] The wind speed immediately before a wake-affected turbine $u_1$ is estimated as a function of the distance to the upstream turbine $x$ with rotor radius $r_r$, the free wind speed $u_{\text{free}}$, and the thrust coefficient and the wake-decay coefficient $k_w$.

Therefore, the wind-speed reduction in the Park wake model is also a function of $k_w$. The ground interaction of a wake is modeled by adding the wake reflected at the surface, i.e., a wake seemingly originating from a reflected 'underground rotor'. The surface interaction is then modeled by considering the combined effect of the direct and the reflected wakes. Further, the efficiency of the wind turbine cluster is estimated by combining the effects of four types of overlapping wakes[1]:

1. From directly upwind rotors (NOJs original approach).
2. Reflected 'underground rotors' directly upwind.
3. Shading rotors upwind but left or right to the wind direction.
4. Reflected shading 'underground rotors' upwind but left or right to the wind direction.

The combined effect of two or more overlapping wakes on a downwind rotor was modeled through an empirical quadratic summation rule.[1] Here, the partial wake overlap with a rotor is considered by applying the overlap fraction to the speed deficits of the individual wake. Thus, the rotor diameter is required as an input to the model. Rathmann *et al.*[26] analytically solved the contribution of the four types of wakes (described earlier) for an asymptotically infinite number of wind turbines. This is described here as the 'infinite Park wake model' (IPW) (Appendix C).

### 3.1. Adjusted wake-decay coefficient for the infinite Park wake model

When using the Park wake model, we are required of the wake-decay coefficient for the particular site. To a first approximation, it is common procedure and recommended to use $k_w = 0.050$ and $k_w = 0.075$ when performing wake analysis in WAsP over sea and land surfaces, respectively. However, $k_w$ should be estimated for the particular $z_o$ value and atmospheric stability condition of the site, since $k_w \approx u_{*\text{free}}/u_{h\text{free}} = \kappa/[\ln(h/z_o) - \psi_m(h/L)]$, where the correction due to atmospheric stability $\psi_m$ is here already considered from that form proposed by Frandsen.[9] This already results in much lower $k_w$ values than those recommended in WAsP for a wide range of roughness values and stabilities; $k_w$ is lower for low compared with high roughness values and higher for unstable compared with stable conditions.

Figure 7 compares the wind-speed reduction from the IPW model—when using two types of $k_w$-values: from the form $k_w = u_{*\text{free}}/u_{h\text{free}}$, as shown earlier (so we again assume $L$ to be invariant within the wind farm), and the WAsP-$k_w$ values—with that from the IWFBL model by Frandsen for neutral conditions, different dimensionless turbine to turbine separations and a number of roughness lengths. The IPW model shows the same behavior as the IWFBL model, i.e., the higher the wind-speed reductions, the smoother the terrain and the shortest the turbine to turbine separation. The IPW model using the WAsP-$k_w$ values shows similar reductions compared with the IWFBL model, slightly higher ones for offshore conditions. The IPW model using $k_w = u_{*\text{free}}/u_{h\text{free}}$ shows much higher reductions compared with the IWFBL model for all roughness lengths and similar ones to the IPW model using the WAsP-$k_w$ value for $z_o = 0.2$ m only. This result already illustrates that the recommended WAsP-$k_w$ values seem to be too high for wind farms located on flat and homogeneous terrain, except for areas with high roughness values such as forests.

When the IPW model is adjusted so that it gives the same wind-speed reductions as those of the IWFBL model of Frandsen, $k_w$ has to be modified/adjusted, and thus, it becomes dependent not only on $z_o$ ($k_w$ increases with increasing $z_o$ values) but also on turbine separation as shown in Figure 8. The 'adjusted' $k_w$ values are generally much lower for smaller

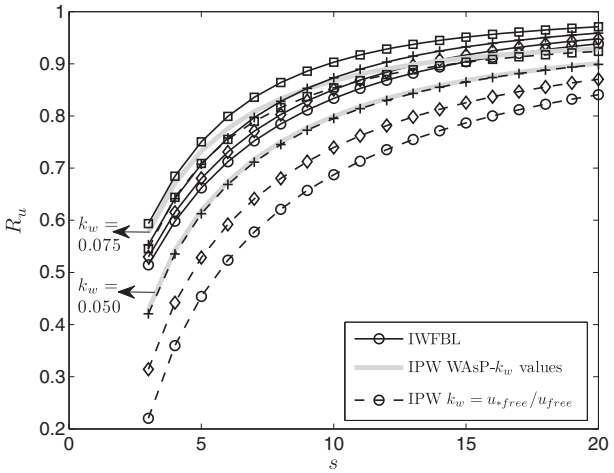


**Figure 7.** Comparison of the wind-speed reduction $R_u$ between the IWFBL model of Frandsen[9] (solid lines with markers) and the IPW model for neutral conditions (by using the form $k_w = u_{*\text{free}}/u_{h\text{free}}$), a number of roughness values (∘ $z_o = 0.0002$ m, ⋄ $z_o = 0.002$ m, + $z_o = 0.02$ m and □ $z_o = 0.2$ m) and dimensionless turbine–turbine separations $s$. The IPW model is also evaluated with the recommended WAsP-$k_w$ values (0.075 and 0.050 in gray solid lines). All models are evaluated with $h = 70$ m, $D_r = 80$ m, $A_* = 4.53$, $u_{h\text{free}} = 10$ m s$^{-1}$ and latitude of 55.5°.

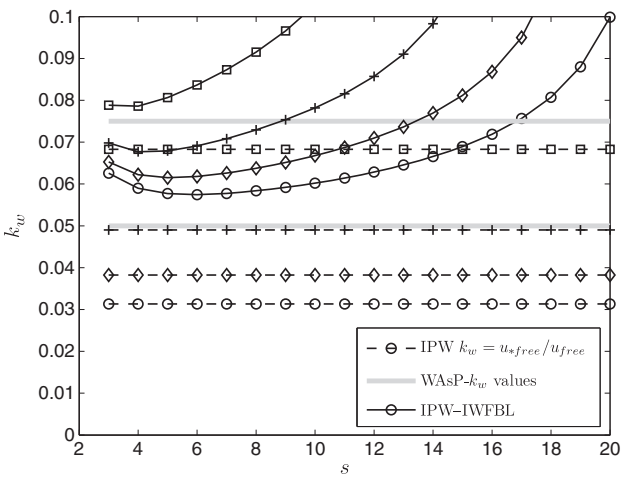


**Figure 8.** Variation of the wake-decay coefficient $k_w$ (i) by assuming the form $k_w = u_{*\text{free}}/u_{h\text{free}}$, (ii) by using the WAsP recommended values and (iii) by using adjusted $k_w$ values so that the IPW model matches the wind-speed reductions of the IWFBL model by Frandsen[9] for neutral conditions, a number of roughness values (as in Figure 7) and dimensionless turbine–turbine separations $s$. The models are evaluated with $h = 70$ m, $D_r = 80$ m, $A_* = 4.53$, $u_{h\text{free}} = 10$ m s$^{-1}$ and latitude of 55.5°.

than for larger turbine separations and lower than the WAsP-$k_w$ values for $z_o = 0.002$—0.02 m and $s < 10$. The lowest $k_w$ values are given by the form $k_w = u_{*\text{free}}/u_{h\text{free}}$, which does not take the turbine separation into account.

In a similar fashion, a constant turbine to turbine distance, e.g., $s = 7$, can be used to analyze the behavior of the wind-speed reduction $R_u$ for different atmospheric stability conditions and roughness lengths. This is illustrated in Figure 9. The wind-speed reductions for the IPW model using the form $k_w = u_{*free}/u_{h\text{free}}$ are generally higher than those for the extended IWFBL model by Frandsen, except for $z_o = 0.2$ m and a range of neutral to stable conditions. The results of the extended IWFBL model by Frandsen show an increase of $R_u$ at a given positive $h/L$ value because, as mentioned earlier, the reference wind speed is too high and MOST might be not longer valid. $R_u$ does not vary with atmospheric stability in the IPW model as strongly (stability is accounted for through $k_w$ only) as it does in the extended IWFBL model of Frandsen. The IPW model using the WAsP-$k_w$ values shows similar reductions compared with those from the extended IWFBL model of Frandsen only for atmospheric conditions close to neutral.

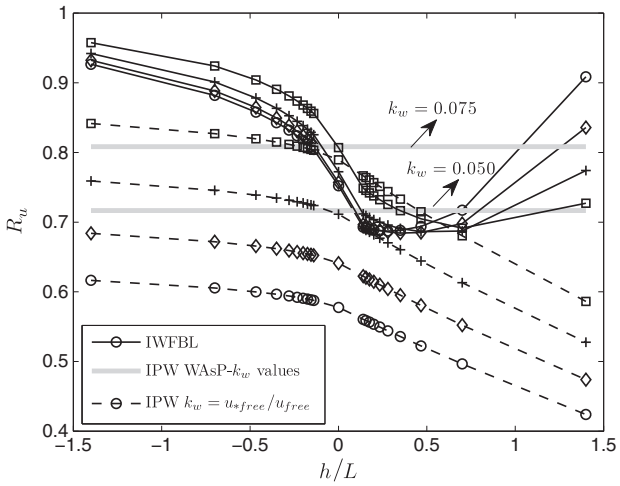


**Figure 9.** As in Figure 7 but for a range of dimensionless atmospheric stability conditions $h/L$ and a constant dimensionless turbine–turbine separation $s = 7$. The models are evaluated with $h = 70$ m, $D_r = 80$ m, $u_{h\text{free}} = 10$ m s$^{-1}$ and latitude of 55.5°.

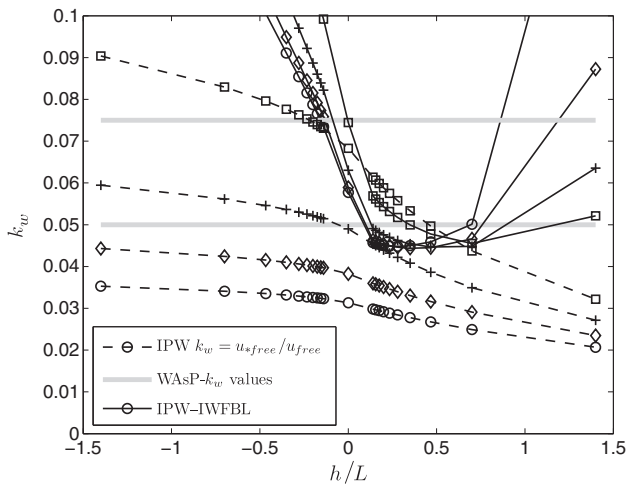


**Figure 10.** As in Figure 8 but for a range of dimensionless atmospheric stability conditions $h/L$ and a constant dimensionless turbine–turbine separation $s = 7$. The models are evaluated with $h = 70$ m, $D_r = 80$ m, $u_{h\text{free}} = 10$ m s$^{-1}$ and latitude of 55.5°.

The correspondent adjusted wake-decay coefficients, found when matching the wind-speed reduction of the IPW model to that of the extended IWFBL model of Frandsen for the different atmospheric stability conditions in Figure 9, are illustrated in Figure 10. The behavior of $k_w$ with stability when assuming $k_w = u_{*\text{free}}/u_{h\text{free}}$ is similar to that found with the adjusted wake-decay coefficients for all roughness lengths, i.e., a decrease of the wake-decay coefficient the more stable the atmosphere, and generally shows the lowest $k_w$ values (except when compared with the adjusted values for a narrow range of stable conditions and $z_o = 0.2$ m). The adjusted values tend to be much lower than the WAsP-recommended ones for a wide range of neutral to stable conditions and all roughness lengths. The increase of the adjusted $k_w$ is due to the increase in $R_u$ at the same stable $h/L$ range, a behavior which disappears when the reference undisturbed wind speed is taken at a height within the surface boundary layer.

## 4. DISCUSSION

In this paper, $k_w$ in the Park wake model for the infinite wind farm is, among others, adjusted so that the model matches the value of the wind-speed reduction of the extended IWFBL model of Frandsen. In a similar fashion, the adjustment can be performed using the IWFBL model of Emeis, which also shows that the WAsP-recommended values for $k_w$ are generally

large for land-type roughness and short turbine separations. There are other WPW models, which use the $k_w$ parameter, and here, we choose the Park wake model because it considers (among others) the effect of adjacent turbines, is a commonly used model and is the base of wind power calculations in WAsP. However, direct comparison and matching of the models are not totally fair because the wind-speed reduction estimated from the IWFBL models is related to the spatial average wind speed within the wind farm, whereas that from the IPW model is related to the wind speed immediately before the last turbine.

From our findings, we do not suggest to use the results for the wake-decay coefficient when performing wind power calculations directly, since the analysis is performed on the basis of the assumption either that $k_w = u_{*\mathrm{free}}/u_{h\mathrm{free}}$ or that of an infinite wind farm and in reality, only a couple of wind farms might be treated as such. For a finite but large wind farm, the first wake-affected turbines experience a rather different wake regime than those at the final rows perpendicular to the mean undisturbed wind direction and, therefore, $k_w$ should be slightly decreased with downstream distance to values similar to ours under close turbine separations and near-stable conditions. An interesting and similar approach was shown by Rathmann *et al.*[26], in which after the $k_w$ of the IPW model is adjusted to the IWFBL model of Frandsen, the WAsP-recommended $k_w$ value in the Park model is gradually modified to asymptotically approach the infinite $k_w$ value for 'deep' positions in the wind farm via a relaxation constant. Their approach agreed better than only assuming the WAsP-recommended values when compared with data from the Horns Rev and Nysted wind farms.

As wind turbines become larger, the IWFBL models have to be extended to account for effects that are normally not considered for small–medium turbines, which are well inside the surface boundary layer, such as the BLH. As illustrated in Figure 5, particularly for stable conditions, the wind speed predicted using MOST highly and sometimes unrealistically increases with height, and the addition of the BLH as a wind profile parameter will damp such unrealistic growth, as shown in the wind profile models by Peña *et al.*[10] over the sea, and Peña *et al.*[22] and Gryning *et al.*[27] over land. Unfortunately, from our knowledge, there is still a lack of BLH data for wind energy purposes, which can be used for model comparison.

Frandsen[28] attempted to compare theoretical wind-farm efficiencies by assuming that the change in roughness imposed by the infinite wind farm can be modeled as a smooth-to-rough generated internal boundary layer (IBL) to those derived from 'traditional' IBL models such as that of Miyake,[29] also used in WAsP for natural roughness transitions, finding similar results for an infinite row of turbines. However, as shown in Floors *et al.*,[30] although the IBL models give good results for neutral atmospheric conditions, observations of the IBL height show a strong dependency on atmospheric stability, which is normally neglected in the IBL models because it is generally believed that the mechanical contribution dominates the IBL growth. Since from our results the efficiency of the wind farm strongly depends on atmospheric stability, the question arises on how the IBL models can be adjusted for wind-farm efficiency analysis under different atmospheric conditions. Wind speeds within and downstream the wind farm are therefore needed to validate, for example, how accurate equation (20) describes the wind-farm characteristics by applying it to roughness models such as that in WAsP.

As previously mentioned, our results are difficult to compare with observations, since their analysis is at least as challenging as the modeling itself. Gaumond[16] found, for example, that the degree of accuracy of wake models evaluated for large offshore wind farms is much more dependent on the way data and simulations are post-processed than the physics of the models itself. There are, however, studies intending to reproduce the effects of large arrays of turbines on boundary layers by using LES techniques. Calaf *et al.*[14] 'immersed' medium-size and large-size arrays of turbines in a neutral boundary layer, and for all the different cases (varying the geometrical loading, aspect ratios $s_r/s_f$ and roughness values), the LES-based average velocity profiles as stated in Calaf *et al.*[14] 'clearly showed the existence of two log laws above and below the turbine region', verifying the fundamental assumption of the IWFBL model of Frandsen. From their LES results, they proposed a new formulation of $z_{oo}$ on the basis of that of Frandsen *et al.*[31] As their analysis of $z_{oo}$, our proposed expression in equation (20), is not very sensitive to the background roughness $z_o$ but to atmospheric stability, which can be incorporated to those expressions in Calaf *et al.*,[14] and Meyers and Meneveau.[13] Lu and Porté-Agel,[12] on the other hand, studied an infinite large wind farm by horizontally applying periodic boundary conditions in a LES of the stable boundary layer covering a wind turbine. The shapes of their average velocity profiles are in good agreement with those in Calaf *et al.*,[14] and they found that the stable BLH considerably increased with simulation time, attributing this effect to radial and vertical wake expansions. We certainly believe that this is partly the case, but the BLH also increases because for all stability conditions, the above hub-height friction velocity, $\boldsymbol{u}_{*2}$, is higher than $u_{*\mathrm{free}}$, which ends up lifting the BLH (in our model $\boldsymbol{u}_{*2}$ is about twice the value of $u_{*\mathrm{free}}$ for stable conditions).

Here, we assume the local 'undisturbed' hub-height value of $L$ to be representative of the upstream atmospheric stability conditions within the surface layer and higher (in cases where $h$ is above it) and within the infinite wind farm. The local stability conditions inside wind farms actually vary because of the presence of the turbines, which change both the local momentum and buoyancy fluxes ($L$ is related to the ratio between both) as Zhang *et al.*[32] showed from wind-tunnel experiments. Therefore, the vertical and horizontal stability homogeneity assumption does not probably hold, but this needs to be further investigated as there is a lack of experimental data to verify it. The models here presented predict the change of momentum flux, but there is no formulation for the buoyancy flux. Lu and Porté-Agel[12] showed that the presence of the turbines reduced the undisturbed surface friction velocity from 0.27 m s$^{-1}$ to 0.23 m s$^{-1}$ ($s = 8$) and 0.21 m s$^{-1}$ ($s = 5$) (we find the same reductions for a wide range of roughness values, 0.0002 m $\ll z_o \ll$ 0.2 m, and neutral conditions), whereas

the undisturbed buoyancy flux ($-4.3 \times 10^{-4}$ m$^2$ s$^{-3}$) becomes $-3.8 \times 10^{-4}$ m$^2$ s$^{-3}$ ($s = 8$) and $-3.2 \times 10^{-4}$ m$^2$ s$^{-3}$ ($s = 8$). In terms of stability, this means a slight increase of instability from $L = 45$ m to $L = 32$ m and $L = 28$ m, respectively. Calaf *et al.*,[33] also using LES, found a scalar flux increasing within the wind farm by about 10–20%, which is in contrast with Zhang *et al.*'s reduction of the heat flux of 4% (in Zhang *et al.*,[32] the differences between the maximum and minimum heat fluxes are up to 12–7%).

## 5. CONCLUSIONS

The Park wake model has been used to derive the wind-speed reduction asymptotically reached by an infinite array of wind turbines and compared with the wind-speed reduction of the boundary-layer model of Frandsen for the infinite wind farm. The models show the same behavior for different dimensionless turbine to turbine separations and surface roughness lengths; the higher the roughness length and the longer the turbine separation, the lower the wind-speed reduction. The IPW model generally shows the highest wind-speed reductions, by assuming the form $k_w = u_{*\text{free}}/u_{h\text{free}}$ compared with those of the IWFBL model.

The IWFBL model of Frandsen has been extended to account for atmospheric static stability conditions (by assuming horizontal and vertical stability homogeneity) and shows a similar behavior with stability when compared with the IWFBL model of Emeis (the stability extended model of E&F); the more stable the atmosphere, the higher the wind-speed reduction, being the relative wind-speed reduction due to stability much higher than that due to surface roughness lengths (a wide range of roughness lengths has been considered). Emeis' model estimates lower wind-speed reductions than Frandsen's model for neutral conditions only and a wide range of wind speeds.

The extended IWFBL model of Frandsen shows that to get an increasing wind-speed reduction when going from neutral to stable conditions, it is required that the inputs to the model (i.e., the reference wind speed and atmospheric stability) are given close to the surface where MOST is fully valid. This results in a good estimation of the stability-corrected undisturbed friction velocity, which in turn provides a reasonable estimation of the geostrophic wind speed by using the stability-corrected $A_*$ value.

The IWFBL model by Frandsen is the only one of the models here studied that is dependent on wind speed not only through the $C_t$ curve of the turbine but also because it is geostrophic wind speed dependent. Thus, for a nearly constant $C_t$ value, the wind-speed reduction increases anyway. However, at this stage, it is difficult to judge the quality of the models, since the IWFBL models, for example, either assume, among others, a relation between the mixing length and the height where the wind is undisturbed or a relation between the geostrophic and the hub-height wind-farm wind speed. Also, we do not validate the models against wind-farm data, but we expect to do so in the near future.

Finally, and most importantly, we are able to calibrate the 'more realistic' and more complex Park wake model to match the wind-speed reduction of the extended IWFBL model of Frandsen for different wind speeds, roughness values, turbine separations, turbine characteristics and atmospheric stability conditions by adjusting the value of the wake-decay coefficient, considering an infinite array of wind turbines. Already for neutral conditions, the $k_w$ values are generally lower than those normally recommended by WAsP for wind power calculations for a number of surface roughness lengths and turbine separations lower than 10 rotor diameters. They are also strongly dependent on atmospheric stability, decreasing as the atmosphere becomes more stable, higher than the WAsP-recommended values for a number of roughness lengths under very unstable atmospheric conditions and much lower than those WAsP-recommended under neutral and a wide range of stable atmospheric conditions.

## ACKNOWLEDGEMENTS

This work could not be possible without the lifetime work efforts of the late Sten T. Frandsen. Funding from the Danish Public Service Obligation (PSO) to the 'Windshadow' project, Energinet.dk 10086, and from the EERA-DTOC project is acknowledged. This work is performed in participation to the IEA-WakeBench research collaboration project. We would also like to thank Pierre-Elouan Réthoré and Søren Ott from DTU Wind Energy, Rebecca Barthelmie and the reviewers for the very useful comments on the manuscript.

## APPENDIX A: SIMPLIFIED GEOSTROPHIC DRAG LAW DEPENDENCY ON ATMOSPHERIC STABILITY

The geostrophic drag law is given as

$$G = \frac{\boldsymbol{u}_*}{\kappa}\left(\left[\ln\left(\frac{\boldsymbol{u}_*}{f_c z_o}\right) - A(\mu_o)\right]^2 + B(\mu_o)^2\right)^{1/2}, \tag{24}$$

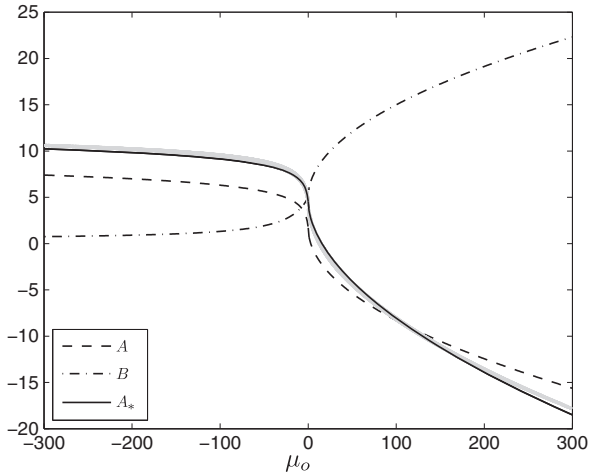


**Figure 11.** The dependency of the $A$, $B$ and $A_*$ parameters of the resistance laws on the dimensionless stability parameter $\mu_o$. The gray points are the adjustment of $A_*$ (equation (29)), to match the geostrophic wind from equation (24). The solid line corresponds to the forms $A_*(\mu_o \geq 0) = 4.53 - \mu_o^{0.55}$ and $A_*(\mu_o \leq 0) = 4.53 + \ln(1 - \mu_o)$.

where $A(\mu_o)$ and $B(\mu_o)$ depend on atmospheric stability since $\mu_o = \kappa \boldsymbol{u}_*/(f_c L)$.[19] Because of the scatter of the observations, there are numerous formulations for $A(\mu_o)$ and $B(\mu_o)$. We choose to use those of Jensen *et al.*[24] but with the values for neutral conditions ($\mu_o = 0$) adjusted to match the recent results of Peña *et al.*[22] and in consistency with the values used for the European Wind Atlas.[3]

$$A(\mu_o \geq 0) = 1.7 - \mu_o^{1/2}, \tag{25}$$

$$A(\mu_o \leq 0) = 1.7 + \ln(1 - \mu_o), \tag{26}$$

$$B(\mu_o \geq 0) = 5 + \mu_o^{1/2}, \tag{27}$$

$$B(\mu_o \leq 0) = \frac{5 - \kappa}{1 - \mu_o/25} + \kappa. \tag{28}$$

In the original formulation of Jensen *et al.*,[24] $\mu_o = u_*/(f_c L)$. However, we choose to include $\kappa$ in $\mu_o$, as in Zilitinkevich,[19] and Long and Guffey,[34] because the points used by Jensen *et al.*[24] to derive equations (25)–(27) were taken from the study of the Wangara data by Clarke and Hess,[35] where $\mu_o = \kappa \boldsymbol{u}_*/(f_c L)$.

For a range of dimensionless stabilities, $G$ is computed from equation (24) by using the forms in equations (25)–(27). The result can then be used to estimate $A_*$ from rearranging the simplified geostrophic drag law, in equation (4).

$$A_* = \ln\left(\frac{G}{f_c z_o}\right) - \frac{\kappa G}{\boldsymbol{u}_*}. \tag{29}$$

Figure 11 illustrates the results of such analysis, where an analytical form for $A_*(\mu_o)$ is also given.

## APPENDIX B: EFFECTIVE WIND-FARM ROUGHNESS LENGTH

From equation (15), one can easily derive

$$\ln\left(\frac{z_{oo}}{h}\right) = -\frac{\kappa\, u_h}{u_{*2}} - \psi_m(h/L), \tag{30}$$

where the ratio $u_h/\boldsymbol{u}_{*2}$ can be replaced by $1/\sqrt{(\boldsymbol{u}_{*1}/u_h)^2 + c_t}$ from equation (1). Since $\boldsymbol{u}_{*1}/u_h = K_1^{-1}$, equation (30) then reads as

$$\ln\left(\frac{z_{oo}}{h}\right) = -\frac{\kappa}{\sqrt{c_t + K_1^{-2}}} - \psi_m(h/L), \tag{31}$$

from which $z_{oo}$ can be derived (Frandsen *et al.*[31] deduced a similar form for neutral conditions only). It should be noted that the dependency on atmospheric stability of $z_{oo}$ is through $\psi_m(h/L)$ and $K_1$, which also depends on $\psi_m(h/L)$.

## APPENDIX C: THE INFINITE PARK WAKE MODEL

The total wake deficit $\delta_T = 1 - R_u$ of the Park wake model implemented in WAsP is estimated as the quadratic sum of four types of overlapping wakes:

$$\delta_T^2 = \delta_{\mathrm{I}}^2 + \delta_{\mathrm{II}}^2 + \delta_{\mathrm{III}}^2 + \delta_{\mathrm{IV}}^2. \tag{32}$$

The first term corresponds to the wakes directly upwind:

$$\delta_{\mathrm{I}}^2 = \delta_o^2 \sum_{j=1}^{\infty} d_w(s_j)^{-4} = \delta_o^2 \sum_{j=1}^{\infty} (1 + 2k_w s_r j)^{-4}, \tag{33}$$

where $\delta_o$ is the initial wake deficit, $\delta_o = \left(1 - \sqrt{1 - C_t}\right)$, $d_w$ is a dimensionless wake diameter, $d_w = D_w/D_r$, with $D_w$ as the wake diameter, $D_w = D_r(1 + 2k_w s_r)$, and $j$ is the number of rows upwind from the considered turbine.

The second term corresponds to the reflected 'underground rotors' directly upwind:

$$\delta_{\mathrm{II}}^2 = \delta_o^2 \sum_{j=m_{\mathrm{II}}}^{\infty} d_w(s_j)^{-4} = \delta_o^2 \sum_{j=m_{\mathrm{II}}}^{\infty} (1 + 2k_w s_r j)^{-4}, \tag{34}$$

where $m$ is the number of minimum rows to the first upwind row from where this type of wake has an effect on the considered turbine; in this case, $m_{\mathrm{II}} = (2h/D_r - 0.5)/(k_w s_r)$.

The third term corresponds to the shading rotors upwind but left or right to the wind direction:

$$\delta_{\mathrm{III}}^2 = \delta_o^2 \sum_{j=m_{\mathrm{III}}}^{\infty} 2N_{\mathrm{III}}(s_j) d_w(s_j)^{-4}, \tag{35}$$

where $N_{\mathrm{III}}$ is the number of turbines to the left and to the right of the wind direction that are able to throw their wake onto the considered turbine, $N_{\mathrm{III}}(s_j) = d_w(s_j)/(2s_f)$ and $m_{\mathrm{III}} = (s_f - 0.5)/(k_w s_r)$, so equation (35) becomes

$$\delta_{\mathrm{III}}^2 = \delta_o^2 \sum_{j=m_{\mathrm{III}}}^{\infty} \frac{d_w(s_j)}{s_f} d_w(s_j)^{-4} = \frac{\delta_o^2}{s_f} \sum_{j=m_{\mathrm{III}}}^{\infty} (1 + 2k_w s_r j)^{-3}. \tag{36}$$

The fourth term corresponds to the reflected shading 'underground rotors' upwind but left or right to the wind direction:

$$\delta_{\mathrm{IV}}^2 = \delta_o^2 \sum_{j=m_{\mathrm{IV}}}^{\infty} 2N_{\mathrm{IV}}(s_j) d_w(s_j)^{-4}, \tag{37}$$

where $N_{\mathrm{IV}}(s_j) = \sqrt{d_w(s_j)^2 - (4h/D_r)^2}/(2s_f)$ is the number of turbines to the left and to the right of the wind direction that are able to throw a reflected wake onto the considered turbine and $m_{\mathrm{IV}} = \left(\sqrt{s_f^2 + (2h/D_r)^2} - 0.5\right)/(k_w s_r)$, so equation (37) becomes

$$\delta_{\mathrm{IV}}^2 = \delta_o^2 \sum_{j=m_{\mathrm{IV}}}^{\infty} \frac{\sqrt{d_w(s_j)^2 - (4h/D_r)^2}}{s_f} d_w(s_j)^{-4} = \frac{\delta_o^2}{s_f} \sum_{j=m_{\mathrm{IV}}}^{\infty} \frac{\sqrt{(1 + 2k_w s_r j)^2 - (4h/D_r)^2}}{(1 + 2k_w s_r j)^4}. \tag{38}$$

The infinite sums converge and can be computed as

$$\delta_{\mathrm{I}}^2 = \frac{\delta_o^2 \ \mathrm{psi}\left[3, 1 + (2\, s_r\, k_w)^{-1}\right]}{96\, s_r^4\, k_w^4} \tag{39}$$

$$\approx \frac{\delta_o^2}{(1 + 2k_w s_r)^3}\left[\frac{1}{2(1 + 2k_w s_r)} + \frac{1}{6k_w s_r}\right], \tag{40}$$

$$\delta_{\mathrm{II}}^2 = \frac{0.0104167\, \delta_o^2 \ \mathrm{psi}\left[3, 2\, h/(s_r\, k_w)\right]}{s_r^4\, k_w^4} \tag{41}$$

$$\approx \frac{\delta_o^2}{128(h/D_r)^3}\left[\frac{1}{4(h/D_r)} + \frac{1}{3k_w s_r}\right] \tag{42}$$

$$\delta_{\mathrm{III}}^2 = \frac{-0.0625\, \delta_o^2 \ \mathrm{psi}\left[2, s_f/(s_r\, k_w)\right]}{s_f\, s_r^3\, k_w^3} \tag{43}$$

$$\approx \frac{\delta_o^2}{16 s_f^4}\left(1 + \frac{s_f/s_r}{k_w}\right), \quad \text{and} \tag{44}$$

$$\delta_{\mathrm{IV}}^2 \approx \frac{\delta_o^2}{16 s_f^4}\left[(1 + 4[(h/D_r)/s_f]^2)^{-2} + \left(\frac{s_f/s_r}{k_w}\right)\left(\frac{1 - [1 + 4([h/D_r]/s_f)^2]^{-3/2}}{6[(h/D_r)/s_f]^2}\right)\right]. \tag{45}$$

When using these last four results, one assumes that $C_t$ is constant throughout the array, i.e., it does not strongly vary within the range of reduced wind speeds.

## REFERENCES


1. Katic I, Højstrup J, Jensen NO. A simple model for cluster efficiency, *Proceedings of the European Wind Energy Association Conference & Exhibition*, 1986.
2. Mortensen NG, Heathfield DN, Myllerup L, Landberg L, Rathmann O. Getting started with WAsP 9. *Risø-I-2571(EN)*, Risø National Laboratory, Roskilde, *http:/www.wasp.dk/Download/DownloadFiles/General/Getting Started with WAsP 9.pdf*, 2007.
3. Troen I, Petersen EL. *European Wind Atlas*. Risø National Laboratory, Roskilde, 1989.
4. Peña A, Hahmann AN. Atmospheric stability and turbulent fluxes at Horns Rev—an intercomparison of sonic, bulk and WRF model data. *Wind Energy* 2012; **15**: 717–730.
5. Jensen LE. Array efficiency at Horns Rev and the effect of atmospheric stability, *Proceedings of the European Wind Energy Association Conference & Exhibition*, Milano, 2007.
6. Barthelmie R, Jensen LE. Evaluation of wind farm efficiency and wind turbine wakes at the Nysted offshore wind farm. *Wind Energy* 2010; **13**: 573–586.
7. Vincent CL, Pinson P, Giebel G. Wind fluctuations over the North Sea. *International Journal of Climatology* 2010. in press.
8. Sathe A, Gryning S-E, Peña A. Comparison of the atmospheric stability and wind profiles at two wind farm sites over a long marine fetch in the North Sea. *Wind Energy* 2011. in press.
9. Frandsen S. On the wind speed reduction in the center of large clusters of wind turbines. *Journal of Wind Engineering and Industrial Aerodynamics* 1992; **39**: 251–265.
10. Peña A, Gryning S-E, Hasager CB. Measurements and modelling of the wind speed profile in the marine atmospheric boundary layer. *Boundary-Layer Meteorology* 2008; **129**: 479–495.
11. Vermeer LJ, Sørensen JN, Crespo A. Wind turbine wake aerodynamics. *Progress in Aerospace Sciences* 2003; **39**: 467–510.
12. Lu H, Porté-Agel F. Large-eddy simulation of a very large wind farm in a stable atmospheric boundary layer. *Physics of Fluids* 2011; **23**: 065101 (1–19).
13. Meyers J, Meneveau C. Optimal turbine spacing in fully developed wind farm boundary layers. *Wind Energy* 2011. in press.

14. Calaf M, Meneveau C, Meyers J. Large eddy simulation study of fully developed wind-turbine array boundary layers. *Physics of Fluids* 2010; **22**: 015110 (1–16).
15. Emeis S, Frandsen S. Reduction of horizontal wind speed in a boundary layer with obstacles. *Boundary-Layer Meteorology* 1993; **64**: 297–305.
16. Gaumond M, Rethoré P-E, Ott S, Peña A, Bechmann A, Hansen KS. Evaluation of the wind direction uncertainty and its impact on wake modelling at the Horns Rev offshore wind farm. *Wind Energy* 2013. in press.
17. Jensen NO. Change of surface roughness and the planetary boundary layer. *Quarterly Journal of the Royal Meteorological Society* 1978; **104**: 351–356.
18. Rethoré P-E. Wind turbine wake in atmospheric turbulence. *Technical Report Risoe-PhD-53(EN)*, Risø DTU, Roskilde, 2009.
19. Zilitinkevich SS. Resistance laws and prediction equations for the depth of the planetary boundary layer. *Journal of Atmospheric Sciences* 1975; **32**: 741–752.
20. Emeis S. A simple analytical wind park model considering atmospheric stability. *Wind Energy* 2010; **13**: 459–469.
21. Monin AS, Obukhov AM. Osnovnye zakonomernosti turbulentnogo peremeshivanija v prizemnom sloe atmosfery (basic laws of turbulent mixing in the atmosphere near the ground). *Trudy Geofizicheskogo Instituta AN SSSR* 1954; **24**(151): 163–187.
22. Peña A, Gryning S-E, Hasager CB. Comparing mixing-length models of the diabatic wind profile over homogeneous terrain. *Theoretical and Applied Climatology* 2010; **100**: 325–335.
23. Peña A, Gryning S-E, Mann J. On the length-scale of the wind profile. *Quarterly Journal of the Royal Meteorological Society* 2010; **136**: 2119–2131.
24. Jensen NO, Petersen EL, Troen I. Extrapolation of mean wind statistics with special regard to wind energy applications. *Technical Report WCP–86, WMO/TF–No. 15*, World Meteorological Organization, 1984.
25. Jensen NO. A note on wind generator interaction. *Technical Report Risoe-M-2411(EN)*, Risø National Laboratory, Roskilde, 1983.
26. Rathmann OS, Frandsen S, Nielsen M. Wake decay constant for the infinite wind turbine array, *Proceedings of the European Wind Energy Association Conference & Exhibition*, Warsaw, 2010.
27. Gryning S-E, Batchvarova E, Brümmer B, Jørgensen H, Larsen S. On the extension of the wind profile over homogeneous terrain beyond the surface layer. *Boundary-Layer Meteorology* 2007; **124**: 251–268.
28. Frandsen ST. Turbulence and turbulence-generated structural loading in wind turbine clusters. *Technical Report Risoe-R-1188(EN)*, Risø DTU, Roskilde, 2007.
29. Miyake M. Transformation of the atmospheric boundary layer over inhomogeneous surfaces. *Technical Report Unpublished MSc. Thesis, Science Report 5R-6*, University of Washington, Seattle, 1965.
30. Floors R, Gryning S-E, Peña A, Batchvarova E. Analysis of diabatic flow modification in the internal boundary layer. *Meteorologische Zeitschrift* 2011; **20**: 649–659.
31. Frandsen S, Barthelmie R, Pryor S, Rathmann O, Larsen S, Højstrup J, Thøgersen M. Analytical modelling of wind speed deficit in large offshore wind farms. *Wind Energy* 2006; **9**: 39–53.
32. Zhang W, Markfort CD, Porté-Agel F. Experimental study of the impact of large-scale wind farms on land-atmosphere exchanges. *Environmental Research Letters* 2013; **8**: 015002 (8 pp).
33. Calaf M, Parlange MB, Meneveau C. Large eddy simulation study of scalar transport in fully developed wind-turbine array boundary layers. *Physics of Fluids* 2010; **23**: 126603 (1–16).
34. Long RR, Guffey LJ. Drag and heat transfer relations for the planetary boundary layer. *Boundary-Layer Meteorology* 1977; **11**: 363–373.
35. Clarke RH, Hess GD. Geostrophic departure and the functions a and b of rossby-number similarity theory. *Boundary-Layer Meteorology* 1974; **7**: 267–287.

THE EUROPEAN ENERGY RESEARCH ALLIANCE
DESIGN TOOLS FOR OFFSHORE WIND FARM CLUSTER

# *WP1 wake model performance validation results for Horns Rev offshore wind farm*

***Kurt S. Hansen - DTU Wind Energy***
***E-Mail: kuhan@dtu.dk***

July, 2013, version 4

| | |
|---|---|
| Agreement n.: | FP7-ENERGY-2011-1/ n°282797 |
| Duration | January 2012 to June 2015 |
| Co-ordinator: | DTU Wind Energy, Risø Campus, Denmark |

Support by:

SEVENTH FRAMEWORK PROGRAMME

PROPRIETARY RIGHTS STATEMENT
This document contains information, which is proprietary to the “EERA-DTOC” Consortium. Neither this document nor the information contained herein shall be used, duplicated or communicated by any means to any third party, in whole or in parts, except with prior written consent of the “EERA-DTOC” consortium.

## Document information

| | |
|---|---|
| **Document Name:** | WP1-Hornsrev benchmark validation. |
| **Document Number:** | 3 |
| **Author:** | Kurt S. Hansen - DTU Wind Energy |
| **Date:** | 5. July 2013 |
| **WP:** | WP1 |
| **Task:** | Task 1 |

# 1 TABLE OF CONTENTS


1 TABLE OF CONTENTS ..... 4

2 INTRODUCTION ..... 5

3 RESULTS: HORNS REV – FLOW SECTOR VARIATION ..... 6
3.1 Objectives ..... 6
Run 1: Wind direction 270° ± 2.5° ..... 6
Run 1: Wind direction 270° ± 7.5° ..... 7
Run 3: Wind direction 270° ± 15° ..... 7

4 BENCHMARK: HORNS REV – ATMOSPHERIC STRATIFICATION ..... 8
4.1 Objectives ..... 8
Run 1: atmospheric stratification =stable. ..... 8
Run 2: atmospheric stratification = neutral. ..... 9
Run 3: atmospheric stratification = unstable. ..... 9

5 BENCHMARK: HORNS REV – TURBULENCE INTENSITY ..... 10
5.1 Objectives ..... 10
Run 1: Flow sector = 250 - 290° and 7D spacing; ..... 10
Run 2: Turbulence intensity 2-14%; flow sector = 90 ± 2.5° and 8±1 m/s and 7D spacing; ..... 11
Run 3: Turbulence intensity 2-14%; flow sector = 132 ± 2.5° and 8±1 m/s and 10.4D spacing; ..... 12

6 BENCHMARK: HORNS REV – SPACING ..... 13
6.1 Objectives ..... 13
Run 1: Spacing 7D, Wind direction 270° ± 5° ..... 13
Run 2: Spacing 9.4 D, Wind direction 221° ± 5° ..... 14
Run 3: Spacing 10.4D, Wind direction 312° ± 5° ..... 14

7 PARK EFFICIENCY ..... 15
7.1 Objectives ..... 15
7.2 Run 1: Wind direction 0°± 2.5°, 5°± 2.5°, 10°± 2.5°, .. ,355°± 2.5° & 360° ± 2.5°. 15

8 REFERENCES ..... 16

ANNEX A: NOTES ON HORNS REV DATA ANALYSIS. ..... 17
8.1 History ..... 17
8.2 Power deficit distribution analysis. ..... 18
8.3 Power deficit along wind turbine row(s) ..... 20
8.4 Standard uncertainty of mean power deficit. ..... 21
8.5 Uncertainty of the inflow direction ..... 23
8.6 Conclusion ..... 24

# 2 INTRODUCTION

The preliminary benchmarking of existing wake models for Horns Rev wind farm has been completed. This document presents the model results for 11 different wake models applied on thirteen different flow cases for the Horns Rev wind farm. Furthermore the analysis of the wind farm measurements has been refined to enable a direct comparison with the wake model results. The refinement includes selection of inflow wind direction reference, exclusion of wind turbine rows and definition of standard uncertainty for the mean power deficit. These are described and discussed in Annex A.
The participating wake models are listed in Table 1.

Table 1: Wake models participating in EERA-DTOC Horns Rev benchmark.

| Model | Affiliation | Contacts |
|---|---|---|
| SCADA(BA) | DTU Wind Energy | pire@dtu.dk |
| NOJ(BA) | DTU Wind Energy | pire@dtu.dk |
| FUGA | DTU Wind Energy | pire@dtu.dk |
| GCL(BA) | DTU Wind Energy | pire@dtu.dk |
| DWM/HAWC2 | DTU Wind Energy | tjul@dtu.dk |
| CRESflowNS | CRES | jprosp@fluid.mech.ntua.gr |
| WAsP/NOJ | Indiana University | rbarthel@indiana.edu |
| RANS | PORTO University | jpalma@fe.up.pt |
| FarmFlow | ECN Wind Energy | schepers@ecn.nl |
| Ainslie | RES-LTD | Tom.Young@res-ltd.com |
| NOJ/Penã | DTU Wind Energy | aldi@dtu.dk |
| GCL(GU) | CENER | jsrodrigo@cener.com |

The model extension (BA) in Table 1 refers to "Bin Averaged" and (GU) refers to "Gaussian Uncertainty" averaged models results. A benchmark activity summary is listed in Table 2. The flow sector sensitivity has been modeled with all wake models, but only 2 - 3 models are able to handle the stratification right now. Furthermore 2 participants have modeled the park efficiency for a 0 – 360 degree inflow sector.
The SCADA results are marked with yellow squares including errorbars; which express the standard uncertainty for the power deficit corresponding to 95% confidence level.

Table 2: Simulation matrix.

| EERA-DTOC | Flow sector | | | Stratification | | | Turbulence | | | Spacing | | | Park efficiency |
|---|---|---|---|---|---|---|---|---|---|---|---|---|---|
| | *1.1* | *1.2* | *1.3* | *2.1* | *2.2* | *2.3* | *3.1* | *3.2* | *3.3* | *4.1* | *4.2* | *4.3* | *5.1* |
| **WASP (NOJ)** | | 1 | 1 | | | | | | | 1 | 1 | 1 | |
| **NOJ(BA)** | 1 | 1 | 1 | | | | 1 | | | 1 | | | |
| **FarmFlow** | 1 | 1 | 1 | | | | 1 | 1 | 1 | 1 | 1 | 1 | |
| **FUGA** | 1 | 1 | 1 | | | | 1 | | | 1 | | | |
| **GCL(BA)** | 1 | 1 | 1 | | | | 1 | 1 | 1 | 1 | | | |
| **DWM/HAWC2** | 1 | 1 | 1 | 1 | 1 | 1 | 1 | 1 | 1 | 1 | 1 | 1 | |
| **CRESflowNS** | 1 | 1 | 1 | 1 | 1 | 1 | 1 | 1 | | 1 | | 1 | 1[a] |
| **Ainslie** | 1 | 1 | 1 | | | | 1 | 1 | 1 | | | | |
| **RANS** | 1 | 1 | 1 | | | | 1 | | | 1 | 1 | 1 | |
| **NOJ/Penã** | 1 | 1 | 1 | 1 | 1 | 1 | 1 | 1 | 1 | 1 | 1 | 1 | 1 |
| **GCL(GU)** | 1 | 1 | 1 | | | | 1 | 1 | 1 | 1 | 1 | 1 | 1 |
| **sum** | 10 | 11 | 11 | 3 | 3 | 3 | 10 | 7 | 6 | 10 | 6 | 7 | 3 |

1[a] Amended GCL calibrated with CRESflowNS

# 3 RESULTS: HORNS REV – FLOW SECTOR VARIATION

**Test Case ID**: HornsRev_270Neutral
**Managed by**: Kurt S. Hansen (DTU)

## 3.1 Objectives

Determine the power deficit along a single row of 10 turbines, with an internal spacing of 7D, inside a wind farm of regular layout. Evaluate the sensitivity of the model performance to the wind direction sector size.

The conditions for simulating the wind farm flow are:

- Wind farm layout and coordinates of the wind turbine positions (1);
- V80-2MW turbine specifications (1);
- Roughness length: $z_0$ = 0.0001 m;
- Inflow mean velocity at hub height (70 m): 8 m/s;
- Inflow turbulence intensity at hub height: 7%;

**Run 1: Wind direction 270° ± 2.5°**

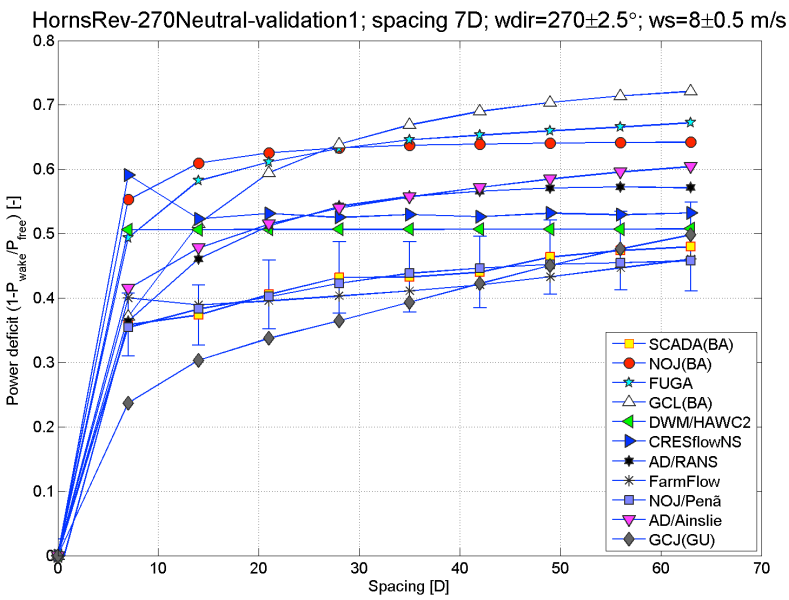


Figure 1: Power deficit along a single row of turbines (row7) as function of spacing for a 5° flow sector at 8 m/s.

The error bars attached to the SCADA results express the two times standard uncertainty of the power deficit corresponding to a 95% confidence level.

### Run 1: Wind direction 270° ± 7.5°

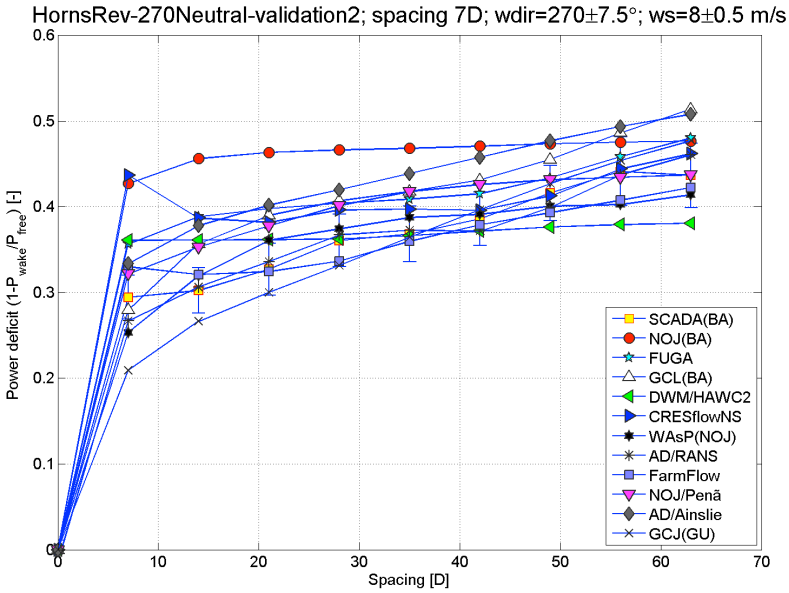


Figure 2: Power deficit along a single row of turbines (row7) as function of spacing for a 15° flow sector at 8 m/s.

### Run 3: Wind direction 270° ± 15°

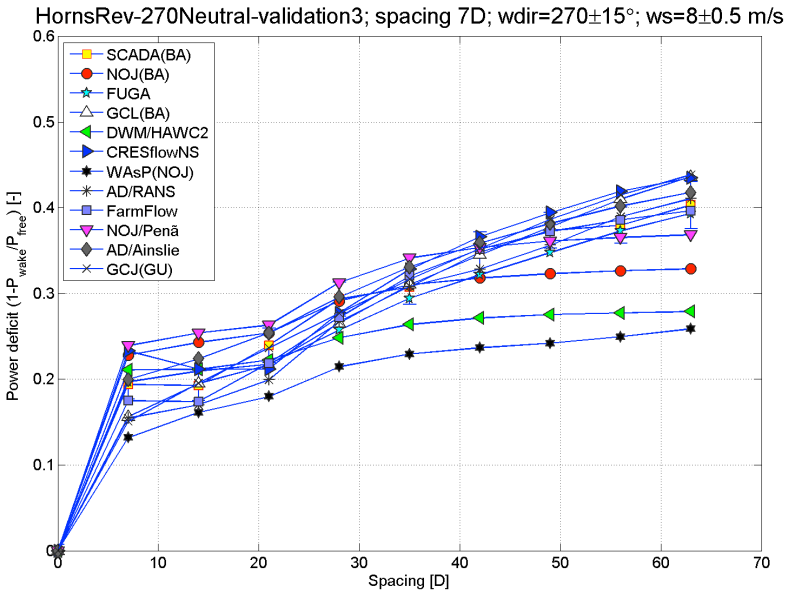


Figure 3: Power deficit along a single row of turbines (row7) as function of spacing for a 30° flow sector at 8 m/s.

# 4 BENCHMARK: HORNS REV – ATMOSPHERIC STRATIFICATION

**Test Case ID**: HornsRev_270Stratification

**Managed by**: Kurt S. Hansen (DTU)

## 4.1 Objectives

Determine the power deficit along a single row of 10 turbines, with an internal spacing of 7D, inside a wind farm of regular layout. Evaluate the sensitivity of the model performance for three atmospheric stratifications, categorized as stable, neutral or unstable.

The conditions for simulating the wind farm flow are:

- Wind farm layout and coordinates of the wind turbine positions (1);
- V80-2MW turbine specifications (1);
- Roughness length: $z_0$ = 0.0001 m;
- Inflow mean velocity at hub height (70 m): 8 m/s;
- Inflow wind direction sector 270 ± 5°;
- Inflow turbulence intensity at hub height: 7%;

Three principal cases have been defined to validate the influence of the atmospheric stability (2).

**Run 1: atmospheric stratification =stable.**

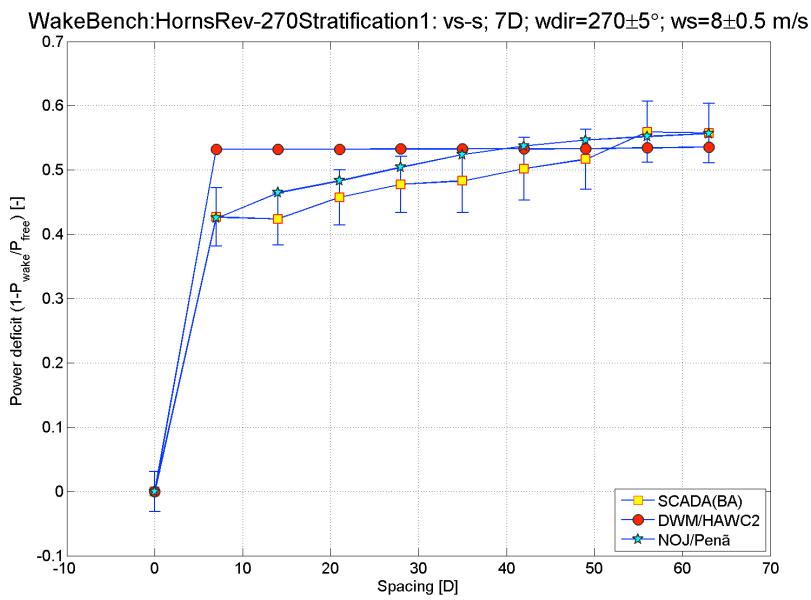


Figure 4: Power deficit along a single row of turbines (row7) as function of spacing for a 10° inflow sector at 8 m/s and stable stratification.

The standard uncertainty *u* of the power deficit is 0.02 and the errorbars represent a 95% confidence level for the SCADA results equal of 2 x *u*.

The classification of the stratification is based on mast measurements: U(20m, mast M7), Tabs(16m, mast M7) and Twater(-4m, mast M7) and calculated with AMOK; which is an in-house software package.

**Run 2: atmospheric stratification = neutral.**

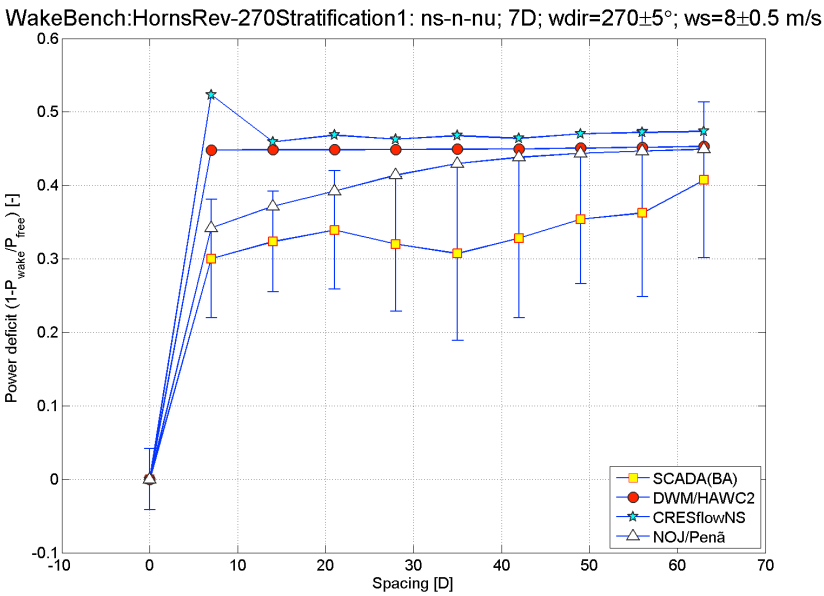


Figure 5: Power deficit along a single row of turbines (r7) as function of spacing for a 10° inflow sector at 8 m/s and neutral stratification.

The standard uncertainty *u* of the power deficit is within the range 0.02- 0.06. The standard uncertainty for the SCADA results is high mainly due to the low number of available observations (2 – 3 hours).

**Run 3: atmospheric stratification = unstable.**

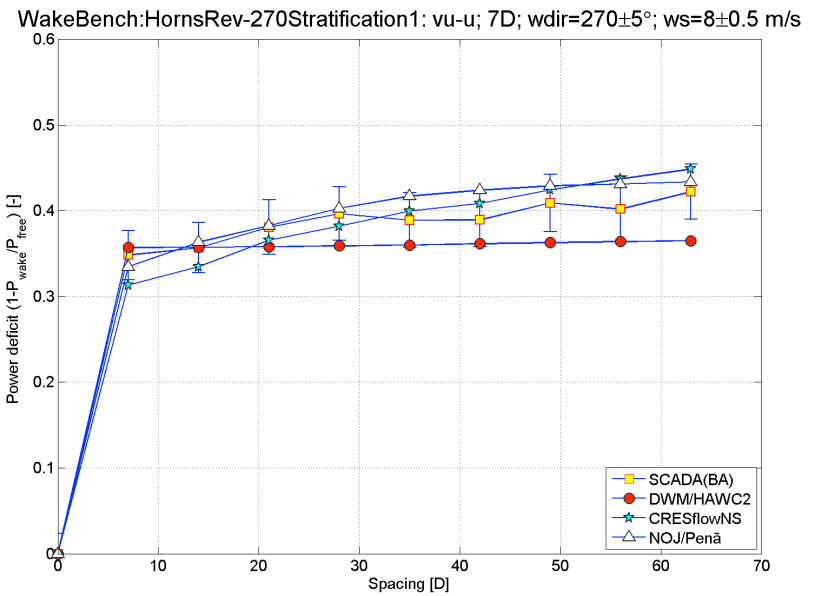


Figure 6: Power deficit along a single row of turbines (row7) as function of spacing for a 10° inflow sector at 8 m/s and unstable stratification.

The standard uncertainty of the power deficit *u* is within the range 0.01-0.02.

# 5 BENCHMARK: HORNS REV – TURBULENCE INTENSITY

**Test Case ID**: HornsRev_270turbulence
**Managed by**: Kurt S. Hansen (DTU)

## 5.1 Objectives

Evaluate park models on a wind farm with well defined boundary conditions to determine the power deficit. The power deficit is determined between two nearby turbines with 7D spacing. The power deficit is determined for 8 m/s hub height wind speed as function of turbulence intensity.

The conditions for simulating the wind farm flow are:

- Wind farm layout and coordinates of the wind turbine positions (1);
- V80-2MW turbine specifications (1);
- Roughness length: $z_0$ = 0.0001 m;
- Inflow mean velocity at hub height (70 m): 8 m/s;

**Run 1: Flow sector = 250 - 290° and 7D spacing;**

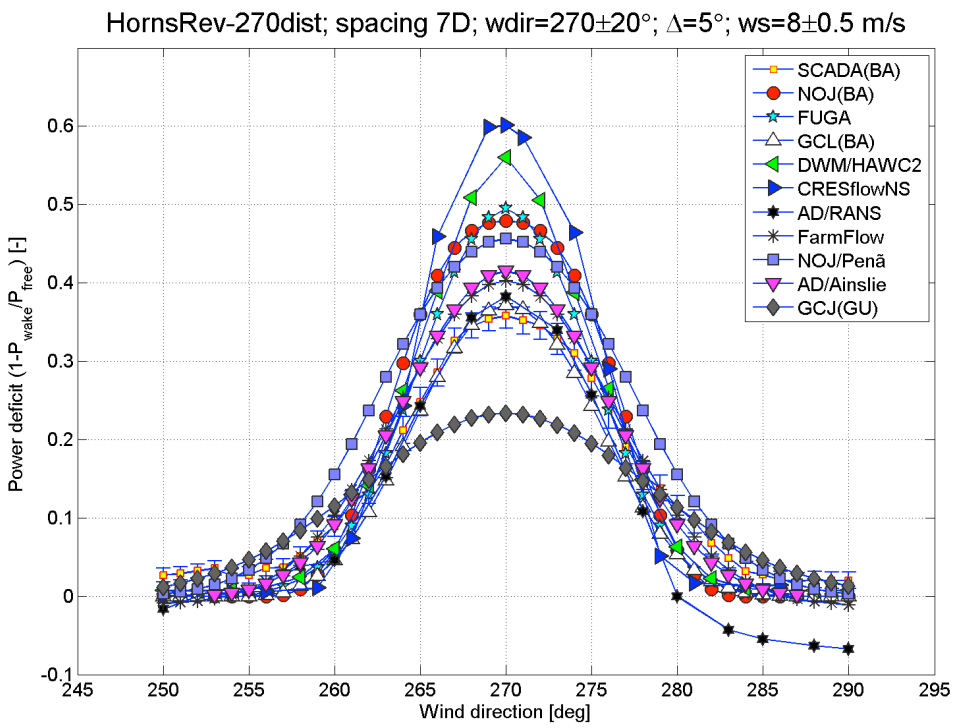


Figure 7: Power deficit distribution between 1 pair of turbines, using a 5° moving average window.

The standard uncertainty *u* of the power deficit is very low, equal to 0.01 and the errorbars express two times the standard uncertainty, equivalent of a 95% confidence level. The peak power deficit is defined as the maximum values on Figure 7 for a 5° inflow sector.

**Run 2: Turbulence intensity 2-14%; flow sector = 90 ± 2.5° and 8±1 m/s and 7D spacing;**

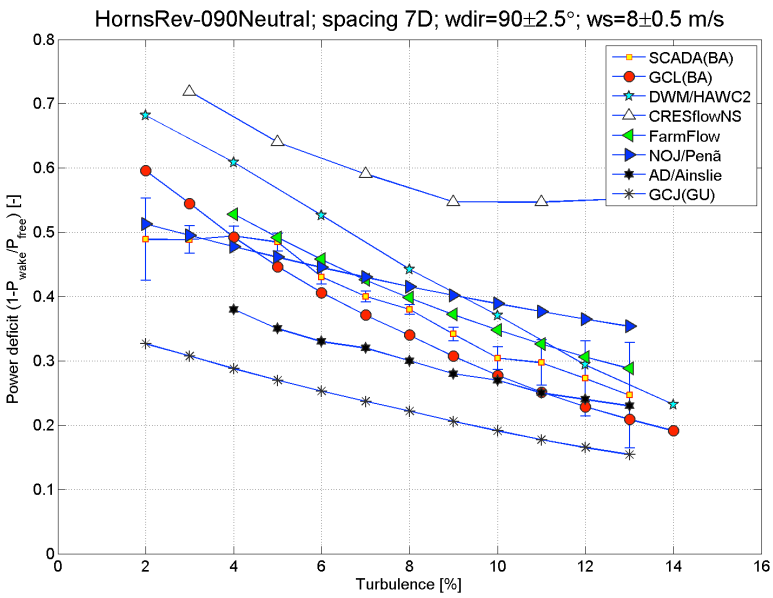


Figure 8: Peak power deficit for 7D spacing as function of turbulence intensity for a 5° inflow sector.

The SCADA results represent a wind speed range of 6 – 12 m/s and are recorded for an easterly sector with reference to the turbulence, measured on mast M6. Each SCADA observation in Figure 8 represent more than 1 hour of measurements. The standard uncertainty is low, except for low and high turbulence mainly due to a lack of data. The errorbars at Figure 8 express two times the standard uncertainty corresponding to a 95% confidence level.

**Run 3: Turbulence intensity 2-14%; flow sector = 132 ± 2.5° and 8±1 m/s and 10.4D spacing;**

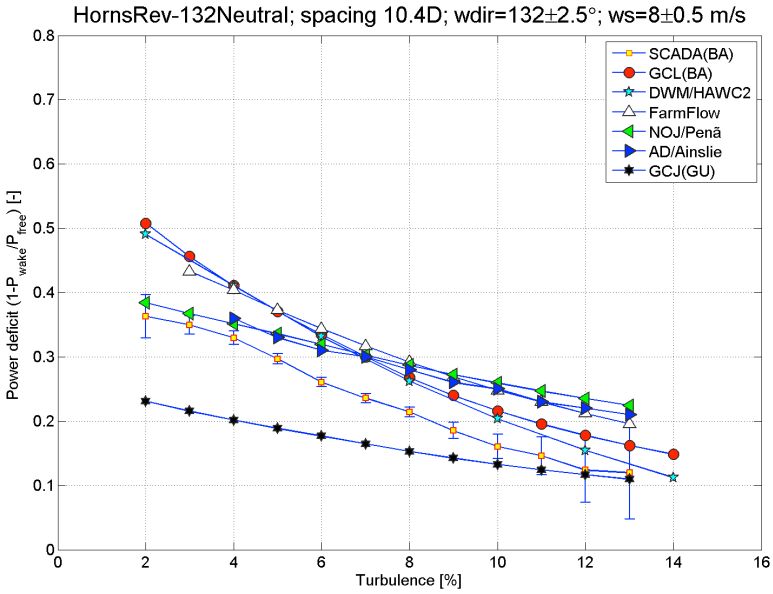


Figure 9: Peak power deficit for 7D spacing as function of turbulence intensity for a 5° inflow sector.

The SCADA results represent a wind speed range of 6 – 12 m/s and are recorded for an south easterly sector with reference to the turbulence, measured on mast M6. Each SCADA observation in Figure 8 represent more than 1 hour of measurements. The standard uncertainty is low, except for low and high turbulence mainly due to a lack of data. The errorbars at Figure 9 express two times the standard uncertainty corresponding to a 95% confidence level.

# 6 BENCHMARK: HORNS REV – SPACING

**Test Case ID**: HornsRev_270Spacing
**Managed by**: Kurt S. Hansen (DTU)

## 6.1 Objectives

Determine the power deficit along a single rows consisting of 6 or 10 turbines, with a varying internal spacing, inside a wind farm of regular layout. The purpose is to evaluate the sensitivity of the wake model performance to the wind turbine spacing.

The conditions for simulating the wind farm flow are:

- Wind farm layout and coordinates of the wind turbine positions (1);
- V80-2MW turbine specifications (1);
- Roughness length: $z_0$ = 0.0001 m;
- Inflow mean velocity at hub height (70 m): 8 m/s;
- Inflow turbulence intensity at hub height: 7%;

Three principal cases have been defined to validate the influence of the spacing (2).

### Run 1: Spacing 7D, Wind direction 270° ± 5°

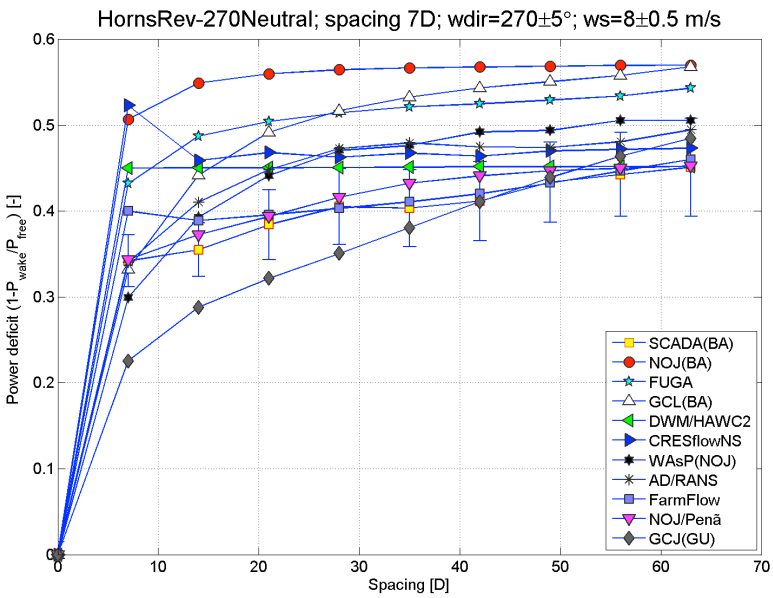


Figure 10: Power deficit along a single row of turbines (row7) as function of 7D spacing for a 10° flow sector at 8 m/s.

### Run 2: Spacing 9.4 D, Wind direction 221° ± 5°

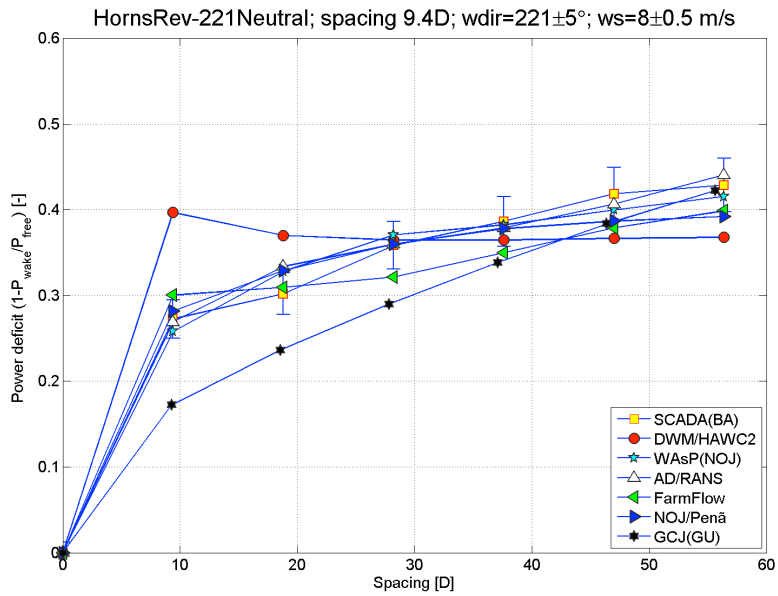


Figure 11: Power deficit along a single row of turbines - as function of 9.4D spacing for a 10° flow sector at 8 m/s.

### Run 3: Spacing 10.4D, Wind direction 312° ± 5°

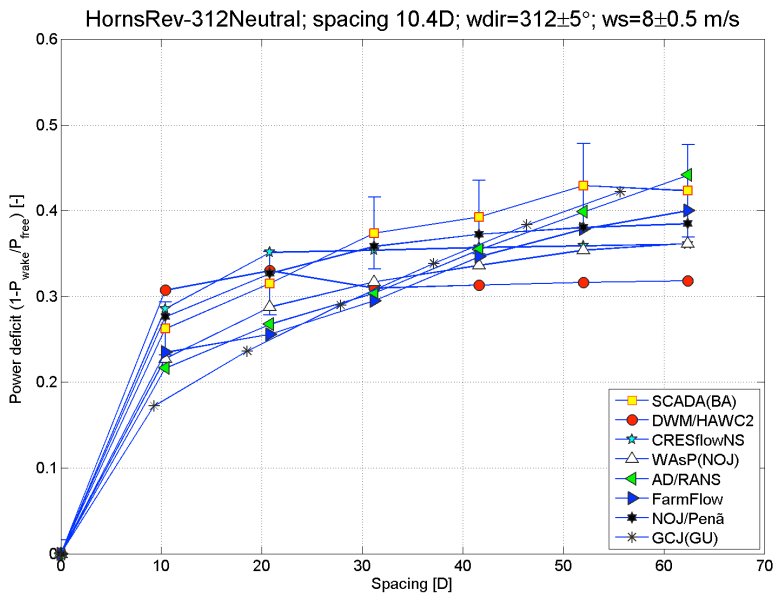


Figure 12: Power deficit along a single row of turbines - as function of 9.4D spacing for a 10° flow sector at 8 m/s.

# 7 PARK EFFICIENCY

**Test Case ID**: HornsRev_270Spacing
**Managed by**: Kurt S. Hansen (DTU)

## 7.1 Objectives

Determine the park power efficiency for 0 - 360° inflow, where the efficiency is defined as the ratio between the park power and the power from 80 x one stand-alone wind turbine.

The conditions for simulating the wind farm flow are:

- Wind farm layout and coordinates of the wind turbine positions (1);
- V80-2MW turbine specifications (1);
- Roughness length: $z_0$ = 0.0001 m;
- Inflow mean velocity at hub height (70 m): 8 m/s;
- Inflow turbulence intensity at hub height: 7%;

One principal case has been defined to validate the park efficiency.

## 7.2 Run 1: Wind direction 0°± 2.5°, 5°± 2.5°, 10°± 2.5°, .. ,355°± 2.5° & 360° ± 2.5°.

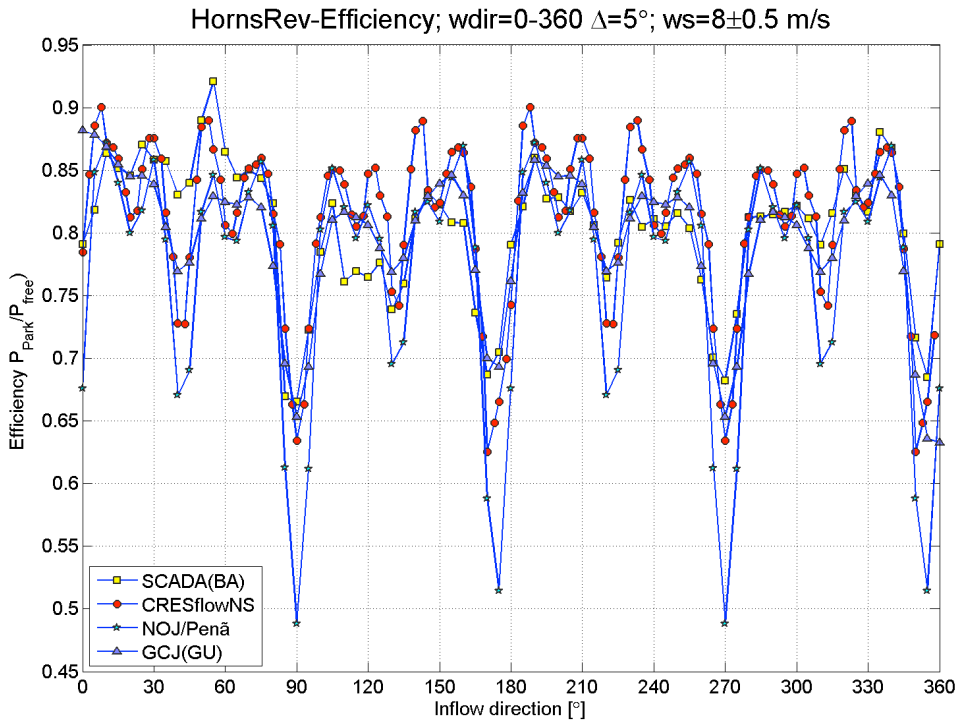


Figure 13: Park power efficiency at 8 m/s inflow - as function of inflow direction.

The park efficiency plot in Figure 13 illustrates the four distinct narrow deficit sectors along the main directions inside the Horns Rev wind farm. The deficits sectors are well captured with both models.

# 8 REFERENCES

(1) Presentation of the Horns Rev offshore wind farm and the Vestas V80 wind turbine. DTOC name: Hornsrev-V80, 28th June 2012; Kurt S. Hansen – DTU Wind Energy.

(2) WP1.1 Wake model performance validation, Horns Rev offshore wind farm. DTOC Name: WP1-Horns Rev test case, 29th June 2012; Kurt S. Hansen DTU Wind Energy.

(3) Hansen, et. al.; *The impact of turbulence intensity and atmospheric stability on power deficits due to wind turbine wakes at Horns Rev*; Wind Energy 2012, we.512 Wiley.

# ANNEX A: NOTES ON HORNS REV DATA ANALYSIS.

Preliminary analysis of the Horns Rev wind farm has been based on 1½ -2 years of recordings without a representative distribution of the stratification. The previous findings have been published a.o. in (3). Figure 8a (3) demonstrated a peak power deficit distribution of 0.42 for a pair of turbines with 7D spacing. This peak number has been difficult to reproduce after the dataset has been enlarged in combination with an improved filtering; furthermore the findings are based on wind speed from mast M2; which showed some failures. Due to recent discussion on the data validity, this note should clarify some of the recent doubts concerning wind farm power deficit including a sensitivity analysis for the reference signals.
This note will address the uncertainty estimation of using derived inflow parameters when performing wind farm flow analysis on Horns rev wind farm and the standard uncertainty for mean deficit values is defined. The peak deficit refers to the maximum power deficit for a 5 degree inflow sector in the following plots and discussion.

## 8.1 History

The preliminary dataset includes measurements from 80 turbines, representing the period 2005 - January 2007. The corresponding mast measurements are represented with:

a) Mast M6 & M7; 2005 - 2009, demonstrated both high quality and availability.

Unfortunately it was not possible to obtain direct inflow measurements, e.g. wind speed and direction for the frequent western inflow sector. Instead power values have been combined with the reference to the power curve to determine the wind speed. The turbine yaw position is calibrated and used to determine the local inflow direction. WT07 on Figure 14 has been used as a reference wind turbine for the westerly flow sector.

- The wind speed is determined within ±0.2 m/s, with reference to the power curve (3);
- The wind direction is determined with a rather high uncertainty, mainly caused by the yaw control hysteresis. Furthermore the yaw position offset has to be determined by analyzing the power deficit distribution for a pair of turbines.

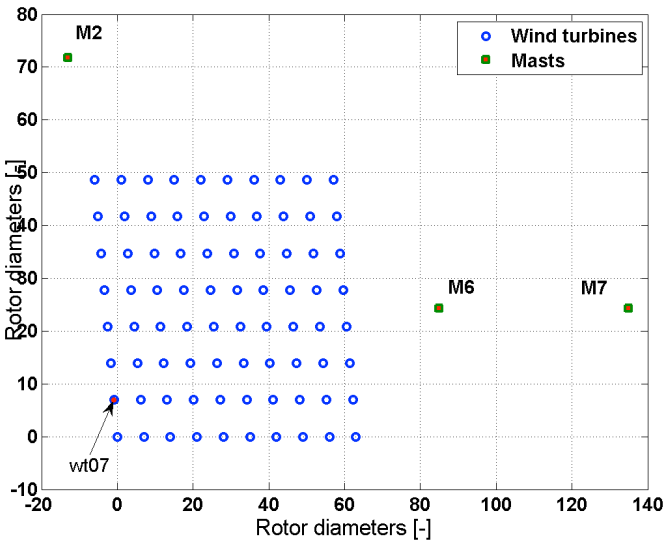


Figure 14: HR Layout

## 8.2 Power deficit distribution analysis.

The basic power deficit distribution is shown in Figure 15 and represents a narrow distribution with a peak deficit (Δ=5°) of 0.42 and a 95% confidence distribution width of 30°.

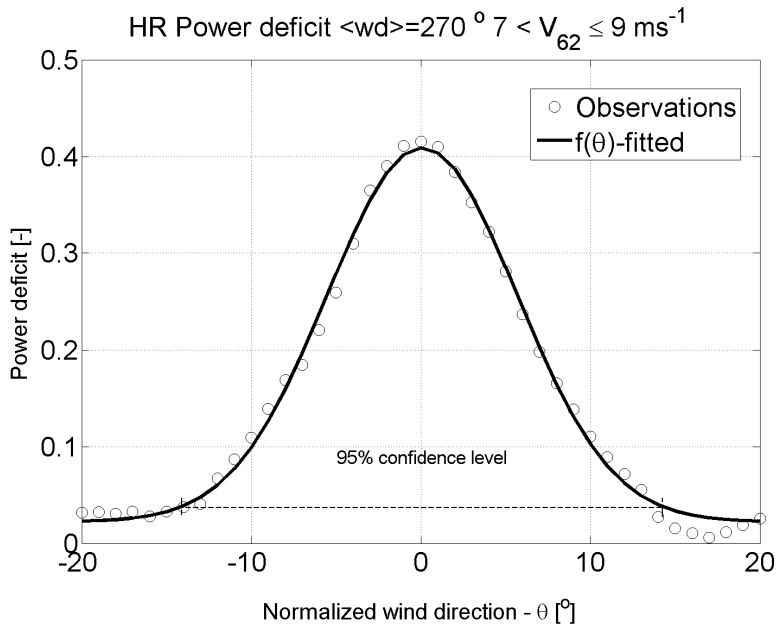


Figure 15: Deficit distribution with a peak deficit of 0.42 from (3).

The present analysis has been based on combinations of periods, wind direction signals and atmospheric stratification; which are summarized in Table 3.

Table 3: Power deficit sensitivity analysis - based on 1 pair of wind turbines.

| # | Wind speed | Ínflow Sector | Period | Wind dir reference | Stratification | Peak deficit | Comments |
|---|---|---|---|---|---|---|---|
| 1. | 8 ±1 m/s | 270° | ? | M2, h=60m | all | 0.42 | Reference Figure 8a from (3). |
| 2. | 8 ±1 m/s | 270° | 2005-2006 | NP07[1] | all | 0.36 | Shape is ok, but the peak does not increase when including pair wt16/wt06. |
| 3. | 8 ±1 m/s | 270° | 2005-2007 | M7[2] wd;68m | all | 0.31 | Broader deficit shape compared to Figure 1. |
| 4. | 8 ±1 m/s | 270° | 2005-2009 | M7[2] wd;68m | all | 0.32 | See previous comment #4 |
| 5. | 8 ±1 m/s | 90° | 2005-? | M6: wd68 m | all | 0.38 | Shape ok, but with a limited number of observations |
| 6. | 8 ±1 m/s | 90° | 2005-2009 | NP95 | all | 0.36 | Shape ok, but with a limited number of observations |
| 7. | 8 ±1 m/s | 270° | 2005-2009 | NP07 | s - vs[3] Stable | 0.43 | Shape is ok |

[1] The offset for wt07 yaw position, named NP07 is constant during 2005-2006.

[2] The offset for wind direction signal M7, h=68 m is calibrated for 8 principal wind farm inflow sectors where each wind sector is represented with 4-6 pairs of turbines.

[3] The stratification is determined according to the Monin-Obukhov theory with the AMOK tool, based on the air-water temperature difference and the wind speed measured 20m above msl.

| | | | | | | | |
|---|---|---|---|---|---|---|---|
| 10. | 8 ±1 m/s | 270° | 2005-2009 | NP07 | nu-n-ns³ Neutral | 0.38 | Shape is ok |
| 11. | 8 ±1 m/s | 270° | 2005-2009 | NP07 | vu-u³ Unstable | 0.34 | Shape is ok |

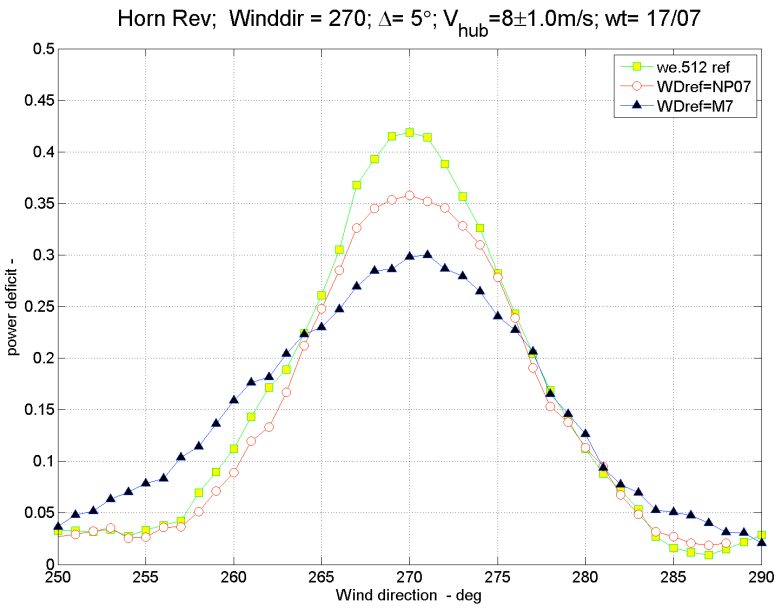


Figure 16: Power deficit distribution for wt17/wt07 recorded Turing 2005-2009 with reference to 2 different inflow reference wind direction signals.

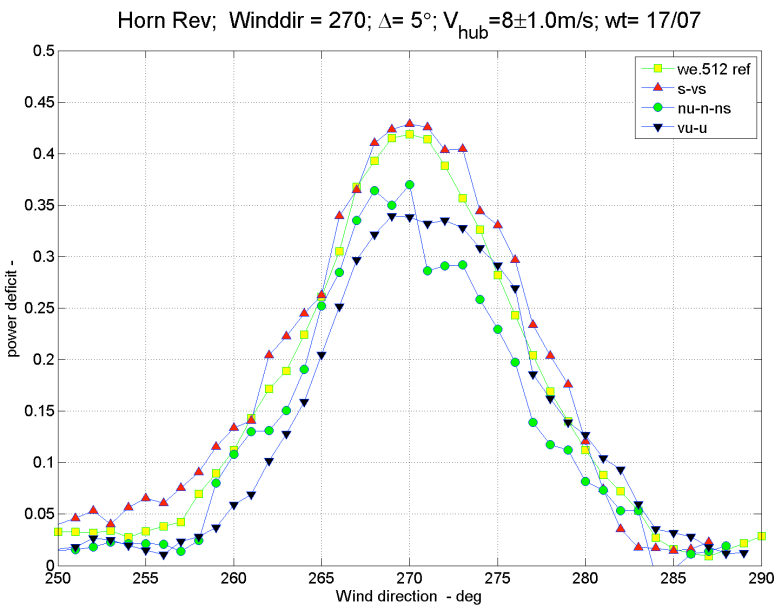


Figure 17: Power deficit distribution for stable, neutral and instable stratification.

**Discussion:**

1) The selection of a nearby inflow direction reference (NP07 yaw position) is important compared to the calibrated wind vane on M7 located more than 10 km downstream to the wind farm. Using the M7 reference results in a decreased peak deficit and an increased distribution width, as shown in Figure 16. The short time correlation (< 1 hour)

between reference wind direction based on M7 and the power deficit is reduced, compared to a reference signal based on wind turbine yaw position.

2) The peak deficit highly correlates with the atmospheric stratification, as demonstrated on the Figure 17. The peak deficit varies from 0.34 – 0.43 by grouping the stratification in three main groups: unstable, neutral and stable.

3) The peak deficit is determined for the recording periods, especially it is important to include period with a fair representation of the stratification.

4) The published distribution; Figure 8a (3) has been based on periods with stable stratification.

## 8.3 Power deficit along wind turbine row(s)

The peak deficit along single wind turbine rows are determined with reference to the inflow conditions for the undisturbed wind turbine analog to the previous definition. The power deficit for a narrow westerly flow sector; 270±2.5° is used as basic flow case and the deficit is shown in Figure 18.

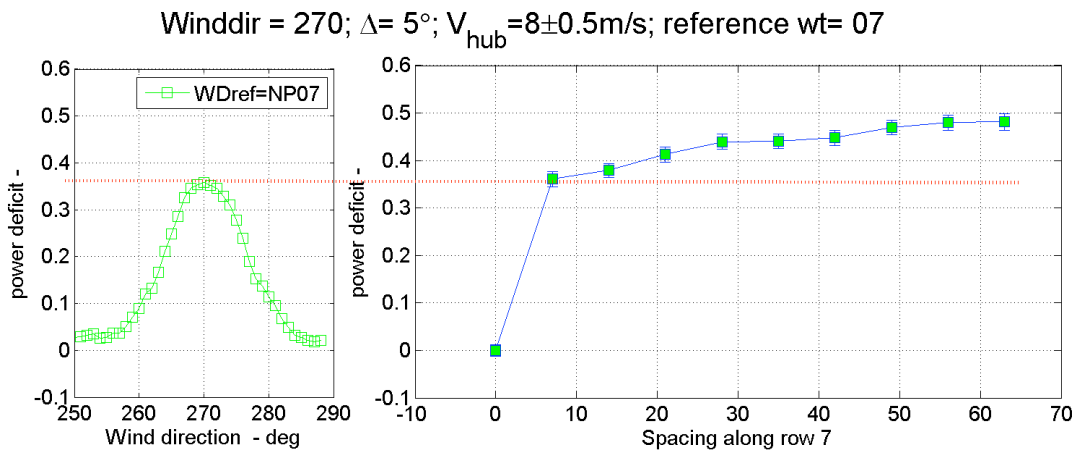


Figure 18: Power deficit distribution and peak power deficit for Δ=5° along row 7.

Figure 18 demonstrates how the deficit distribution between a pair of turbines agrees well with the peak deficit along a row of turbines.

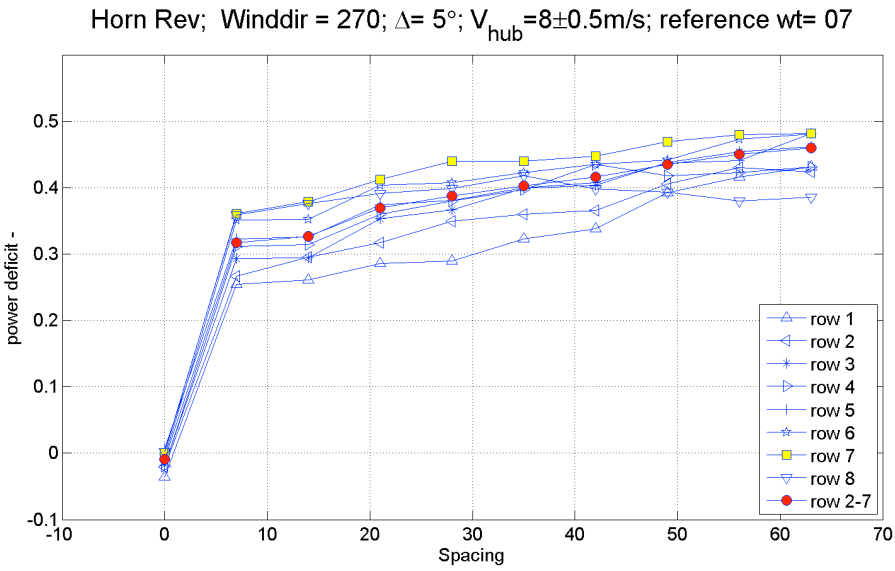


Figure 19: Peak power deficit along 8 rows including the reference row 7 and averaged values for row 2-7.

The average power deficit along multiple parallel rows of wind turbines demonstrates some scatter due to the lateral inflow variation (wind speed and wind direction) as demonstrated in Figure 19. The scatter in the inflow turbine column is within ±2%, but increases downstream inside the wind farm. The scatter is primarily caused by individual wind turbine yaw misalignment combined with lateral flow gradient. The figure furthermore demonstrates the averaged inflow conditions based on row 2-7 results in a reduced peak deficit compared to deficit along a single row turbines, e.g. row7.

## 8.4 Standard uncertainty of mean power deficit.

The power deficit (μ) values have been extracted from the data analysis representing 6 different spacing distances. The distribution of power deficit values for 7D spacing is shown Figure 20 a) for a narrow flow sector (Δ=5°). The figure furthermore includes the normal distribution (red curve) based on the mean deficit value and standard deviation for the population of 68 observations. The power deficit values cover the range 0 – 0.65 and are assumed to be Gaussian distributed around the mean value. Figure 20 includes power deficit distributions for 6 different spacing ranging from 7D – 63D. The corresponding curves for an inflow sector of 30 degrees are shown in Figure 21. Each of these distributions represents more than 500 observations and also seems to be Gaussian distributed.

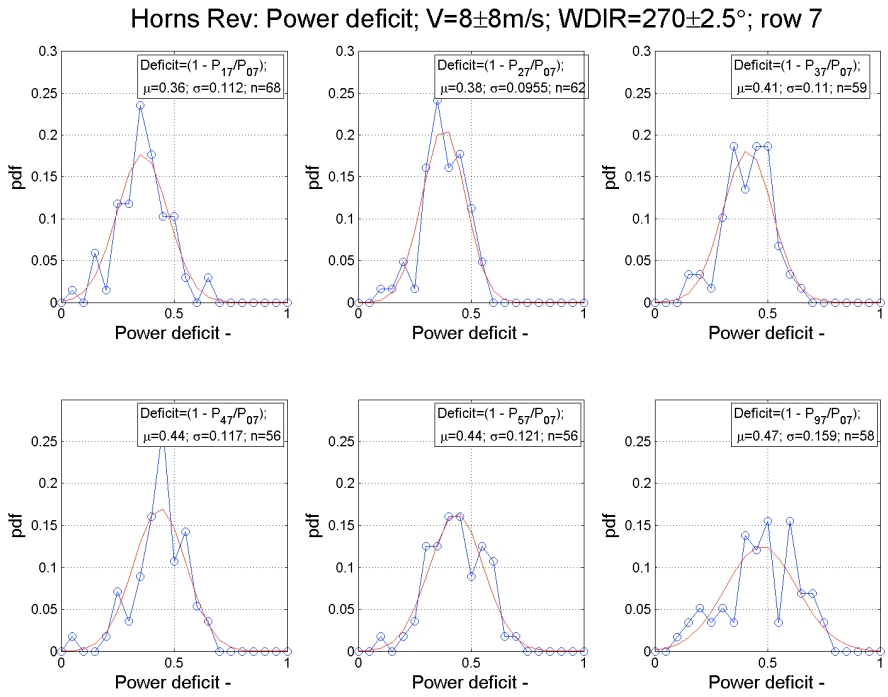


Figure 20: Distribution of power deficit for 7, 14, 21, 28, 35 & 63D spacing respectively, representing a narrow 5° inflow sector.

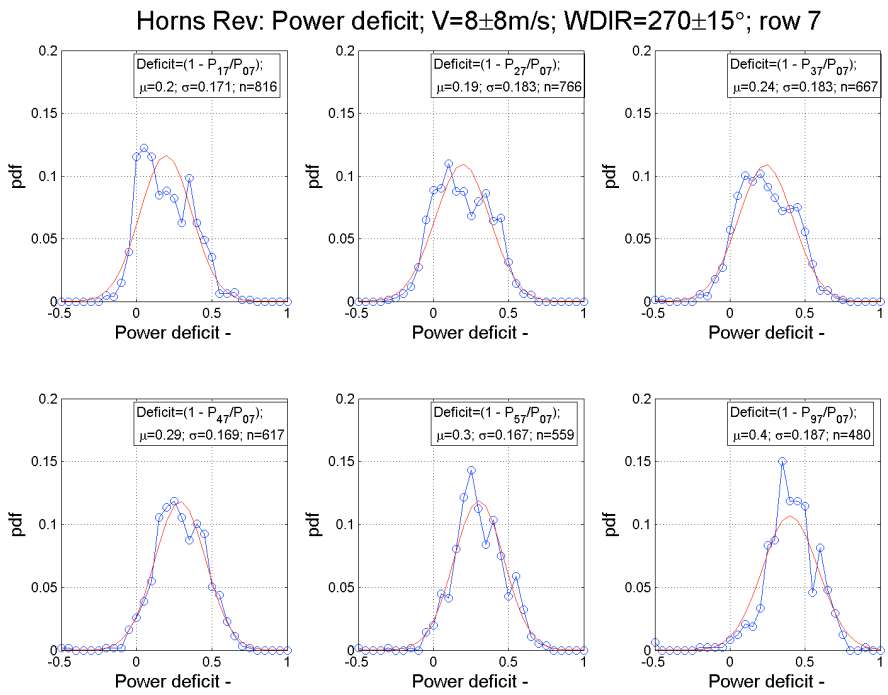


Figure 21: Distribution of power deficit for 7, 14, 21, 28, 35 & 63D spacing respectively, representing a 30° inflow sector.

The standard uncertainty *u* is defined according to $u=s/\sqrt{n}$, where *u* express the standard uncertainty of the mean power deficit with a confidence level of 68% and 2x*u* express the

standard uncertainty of the mean power deficit with a confidence level of 95%. The standard uncertainty, *u* is equal to 0.015 for all peak deficit values; which is almost invisible in Figure 18. Example of mean power deficit, standard deviation and standard uncertainty for row 7 are shown in Figure 22. The results represent 53 – 70 observations for wind turbine located in row 7; this corresponds to approximately 10 hours of operation for each wind turbine recorded over a period of 5 years.

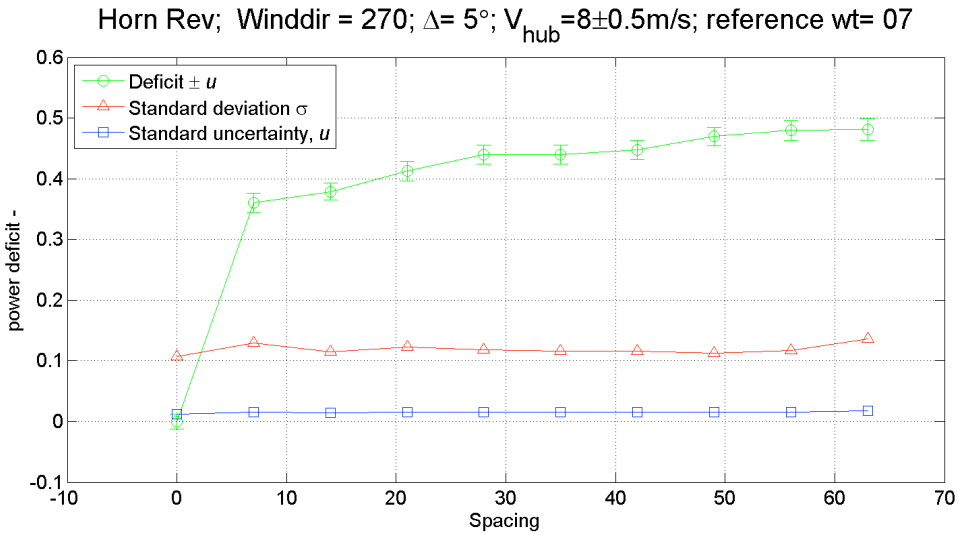


Figure 22: Power deficit, standard deviation and standard uncertainty along a row of wind turbines with 7D spacing.

## 8.5 Uncertainty of the inflow direction

Due to lack of measurements from mast M2 the yaw position of wind turbine WT07 has been used as a reference. Wind turbine wt07 is located in the western row of turbines, Figure 13. Approximately one year of wind direction measurements from M2 have been used to estimate the uncertainty of wind turbine yaw position.
The following reference signals have been used for the investigation:

- $wd60_{M2}$, wind direction, stored as 10-minute average and standard deviation values, which have been recorded at level 60 m on mast M2; σ= standard deviation of $wd60_{M2}$. ;
- np07, yaw position of wind turbine WT07;
- npxx, yaw position of each of the 80 wind turbines in the wind farm.

The difference between inflow $wd60_{M2}$ and yaw position is defined as $\Delta = np07 - wd60_{M2}$ where $\sigma_\Delta$= standard deviation of Δ. The verification has been performed for an undisturbed westerly inflow sector: 235-315° and U=5.5 – 10.5 m/s.

$\sigma_{wd60} = \bar{\sigma}_i$ where *i* includes all 10 minute stdev recordings from mast M2.

$\sigma_{NP} = \sqrt{\sigma_\Delta^2 - \sigma_{wd60}^2}$ stdev for the wind turbine inflow (including a distance factor with reference to the mast M2).

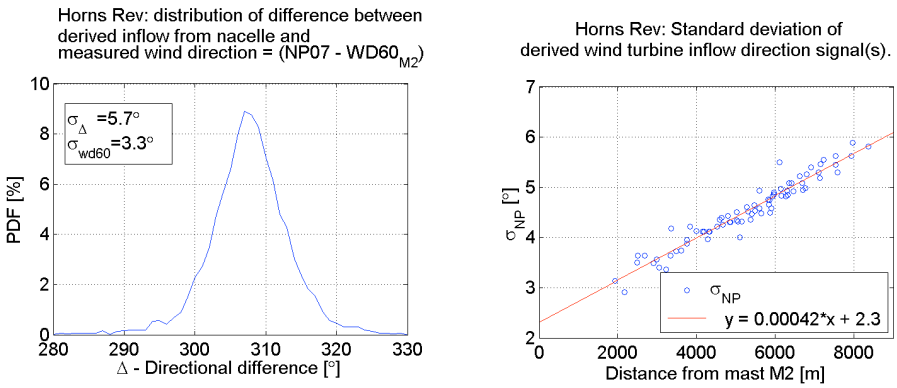


Figure 23: a) distribution of inflow difference Δ based on wt07 yaw position minus wd60. b) stdev of inflow difference $\sigma_{NP}$ as function of distance to reference mast M2 – for all turbines.

The expected standard deviation for the inflow direction is approximately 2.3°- based on a wind turbine yaw position according to Figure 22 b); this number is lower than the standard deviation measured directly with the wind vane, mainly due to the hysteresis applied through the yaw control system (which serves as a low pass filter).

## 8.6 Conclusion

The level of the power deficit highly depends on the 1) reference inflow conditions, 2) the stratification and 3) the data period.

Wind Energy

WIND ENERGY
*Wind Energ.* (2013)
Published online in Wiley Online Library (wileyonlinelibrary.com). DOI: 10.1002/we.1625

RESEARCH ARTICLE

# Evaluation of the wind direction uncertainty and its impact on wake modeling at the Horns Rev offshore wind farm

M. Gaumond[1], P.-E. Réthoré[1], S. Ott[1], A. Peña[1], A. Bechmann[1] and K. S. Hansen[2]

[1] DTU Wind Energy, Risø Campus, Roskilde, Denmark
[2] Department of Mechanical Engineering, Technical University of Denmark, Kgs Lyngby, Denmark

## ABSTRACT

Accurately quantifying wind turbine wakes is a key aspect of wind farm economics in large wind farms. This paper introduces a new simulation post-processing method to address the wind direction uncertainty present in the measurements of the Horns Rev offshore wind farm. This new technique replaces the traditional simulations performed with the 10 min average wind direction by a weighted average of several simulations covering a wide span of directions. The weights are based on a normal distribution to account for the uncertainty from the yaw misalignment of the reference turbine, the spatial variability of the wind direction inside the wind farm and the variability of the wind direction within the averaging period. The results show that the technique corrects the predictions of the models when the simulations and data are averaged over narrow wind direction sectors. In addition, the agreement of the shape of the power deficit in a single wake situation is improved. The robustness of the method is verified using the Jensen model, the Larsen model and Fuga, which are three different engineering wake models. The results indicate that the discrepancies between the traditional numerical simulations and power production data for narrow wind direction sectors are not caused by an inherent inaccuracy of the current wake models, but rather by the large wind direction uncertainty included in the dataset. The technique can potentially improve wind farm control algorithms and layout optimization because both applications require accurate wake predictions for narrow wind direction sectors. Copyright © 2013 John Wiley & Sons, Ltd.

**KEYWORDS**

wind farm; offshore; wake; power deficit; wind direction

**Correspondence**

Mathieu Gaumond, DTU Wind Energy, Risø Campus, Roskilde, Denmark.
E-mail: mathieu.gaumond@gmail.com

Received 9 November 2012; Revised 28 February 2013; Accepted 22 March 2013

## 1. INTRODUCTION

The rising demand for wind power together with social, environmental and economical constraints currently lead to an increase in the size of wind turbines and wind farms. A drawback from installing wind turbines in large arrays is the wake penalty that arises when a wind turbine operates in the lee of another. In large offshore wind farms, the average energy loss due to wind turbine wakes is approximately 10% to 20% of the annual energy production.[1] As the wind flows through the rotors, turbulent structures are generated and transported downstream. The resulting turbulent velocity field reduces the wind turbine lifespan and increases maintenance costs. Therefore, it is crucial for wind farm developers to estimate accurately the impact of wind turbine wakes because it has become significant for wind farm economics.

Most engineering wake models currently used by the wind industry are still based on the classical work from Jensen,[2] Katic *et al.*[3] and Ainslie[4] in the 1980s, although the challenges of wake modeling have drastically changed since then. Today, wind farms are increasingly being installed in sites where the assumptions underlying these models are not valid. The characteristics of such sites include complex orography, forests and non-neutral atmospheric stability. The size of wind farms has also become an increasing issue because the engineering models tend to underestimate wake losses in large wind farms.[1,5,6] Some studies suggest that these deviations occur because wind power plants are now so large that they have an impact on the local boundary layer.[7,8]

Copyright © 2013 John Wiley & Sons, Ltd.

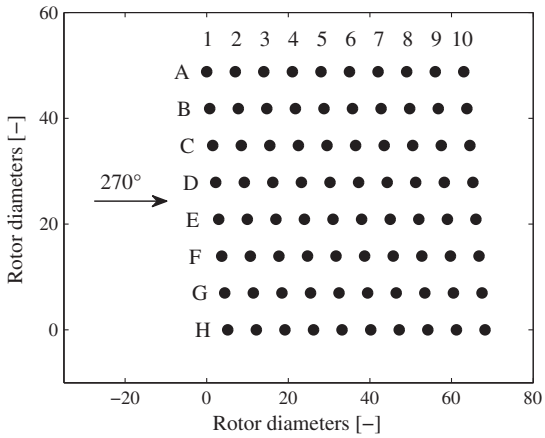


**Figure 1.** Layout of the Horns Rev offshore wind farm.

With the increase in computer power, several new wake models have been developed in an attempt to overcome these issues.[9] Some promising approaches include computational fluid dynamics methods using Reynolds-averaged Navier–Stokes (RANS) models[10,11] or large eddy simulations.[12–15] Nevertheless, several studies found that conventional RANS simulations overpredict the velocity inside the wakes due to the limitations of the Boussinesq hypothesis.[16–19]

The wide variety of available wake models emphasizes the need for additional validation campaigns to define clear guidelines on how the wind industry shall use the models.[20] A better understanding of the wake models' limitations will decrease wake loss uncertainty in project development and improve the competitiveness of wind energy. However, comparing numerical simulations with wind farm production data is a task that must be carried out carefully in a context where robust solutions are desired. Barthelmie *et al.*[1] underlined several aspects to consider when performing benchmarking studies with experimental data. One issue is the wind direction uncertainty included in the datasets because numerical simulations are very sensitive to a change of wind direction input.[21] In some cases, the reference wind direction of a whole wind farm is determined from the yaw position sensor of an upstream wind turbine during data processing. Hansen *et al.*[22] mentioned that this method 'results in an uncertainty of more than 7° because the yaw misalignment of the reference turbine also needs to be included'. In addition, spatial variability and time averaging of the wind direction increase the direction uncertainty in large wind farms due to the stochastic behavior of the wind. Gaumond *et al.*[23] suggested that the discrepancies of numerical simulations for narrow wind direction sectors ($< 10°$) found in previous studies[10,12,24] are not caused by wake modeling inaccuracies, but rather by the large wind direction uncertainty included in the datasets. Further, Gaumond *et al.*[23] highlighted a correlation between the width of the wind direction sector used for data binning and the agreement of the numerical simulations with wind farm data. It has become critical to quantify this uncertainty to enable a better and fairer comparison between numerical simulations and power production data. Ultimately, the robustness of the models should improve by excluding the site-specific dataset uncertainty from the model calibrations.

This paper proposes in Section 3 a new method to address the wind direction uncertainty included in the datasets of large wind farms. The technique is applied to the Horns Rev offshore wind farm due to the large amount of data available. Simulations from the Jensen model,[2,3*] the Larsen model[25] and Fuga[26] are used to validate the robustness of the method in single and multiple wake situations in Section 4 with a discussion of the results. Section 5 presents the main conclusions.

## 2. MEASUREMENTS

The Horns Rev offshore wind farm is located in the North Sea 14 km from the west coast of Denmark. It has a total rated power capacity of 160 MW and consists of 80 pitch-controlled, variable speed Vestas V80 wind turbines (Vestas Wind Systems A/S, Hedeager 44, 8200 Aarhus N, Denmark) with a rotor diameter ($D$) of 80 m and a hub height of 70 m. As shown in Figure 1, the wind turbines are positioned in a regular array of 8 by 10 turbines with a spacing along the main directions of $7D$. The horizontal rows are here referred to rows A to H, whereas the vertical rows are referred to columns 1 to 10. The yaw position sensor of turbine G1 was used to determine the reference wind direction for the westerly sector

*Here, the Jensen model refers to the cluster wake model suggested by Katic *et al.*[3] (also known as Park) using the single wake model of Jensen[2].

(270° ± 65°) as suggested by Hansen *et al.*[22] Due to the lack of calibration of this sensor, the yaw position offset of turbine G1 was derived to ensure the maximum power ratio between G1 and G2 precisely at 270°.

The dataset represents three full years of wind farm operation (January 1, 2005 to December 31, 2007) extracted from the wind farm supervisory control and data acquisition system. The 10 min average statistics were quality controlled and processed as described by Hansen *et al.*.[22] In the current study, all atmospheric stability and turbulence conditions are included. In addition, the dataset was filtered to try to ensure flow stationarity throughout the whole wind farm. As proposed by Hansen *et al.*,[22] this filter considers only the second of two subsequent 10 min periods where both wind speed and wind direction remain within the desired flow case (e.g., 8 m s$^{-1}$ ± 0.5 m s$^{-1}$ and 270°± 2.5°). This criterion is used to exclude periods where the wind farm is partly covered by weather fronts. It is especially restrictive for narrow wind direction sectors.

## 3. NUMERICAL METHODS

This section describes first the basics of the three engineering wake models used in this investigation. The method to post-process the numerical simulations and address the wind direction uncertainty is then presented.

### 3.1. Wake models

The Jensen model, the Larsen model and Fuga are cluster wake models that assume neutral atmospheric stability, although the Jensen and Larsen models have parameters that can be calibrated to work under a range of atmospheric conditions. The three models can compute the wake deficits of large wind farms within seconds on a personal computer and therefore can also be coupled to wind resource software to estimate the annual energy production (AEP).

#### 3.1.1. Jensen model.

From the law of mass conservation, an expression for the wake velocity as a function of distance downstream is derived in the original Jensen model.[2] The initial velocity deficit is calculated from the turbine's thrust coefficient, and the rate of wake expansion is determined through a semi-empirical coefficient ($k$). The total velocity deficit for a given location is calculated as in Katic *et al.*,[3] i.e. as the square root of the sum of squares of the velocity deficits induced by all upstream turbines. In offshore conditions, it is common practice to set $k$ to 0.05 and 0.04 for small and large wind farms, respectively. In this study, the values 0.05 and 0.04 are used for the single wake and multiple wake cases, respectively.

#### 3.1.2. Larsen model.

The Larsen model corresponds to the most recent update of the model from Larsen.[25] The model has a closed form expression of the wake radius and wake velocity based on a simplification of the RANS equations and an empirical calibration of the wake radius at $9.6D$.[25] The velocity recovery and wake expansion are controlled by the turbine's thrust coefficient and the ambient turbulence intensity. The total velocity deficit for a given location is calculated as the linear sum of the velocity deficits induced by all upstream turbines.

A turbulence intensity of 7% is applied to the model for all flow cases investigated in this paper. This value is consistent with measurements documented by Hansen *et al.*[22] for westerly winds of 8 m s$^{-1}$ at Horns Rev.

#### 3.1.3. Fuga.

Fuga is a linear flow solver based on the steady-state RANS equations. It is designed for flat and homogeneous terrain so its main purpose is wake modeling of offshore wind farms. The flow is assumed incompressible and lid driven at a chosen height above the ground. The Reynolds stress tensor is modeled using a simple eddy viscosity turbulence closure. An actuator disc technique accounts for the wind turbine forcing on the flow. No numerical grid is required by the solver, which eliminates user dependence and numerical diffusion. The complete description of the model and its evaluation with wind farm datasets are found in the study of Ott *et al.*.[26]

Fuga is currently implemented as a stand-alone graphical user interface that requires a wind farm layout and wind turbine parameters in WAsP format. In this study, Fuga version 2.0.0.28 is used with a roughness length of 0.0001 m and a boundary layer height of 500 m. These values are consistent with the work from Ott *et al.*[26] and numerical simulations from the Weather Research and Forecasting model.[27]

### 3.2. Simulation post-processing

The wind direction uncertainty of the dataset originates from the yaw misalignment of the reference wind turbine, the spatial variability of the wind direction within the wind farm and the variability of the wind direction within the averaging

period. First, the qualitative impact of these three sources of uncertainty is described and then the post-processing technique used to address the wind direction uncertainty is presented.

### 3.2.1. Sources of wind direction uncertainty.

The yaw misalignment of the reference turbine is caused by the inability of the turbine control strategy to respond instantaneously to natural wind direction variations. Therefore, there is a strong correlation between the behavior of the wind direction and the measured yaw error. Figure 2 shows that a normal distribution fits well the measured wind direction variations within a 10 min period at Horns Rev. These measurements were recorded using a sonic anemometer with a sampling rate of 12 Hz at a height of 50 m.[28] Since the wind direction variations within one averaging period can be assumed to be normally distributed, the yaw error of the reference turbine can also be considered as a normally distributed random variable.

The wind direction uncertainty from spatial variability is correlated with the stochastic behavior of the wind direction. In this case, the uncertainty is caused by the difference of wind direction between the reference turbine and the other turbines in the wind farm. Ott and Longnecker[29] proved that the difference of two normally distributed variables is also normally distributed. Therefore, the wind direction uncertainty between two locations in a wind farm has a normally distributed behavior similar to the wind direction variations at the two locations. Due to spatial coherence, the amplitude of the uncertainty is expected to increase with the distance from the reference location.

Numerical simulations performed for a fixed wind direction are not fully consistent with the fact that the wind direction varies during the averaging period. It can be argued that model calibrations should partly account for the wind direction variations through the prescribed turbulence intensity and rate of wake expansion. However, the drift of the wind direction between two averaging periods is not modeled in the simulations because it corresponds to large-scale weather phenomena. Therefore, a fraction of the random behavior of the wind direction within one averaging period is not modeled and represents a wind direction uncertainty included in the dataset. This uncertainty is greatly decreased in the current study by the flow stationarity filter described in Section 2. However, it is possible that the dataset still includes non-stationary flows because, among others, the filtering process is biased by the yaw misalignment of the reference turbine.

### 3.2.2. Weighted average.

The method to address the wind direction uncertainty is to replace the traditional simulation performed with the 10 min average wind direction by a weighted average of several simulations covering a wide span of directions. Section 3.2.1 emphasized the fact that the wind direction uncertainty is correlated with the normally distributed behavior of the wind direction within one averaging period. Therefore, the average is applied according to the probability weight of a normal distribution centered on the desired wind direction. The weighted average is performed within $\pm 3$ standard deviations ($\sigma_a$) to ensure a cumulative probability of 99.7%. The amplitude of $\sigma_a$ is here considered as a measure of the wind direction uncertainty in the dataset.

The implementation of a weighted average does not increase the computation time significantly because the calculation for one wind direction is already very fast with the three wake models presented in Section 3.1. The wind direction resolution used to perform the simulations in the span of the weighted average is 0.5°.

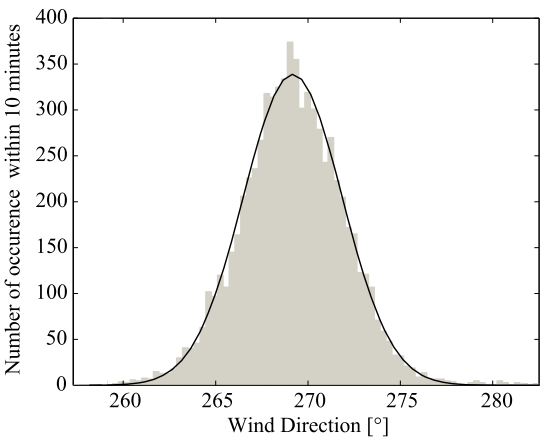


**Figure 2.** Measured wind direction within a 10 min period at Horns Rev using a sonic anemometer with a sampling rate of 12 Hz. The recorded turbulence intensity for the 10 min period was 5.8%. The full line represents a normal fit with a mean direction of 269.2° and a standard deviation of 2.67°.

## 4. RESULTS AND DISCUSSION

The results are divided into two main parts. First, the flow interaction between two wind turbines is analysed to show how the weighted average influences the shape of the power deficit in a single wake condition. Then, the power deficits along the rows of wind turbines are studied to emphasize the performance of the method for narrow and wide directional sectors.

It is worth mentioning that the datasets slightly differ in the two subsections. The single wake flow case represents the wind speed range 8 m s$^{-1}$ $\pm$ 1 m s$^{-1}$, whereas the multiple wake cases correspond to 8 m s$^{-1}$ $\pm$ 0.5 m s$^{-1}$. Nevertheless, all simulations were accomplished for a fixed wind speed of 8 m s$^{-1}$.

### 4.1. Flow interaction between two wind turbines

Figure 3 shows the power of turbine G2 normalized to the reference turbine G1 as a function of wind directions relative to 270°. More precisely, the power of turbine G2 was normalized for each time stamp and then aggregated over the period of the data. The average sample size for each data point corresponds to 5 h of measurements with a bias for stable atmospheric conditions.[22] Similarly to previous wake modeling investigations,[6,21] the error bars included in the plots provide an indication of the scatter in the measurements by illustrating $\pm$0.5 standard deviation of the measured 10 min averages.

A linear moving average of 5° was applied on the results of the weighted simulations to be consistent with data processing.[22] Therefore, the weighted average on the interval $\pm 3\sigma_a$ accounts for the wind direction uncertainty included in the dataset, and the subsequent linear moving average accounts for data binning. The curves with no weighted average ($\sigma_a = 0°$) correspond to the baseline results where the wind direction uncertainty is not addressed.

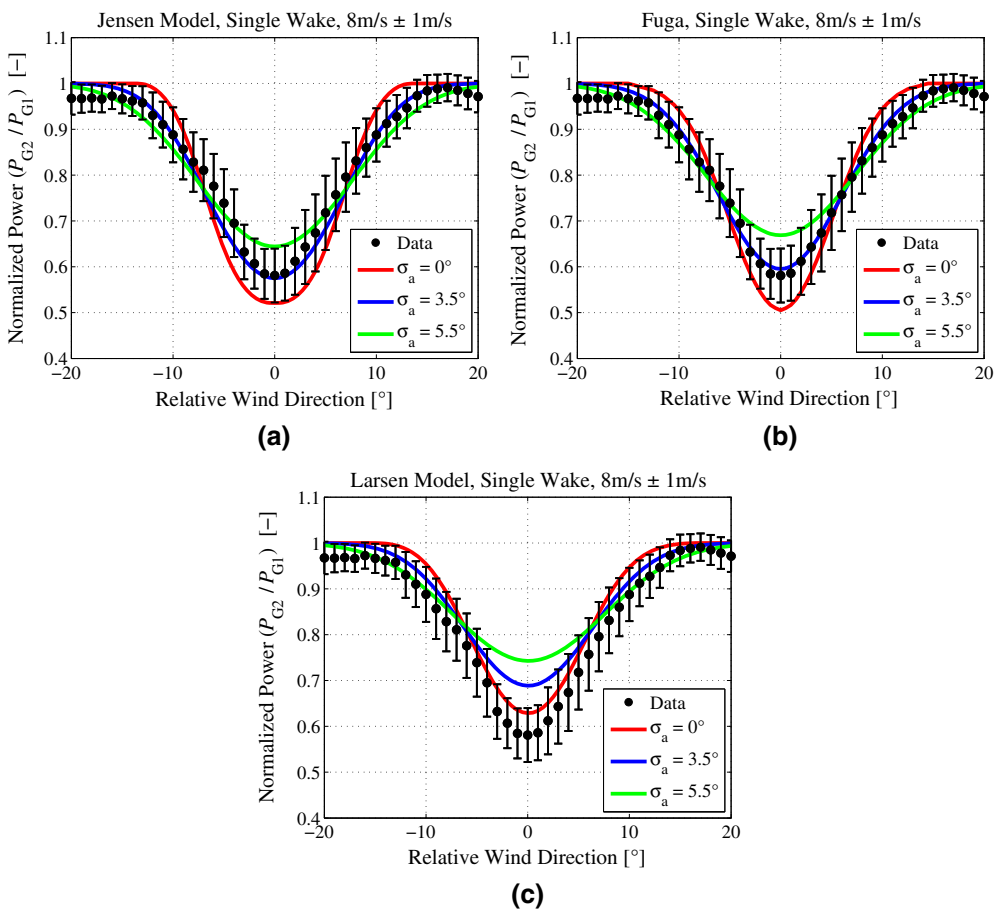


**Figure 3.** Influence of the weighted average on the predictions of (a) the Jensen model, (b) Fuga and (c) the Larsen model. The normalized power of turbine G2 is plotted as a function wind directions relative to 270°. The error bars correspond to $\pm$0.5 standard deviation of the measured normalized power.

For the three models, the normalized power simulated in the interval [−7°,+7°] increases with $\sigma_a$ because the weighted average includes wind directions where the turbine operates in wake free or partial wake conditions. Alternatively, the normalized power in the intervals [−15°,−7°] and [+7°,+15°] decreases with increasing $\sigma_a$ because the weighted average includes more cases where the turbine operates in full wake condition.

The proposed method clearly improves the shape of the normalized power deficit when $\sigma_a = 3.5°$ is applied to both the Jensen model and Fuga. This value is slightly higher than the standard deviation of the wind direction for the 10 min period reported in Figure 2. This difference suggests that $\sigma_a$ cannot be derived directly from the wind data. However, the amplitude of $\sigma_a$ is believed to be an adequate first estimate of the wind direction uncertainty for similar turbine spacings, wind conditions and data processing methods.

It must be underlined that the Larsen model obtains better agreement in terms of the shape when no weighted average is applied. This different behavior might be caused by the empirical calibration of the model from single wake measurements at the Vindeby offshore wind farm.[25] Therefore, the calibrated shape of the normalized power deficit already includes a wind direction uncertainty. Also, the Larsen model might simply overpredict the power production in single wake conditions and fully aligned flow. Indeed, the weighted average improves the agreement of the Larsen model in the intervals [−15°,−7°] and [+7°,+15°], although the overall shape is mispredicted.

### 4.2. Power deficit along rows of wind turbines

Figure 4 presents the averaged power of each column in the wind farm normalized to the production of the reference turbine G1. The simulations and data were averaged over the wind direction sectors 270°±2.5° and 270°±15° in Figure 4(a) and (b), respectively. The average sample size for each data point corresponds to 7 h 40 min for the ±2.5° sector and 757 h for the ±15° sector. The two plots include no weighted average on the simulations to present the baseline performance of the models.

The three models significantly underpredict the power production for the narrow sector (±2.5°), while obtaining good to excellent results for the wide sector (±15°). The correlation between the span of the sector and the accuracy of the wake models was underlined by Gaumond *et al.*[23] and documented in previous studies.[10,24] Due to the wind direction uncertainty described in Section 3.2.1, narrow wind direction sectors of 5° most likely include situations where the turbines operate in conditions outside the span of the sector. This means that the turbines operate more often in wake free or partial wake situations (i.e., higher power outputs) than what is modeled by the numerical simulations. In turn, when the sector width increases the wind direction uncertainty becomes less significant and less cases are filtered in the wrong bins. The agreement in Figure 4(b) is therefore improved because the simulations for wider sectors are more representative of the datasets.

A further investigation of the power production of the individual rows shows that a lateral power gradient exists. Figure 5(a) illustrates the normalized power of rows A, B, E, F and G. The power clearly increases from rows G to A (the normalized power of rows C, D and H is not shown for clarity reasons, but the increasing trend as a function of distance from row G is applicable to all rows[30]). It is worth mentioning that the power of turbine G2 in Figure 5(a) differs

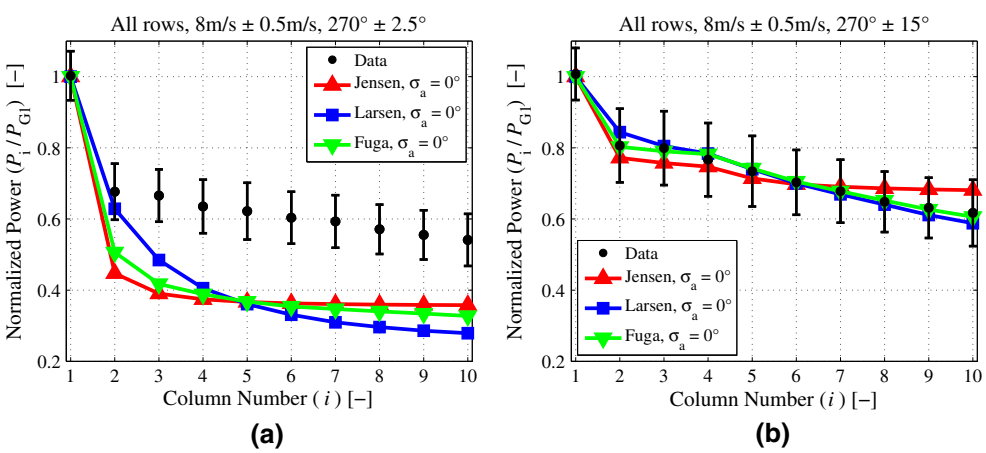


**Figure 4.** Average power of each column of the wind farm (all rows included) normalized to the production of the reference turbine G1 for two different averaging sectors: (a) 270° ± 2.5° and (b) 270° ± 15°. No weighted average was applied on the simulations. The error bars correspond to ± 0.5 standard deviation of the measured power production.

from the power with a relative wind direction of 0° in Figure 3 due to the different wind speed range used in the filtering process. In fact, the results from Hansen *et al.*[22] suggest that Figures 4 and 5(a) represent atmospheric conditions that are less stable than Figure 3.

The results in Figure 5(a) do not necessarily imply that row A generated more power than rows B, E and F, which in turn had a higher power output than row G. In fact, the lateral power gradient is an indication that the estimation of the wind direction is less accurate when the distance from the rows to the reference turbine G1 increases. A less accurate estimation of the wind direction yields more cases that are wrongly filtered in the narrow bin 270°±2.5°. These misfiltered cases correspond to wake free or partial wake situations that increase artificially the power in the rows. Therefore, the lateral power gradient is an artifact of the data processing resulting from the increasing wind direction uncertainty. This aspect should be considered when comparing numerical simulations with power production data because the evaluation of the wake models might vary depending on which row or group of rows is selected for the comparison. With the lowest wind direction uncertainty, row G has probably the most representative behavior of the real power production for the narrow wind direction sector 270°±2.5°.

Figure 5(b) illustrates the normalized power of the turbines located in the second column of the wind farm. It can be seen that the power increases almost linearly from G2 to A2. This result shows that the wind direction uncertainty increases linearly with the distance perpendicular to the mean wind direction. This uncertainty is significant because turbine A2 produces 14% more power than G2 for the same wind direction sector. To account for the uncertainty from spatial variability of the wind direction, the simulations from Fuga are fitted to the data of column 2 in Figure 5(b) using a row-specific $\sigma_a$ value. Fuga is here used because it is the most accurate model for the wide sector (Figure 4(b)), where the uncertainty is assumed negligible. Fitting the simulations from Fuga for the narrow sector therefore provides the most accurate estimate of the uncertainty. These values are presented in Table I, where it is observed that $\sigma_a$ increases proportionally to the distance from row G where the reference turbine is located.

Figure 6 shows the results when the weighted average technique is applied to the simulations using the row-specific $\sigma_a$ from Table I. The results for the narrow sector in Figure 6(a) are significantly improved compared with those in Figure 4(a). Interestingly, the fitted row-specific $\sigma_a$ for the second turbine in each row also improves the agreement of the remaining turbines in the rows. The apparent absence of an increased uncertainty along the rows is consistent with the stationary flow filter that intends to ensure uniform downstream conditions. As underlined by Gaumond *et al.*[23] for the Lillgrund offshore wind farm, an increasing wind direction uncertainty along the rows is possible when the dataset is processed with a short averaging period and the absence of a stationary flow filter.

The accuracy of the three models for the wide sector 270°±15° remains almost unchanged when using the row-specific $\sigma_a$ (Figure 6(b)) compared with the results for $\sigma_a = 0°$ (Figure 4(b)). This outcome shows that the weighted average methodology based on the normal probability distribution is a robust tool to address the wind direction uncertainty because it does

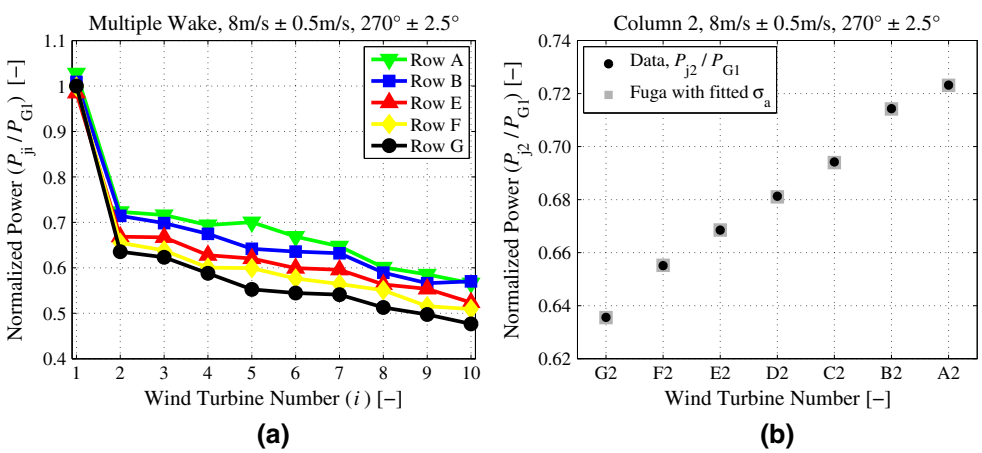


**Figure 5.** (a) Power production data of rows A, B, E, F and G normalized to the reference turbine G1 for the sector 270° ± 2.5°. (b) Normalized power of the second turbine in rows A to G for the sector 270° ± 2.5°. The fitted values of $\sigma_a$ from Fuga are in Table I.

**Table I.** Fitted $\sigma_a$ values to the normalized power of the second turbine in each row for the sector 270° ± 2.5°.

| Turbine number | A2 | B2 | C2 | D2 | E2 | F2 | G2 | H2 |
|---|---|---|---|---|---|---|---|---|
| Fitted $\sigma_a$ with Fuga | 7.4° | 7.0° | 6.2° | 5.8° | 5.4° | 5.0° | 4.5° | 4.8° |

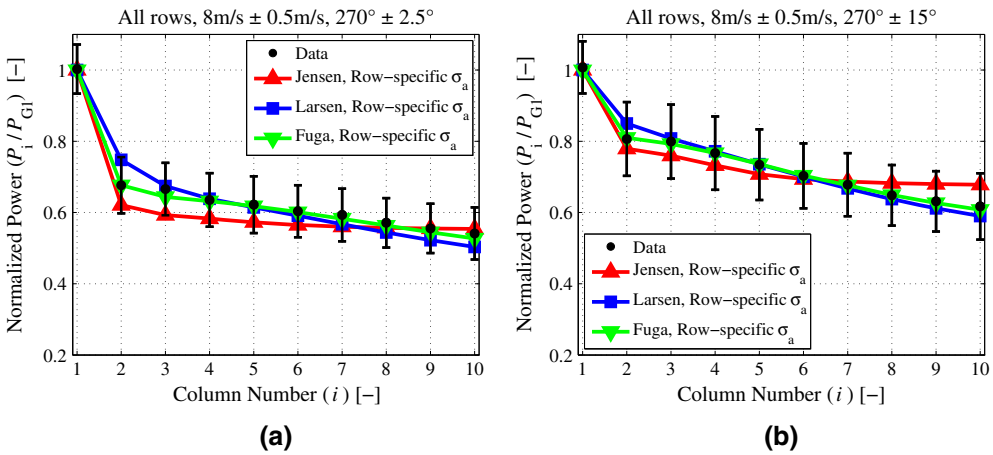


**Figure 6.** Average power of each column of the wind farm (all rows included) normalized to the production of the reference turbine G1 for two different averaging sectors: (a) 270° ± 2.5° and (b) 270° ± 15°. The weighted average was applied on the simulations using the row-specific $\sigma_a$ from Table I. The error bars correspond to ± 0.5 standard deviation of the measured normalized power.

not alter the performance of the wake models. As mentioned in Section 4.1 for the single wake situation, the weighted average technique also improves the shape of the power deficit, which results in a better agreement for both the narrow and wide directional sectors in multiple wake situations.

Table II shows the results of the efficiency of the Horns Rev wind farm with all wind turbines operating. The simulations with $\sigma_a = 0°$ correspond to the baseline results where the wind direction uncertainty is not addressed. The results confirm that the wake models predict accurately the power production of the wind farm for the averaging sector 270° ± 15° independently of the method used. However, the proposed weighted average technique improves the agreement of the simulations for the narrow sector to a 1% margin with the Larsen model and Fuga.

Two potential applications of the method are wind farm control algorithm and layout optimization because they require accurate predictions for narrow wind direction sectors. However, the post-processing technique does not seem to be highly valuable for the computation of the AEP because in this case the simulations are commonly averaged over wind direction sectors of 30°.

It is worth mentioning that although the three models accurately predict the efficiency of the wind farm for the wide sector in Table II, the Larsen model and Fuga capture more accurately the reduction of power along the rows in Figures 4(b) and 6(b). Alternatively, the high accuracy of the Jensen model (+0.1%) is caused by balancing errors from the underprediction of the first five columns and the overprediction of the last four ones. If the number of columns in each row was higher, the Larsen model and Fuga would potentially still make accurate power predictions of the last turbines in the rows, whereas the Jensen model would probably overpredict their power. This is an important aspect to consider when predicting wakes with such models because the size of future wind farms will likely increase. The overprediction of the Jensen model can however be mitigated by reducing the value of $k$ for deeper turbines in the array.[31]

Our results indicate that the discrepancies between the traditional numerical simulations and power production data for narrow wind direction sectors are not caused by an inherent inaccuracy of the engineering wake models, but rather by a large wind direction uncertainty included in the dataset. Therefore, modifying the wake model parameters to fit specific measurements for narrow sectors[10,19] is a risky approach that might deteriorate AEP predictions based on wide sectors.

**Table II.** Efficiency of the Horns Rev wind farm at 8 m s$^{-1}$ ± 0.5 m s$^{-1}$.

| Averaging sector | 270°± 2.5° | 270°± 15° |
|---|---|---|
| Measured wind farm efficiency | 64.7% | 73.9% |
| Jensen model with $\sigma_a = 0°$ | −20.9% | +0.4% |
| Larsen model with $\sigma_a = 0°$ | −20.9% | −0.1% |
| Fuga with $\sigma_a = 0°$ | −21.7% | −0.3% |
| Jensen with row-specific $\sigma_a$ | −3.1% | +0.1% |
| Larsen with row-specific $\sigma_a$ | −0.7% | −0.2% |
| Fuga with row-specific $\sigma_a$ | −0.8% | −0.2% |

In addition, this kind of calibration includes the specific dataset uncertainty, which might not be applicable to another wind farm. Figure 5(a) clearly illustrates that even within the same wind farm, the choice of row would influence the model calibration.

## 5. CONCLUSION

A method to address the wind direction uncertainty included in the dataset of the Horns Rev offshore wind farm is presented. The method replaces the traditional simulations performed with the 10 min average wind direction by a weighted average of several simulations covering a wide span of directions. The weighted average is based on a normal probability distribution to account for the uncertainty from the yaw misalignment of the reference turbine, the spatial variability of the wind direction inside the wind farm and the variability of the wind direction within the averaging period.

The results show that the post-processing technique improves the agreement of the simulations for single and multiple wake cases. The shape of the power deficit is more consistent with the dataset, and the underpredictions of the models for narrow wind direction sectors are significantly improved. The robustness of the method is verified using three different wake models, namely the Jensen model, the Larsen model and Fuga. The results show that the discrepancies between the results of numerical simulations and power production data for narrow wind direction sectors in previous studies[10,12,23,24] were not caused by an inherent inaccuracy of the models, but rather by a large wind direction uncertainty in the dataset.

Future work shall verify if the proposed method can consistently improve the simulation results at other large wind farms. In addition, further investigations should attempt to quantify the wind direction uncertainty independently of the wake models applied. It would be interesting to establish a correlation between the standard deviation of the wind direction within the averaging period and the value of $\sigma_a$.

## ACKNOWLEDGEMENTS

Vattenfall and DONG Energy are acknowledged for providing measurement data. This work was funded by the Natural Sciences and Engineering Research Council of Canada and the Fonds Québécois de la Recherche sur la Nature et les Technologies. Additional funding was provided by the EUDP WakeBench contract 64011-0308 and EERA DTOC contract FP7-ENERGY-2011/n 282797.

## REFERENCES

1. Barthelmie RJ, Hansen K, Frandsen ST, Rathmann O, Schepers JG, Schlez W, Phillips J, Rados K, Zervos A, Politis ES, Chaviaropoulos PK. Modelling and measuring flow and wind turbine wakes in large wind farms offshore. *Wind Energy* 2009; **12**: 431–444.
2. Jensen NO. A note on wind generator interaction. *Technical Report Risø-M-2411*, Risø National Laboratory, Roskilde, 1983.
3. Katic I, Højstrup J, Jensen NO. A simple model for cluster efficiency, *Proceedings of the European Wind Energy Association Conference*, Rome, 1986; 407–410.
4. Ainslie JF. Calculating the flowfield in the wake of wind turbines. *Journal of Wind Engineering and Industrial Aerodynamics* 1988; **27**: 213–224.
5. Schlez W, Neubert A. New developments in large wind farm modelling, *Proceedings of the European Wind Energy Association Conference*, Marseille, 2009.
6. Barthelmie RJ, Jensen LE. Evaluation of wind farm efficiency and wind turbine wakes at the Nysted offshore wind farm. *Wind Energy* 2010; **13**: 573–586.
7. Frandsen S, Barthelmie R, Pryor S, Rathmann O, Larsen S, Højstrup J, Thøgersen M. Analytical modelling of wind speed deficit in large offshore wind farms. *Wind Energy* 2006; **9**: 39–53.
8. Frandsen ST, Jørgensen HE, Barthelmie R, Rathmann O, Badger J, Hansen K, Ott S, Rethore PE, Larsen SE, Jensen LE. The making of a second-generation wind farm efficiency model complex. *Wind Energy* 2009; **12**: 445–458.
9. Sanderse B, Pijl SP, Koren B. Review of computational fluid dynamics for wind turbine wake aerodynamics. *Wind Energy* 2011; **14**: 799–819.
10. Garza J, Blatt A, Gandoin R, Hui SY. Evaluation of two novel wake models in offshore wind farms, *Proceedings of the European Wind Energy Association Offshore Conference*, Amsterdam, 2011.
11. Montavon C, Hui SY, Graham J, Malins D, Housley P, Dahl E, Villiers P, Gribben B. Offshore wind accelerator: wake modelling using CFD, *Proceedings of the European Wind Energy Association Conference*, Brussels, 2011.

12. Ivanell S, Mikkelsen RF, Sørensen JN, Hansen KS, Henningson D. The impact of wind direction in atmospheric BL on interacting wakes at Horns Rev wind farm, *Proceedings of the Science of Making Torque from Wind Conference*, Heraklion, 2010; 407–426.
13. Troldborg N, Sørensen JN, Mikkelsen R. Numerical simulations of wake characteristics of a wind turbine in uniform inflow. *Wind Energy* 2010; **13**: 86–99.
14. Troldborg N, Larsen GC, Madsen HA, Hansen KS, Sørensen JN, Mikkelsen R. Numerical simulations of wake interaction between two wind turbines at various inflow conditions. *Wind Energy* 2011; **14**: 859–876.
15. Churchfield MJ, Lee S, Moriarty PJ, Martinez LA, Leonardi S, Vijayakumar G, Brasseur JG. A large-eddy simulation of wind-plant aerodynamics, *50th American Institute of Aeronautics and Astronautics Meeting*, Nashville, TN, 2012; 1–19.
16. El Kasmi A, Masson C. An extended $k-\epsilon$ model for turbulent flow through horizontal-axis wind turbines. *Journal of Wind Engineering and Industrial Aerodynamics* 2008; **96**: 103–122.
17. Réthoré PE, Sørensen NN, Bechmann A, Zhale F. Study of the atmospheric wake turbulence of a CFD actuator disc model, *Proceedings of the European Wind Energy Association Conference*, Marseille, 2009.
18. Réthoré PE, Sørensen NN, Bechmann A. Modelling issues with wind turbine wake and atmospheric turbulence, *Proceedings of the Science of Making Torque from Wind Conference*, Heraklion, 2010; 349–357.
19. Rados KG, Prospathopoulos JM, Stefanatos NC, Politis ES, Chaviaropoulos PK, Zervos A. CFD modeling issues of wind turbine wakes under stable atmospheric conditions, *Proceedings of the European Wind Energy Association Conference*, Marseille, 2009.
20. Phillips JL, Cox SD, Henderson AR, Gill JP. Wake effects within and between large wind projects: the challenge of scale, density and neighbours – onshore and offshore, *Proceedings of the European Wind Energy Association Conference*, Warsaw, 2010.
21. Barthelmie RJ, Pryor SC, Frandsen ST, Hansen KS, Schepers JG, Rados K, Schlez W, Neubert A, Jensen LE, Neckelmann S. Quantifying the impact of wind turbine wakes on power output at offshore wind farms. *Journal of Atmospheric and Oceanic Technology* 2010; **27**: 1302–1317.
22. Hansen KS, Barthelmie RJ, Jensen LE, Sommer A. The impact of turbulence intensity and atmospheric stability on power deficits due to wind turbine wake at Horns Rev wind farm. *Wind Energy* 2012; **15**: 183–196.
23. Gaumond M, Réthoré PE, Bechmann A, Ott S, Larsen GC, Peña A, Hansen KS. Benchmarking of wind turbine wake models in large offshore wind farms, *Proceedings of the Science of Making Torque from Wind Conference*, Oldenburg, 2012.
24. Beaucage P, Robinson N, Brower M, Alonge C. Overview of six commerical and research wake models for large offshore wind farms, *Proceedings of the European Wind Energy Association Conference*, Copenhagen, 2012; 95–99.
25. Larsen GC. A simple stationary semi-analytical wake model. *Technical Report Risø-R-1713(EN)*, Risø National Laboratory, Roskilde, 2009.
26. Ott S, Berg J, Nielsen M. Linearised CFD models for wakes. *Technical Report Risø-R-1772(EN)*, Risø National Laboratory, Roskilde, 2011.
27. Peña A, Gryning SE, Hahmann AN. Observations of the atmospheric boundary layer height under marine upstream flow conditions at a coastal site. *Journal of Geophysical Research* 2013; **118**: 1924–1940. DOI: 10.1002/jgrd.50175.
28. Peña A, Hahmann AN. Atmospheric stability and turbulence fluxes at Horns Rev - an intercomparison of sonic, bulk and WRF model data. *Wind Energy* 2012; **15**: 717–731.
29. Ott RL, Longnecker M. *An Introduction to Statistical Methods and Data Analysis*, (6 edn). Brooks/Cole, Cengage Learning: Belmont, California, 2010.
30. Hansen KS, Barthelmie R, Jensen LE, Sommer A. Power deficits due to wind turbine wakes at Horns Rev wind farm, *Proceedings of the Science of Making Torque from Wind Conference*, 2010; 40–46.
31. Peña A, Rathmann O. Atmospheric stability dependent infinite wind farm models and the wake decay coefficient. *Wind Energy* 2012.

# Evaluation of a RANS solver performance in offshore wind farms.

**John Prospathopoulos, George Sieros, Panagiotis Chaviaropoulos**

10-7-2013


| | |
|---|---|
| Agreement n.: | FP7-ENERGY-2011-1/ n°282797 |
| Duration | January 2012 to June 2015 |
| Co-ordinator: | DTU Wind Energy, Risø Campus, Denmark |

Support by:

## Document information

| | |
|---|---|
| **Document Name:** | Evaluation of a RANS solver performance in offshore wind farms |
| **Document Number:** | Contribution of CRES to D1.3 |
| **Author:** | John Prospathopoulos (CRES) |
| **Date:** | 10-7-2013 |
| **WP:** | WP1 |
| **Task:** | Task1.1 |

# TABLE OF CONTENTS

Table of contents

TABLE OF CONTENTS ..... 3

1 INTRODUCTION ..... 4

2 NUMERICAL MODELS ..... 5
2.1 CRES-flowNS model ..... 5

2.1.1 Wind turbine simulation ..... 5

2.1.2 Computational domain and boundary conditions ..... 6
2.2 GCL model ..... 6

2.2.1 Mean wind deficit ..... 6

2.2.2 Turbulence intensity ..... 7

2.2.3 Application on wind farms ..... 7

3 HORNS REV OFFSHORE WIND FARM ..... 8
3.1 Wind farm description ..... 8
3.2 Definition of power deficit ..... 8
3.3 Numerical simulation ..... 8
3.4 Wind speed sector size variation ..... 9
3.5 Wind speed direction variation ..... 10
3.6 Turbulence variation ..... 11
3.7 Atmospheric stratification ..... 11
3.8 Spacing ..... 11
3.9 Power polar ..... 13

4 LILLGRUND OFFSHORE WIND FARM ..... 19
4.1 Wind farm description ..... 19
4.2 Numerical simulation ..... 19
4.3 Sector variation ..... 19
4.4 Wind speed recovery ..... 22

5 CONCLUSIONS ..... 26

6 REFERENCES ..... 27

# 1 INTRODUCTION

The need for reliable wake modelling has been recognized for many years and various models have been developed to simulate the wind turbine wakes. These methodologies, initially developed for single wind turbines have been extended to the simulation of wind farms, where a wind turbine may be located in the wakes of the neighbouring turbines. Evaluation of the main wind farm models was carried out in the context of the UpWind project using experimental data from the Danish offshore wind farm Horns Rev [1]. The models involved were of varying complexity, including the straightforward model WAsP [2] , the moderately complex model WindFarmer [3] , the WAKEFARM [4] model based on parabolized Navier–Stokes equations, and advanced models solving the full 3D Navier–Stokes [5,6]. Predictions were compared with measurements for the wind direction of 270$^o$ at various sector widths (±1$^o$, ±5$^o$, ±10$^o$, ±15$^o$). The preliminary results indicated that the CFD models over-predict wake losses in the narrow sectors, while the simpler wind farm models tend to under-predict wake losses unless their coefficients are calibrated to match the observations.

In the context of the EERA-DTOC project the aim was to further assess the performance of the existing wind farm models using a range of high quality cases for model simulation. Thus, a number of benchmark cases were defined to investigate complex relationships between wind speed, wind turbine spacing, turbulence and stability offshore and how well the suite of selected models perform. Detailed experimental data sets from the Horns Rev and Lillgrund offshore wind farms were made available from DTU for comparison with the predictions of the models.

In the present document, the results of a number of benchmark simulations using the CRES-flowNS [6] RANS solver are reported. They include variation of the wind turbine spacing, size of the wind sector, turbulence and atmospheric stratification. Furthermore, predictions of the park efficiency for the whole wind rose are given with the engineering model GCL [7] calibrated with the CFD predictions for certain wind directions.

# 2 NUMERICAL MODELS

## 2.1 CRES-flowNS model

CRESflow-NS [6] is an in-house RANS solver using the k-ω turbulence model for closure and the actuator disk theory for the simulation of the embedded wind turbines. It has been applied to the simulation of single wind turbine wakes, as well as small and large wind farms in flat and complex terrain [8] [9] . The momentum equations are numerically integrated introducing a matrix-free pressure correction algorithm which maintains the compatibility of the velocity and pressure field corrections. Discretization is performed with a finite volume technique using a body-fitted coordinate transformation on a structured curvilinear mesh. Convection terns are handled by a second order upwind scheme bounded through a limiter, whereas centred second order schemes are employed for the diffusion terms. Velocity-pressure decoupling is prevented by a linear fourth order dissipation term added into the continuity equation. The *k-ω* turbulence model has been suitably modified for neutral atmospheric conditions [10] :

$$\alpha = 0.3706, \quad \beta = 0.0275, \quad \beta_* = 0.033,$$
$$\sigma = 0.5, \quad \sigma_* = 0.5 \tag{1}$$

Stratification is considered through an additional production term *f·G* added to each one of the *k* and *ω* transport equations to account for the buoyancy effect [3] . The production term *G* is given from the following relationship [11] :

$$G = -\mu_t \left( \frac{\partial U}{\partial z} \right)^2 \cdot \frac{Ri}{f_m}, \quad Ri = \zeta \frac{0.74 + 4.7\zeta}{(1 + 4.7\zeta)^2}, \quad f_m = 1 + 5\zeta, \quad \zeta = z / L \tag{2}$$

where $\mu_t$ is the eddy viscosity and *Ri* is the Richardson number. The *f* function is estimated for the *k* and *ω* equations ($f_k$ and $f_\omega$) respectively, so that the simplified momentum and transport equations for constant pressure (*dp/dx=0*) are fulfilled. After a proper mathematical analysis, the following functions $f_k$ and $f_\omega$ are derived for the *k* and *ω* transport equations:

$$f_k = 1 + 4.9\zeta, \quad f_\omega = -14 \cdot (1 + 1.28\zeta) \quad \text{for stable conditions} \tag{3}$$

$$f_k = 1 - 1 / Ri, \quad f_\omega = \frac{1 / Ri - 1}{\sigma \cdot \beta^* \cdot \kappa^2 / \beta^{1.5} - 1} \quad \text{for unstable conditions} \tag{4}$$

### *2.1.1 Wind turbine simulation*

According to the actuator disk approach, the rotor of each wind turbine is simulated as a disk discretized by a number of control volumes. Each control volume acts as a momentum sink through the actuator force calculated using the following relationship:

$$F = 0.5\rho \, U_{ref}^2 \, C_T \, \Delta S \tag{5}$$

where *ρ* stands for the air density, $U_{ref}$ is the reference wind speed for the thrust coefficient calculation, $C_T$ is the thrust coefficient and *ΔS* is the surface area of the control volume. One of the major challenges in the actuator disk theory is the determination of the reference velocity for thrust calculation.

The reference velocity $U_{ref}$ is estimated at the position of each wind turbine as if the specific turbine was absent. In offshore wind farms, wind turbines are mostly installed in parallel rows, so turbine rows can be considered instead of single turbines. A parabolic procedure is then applied: The run starts ignoring the presence of the turbines to estimate the reference velocities at the positions of the first row. When a certain convergence criterion is fulfilled for the velocities at those positions, the actuator disks are activated at the first row. The simulation continues and the reference velocities are estimated at the second row. This procedure is repeated until all turbine rows are added. Namely, a successive activation of turbine rows occurs when a certain convergence criterion is fulfilled for the velocities at the specific positions of that row.

### 2.1.2 Computational domain and boundary conditions

The wind farm is enclosed in a computational domain with assumed known inflow conditions, corresponding to the downstream conditions of the affecting upstream installations. If there is no upstream installation free stream logarithmic profiles for neutral or stratified conditions are applied to the inlet boundary according to the similarity theory [12] . The outflow and the side boundaries are positioned sufficiently far so that Neumann conditions can be applied for the velocities and the *k,ω* turbulence quantities. The inlet and outlet boundaries are positioned *10 D* and *30 D* upstream and downstream of the first and last wind turbine rows respectively. The side boundaries are positioned *10 D* away of the closest wind turbine and finally the top boundary is positioned nearly *30 D* above sea level. Logarithmic wall functions are implemented for the first grid point above the sea level.

The mesh is kept fine close to the wind turbine rotors in the horizontal *x, y* directions with a minimum grid spacing close to *0.1 D*. Between the turbine rotors successive coarsening and refinement of the grid lines occurs using geometrical progression. In the vertical direction the mesh is constructed fine close to the sea level with the first grid line at a distance of about *0.007 D*. A fine mesh is also constructed in the area of each W/T rotor disk, using *15* grid points along the rotor diameter.

## 2.2 GCL model

The GCL model [7] encompasses a semi–analytical description of the wake deficit and a set of simple empirical relations providing the relevant characteristics for the turbulence field in the wake. The empirical expressions are based on full scale measurements and are applicable for both stall , pitch and variable speed regulated turbines. In order to enable the treatment of data from model experiments performed in wind tunnels, the expression for the turbulence intensity has been made non-dimensional. Moreover, one of the boundary conditions for the deficit model was modified in order to reflect the blocking effect from the ground.

### 2.2.1 Mean wind deficit

Neglecting the blocking effect originating from the ground, the wake behind a wind turbine is considered as a free turbulence region. The model is based on the presumptions that the wake region can be adequately described by Prandtl's axisymmetric turbulent boundary layer equations [13] and that self-similarity of the profiles holds. Therefore, wake radius $\delta$ and centerline velocity $U_s$ follow the power laws of *1/3* and *(-2/3)* respectively. The accurate expressions are obtained using the empirical condition that the radius of the wake at *9.5* rotor diameters is given by

$$R_{9.5} = \frac{1}{2}\left(R_{nb} + min\left(z_{hub}, R_{nb}\right)\right), \quad R_{nb} = max\left\{1.08D, 1.08D + 21.7\left(I_a - 0.05\right)\right\}, \tag{6}$$

where $z_{hub}$ is the hub height, $D$ is the rotor diameter and $I_a$ is the ambient turbulence intensity. This relationship denotes that the expansion of the wake is dominated by ambient turbulence and ensures a minimum turbulence level of 5%. The blocking effect is taken into account by applying a wake radius equal to the mean of $z_{hub}$ and $R_{nb}$ at *9.5D* distance when wake radius exceeds hub height. Thus, the formula for the wake radius becomes:

$$\frac{\delta(x)}{D} = 0.5 \cdot \left(1 + \frac{C_T \cdot x}{x_0}\right)^{1/3}, \qquad x_0 = \frac{9.5 \cdot D}{\left(2 \cdot R_{9.5} / D\right)^3 - 1} \tag{7}$$

where $C_T$ is the thrust coefficient.

The centerline velocity is derived from the momentum integral in the wake region:

$$\frac{U_s(x)}{U_\infty} = \frac{35}{72} \cdot \left(\frac{D}{\delta(x)}\right)^2 \cdot C_T \tag{8}$$

where $U_\infty$ is the ambient wind speed.

### 2.2.2 Turbulence intensity

In the far wake, it is assumed that only the surface and wake shear mechanisms contribute significantly to turbulence production. Moreover, the turbulence fluctuations originating from these two sources are considered statistically independent, so the turbulent energies can be superimposed. Normalizing with respect to the undisturbed mean wind velocity, the total turbulence intensity of the axial turbulence component in the wake, is expressed as

$$I_t = \sqrt{I_a^2 + I_w^2} \tag{9}$$

where subscripts *a* and *w* refer to ambient and wake respectively. The wake contribution, $I_w$, depends on both the downstream distance and the undisturbed mean wind velocity and is determined as :

$$I_w = 0.29 \cdot \left(\frac{x}{D}\right)^{-\frac{1}{3}} \sqrt{1-\sqrt{1-C_T}} \tag{10}$$

where S denotes the spacing expressed in rotor diameters.

### 2.2.3 Application on wind farms

GCL model was developed for the estimation of the velocity deficit and the turbulence level within the wake of a single wind turbine. In the case of a wind farm, a wind turbine is subject to the effect of multiple wakes. To calculate the incoming speed on the rotor of the *i-th* wind turbine, the individual effects are summed up according to:

$$\left(U_\infty - U_i\right)^2 = \sum_{j=1}^{N_T}\left[\left(U_j - u_{ij}\right)^2\right] \tag{11}$$

where $U_j$, $U_j$ are the onset velocities of the *i-th*, *j-th* wind turbines respectively and $u_{ij}$ is the velocity induced to the *i-th* wind turbine by the wake of the *j-th* wind turbine, estimated through Eq.(8), as shown schematically in Figure 1

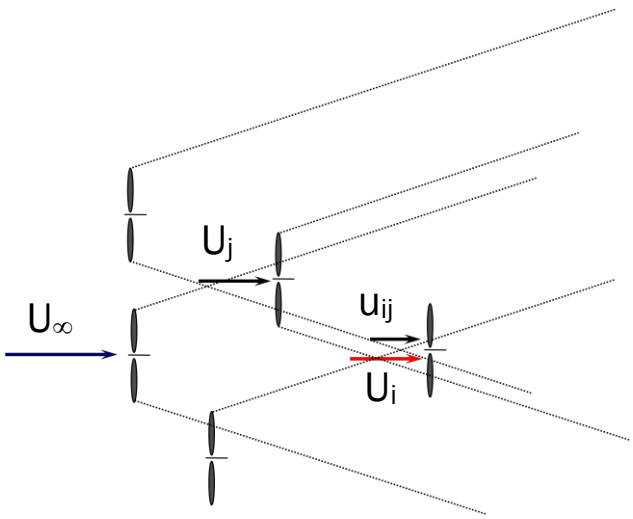


Figure 1: Schematic representation of the interaction between the *i-th* and *j-th* wind turbines. $U_j$, $U_j$ are the onset velocities of the *i-th*, *j-th* wind turbines and $u_{ij}$ is the velocity induced to the *i-th* wind turbine by the wake of the *j-th* wind turbine

# 3 HORNS REV OFFSHORE WIND FARM

## 3.1 Wind farm description

The Horns Rev wind farm is located *14 km* from the west coast of Denmark, with a water depth of *6-14 m*. The wind farm has a rated capacity of *160 MW* comprising 80 wind turbines, which are arranged in a regular array of *8* by *10* turbines, with a spacing of *560 m* in both directions covering an area of *5x3.8 km*$^2$. The layout of the wind farm, shown in Figure 2, is not completely rectangular, while the direction of the N-S columns is *353°*. The wind turbines are installed with an internal spacing along the main directions of *7 D*. The diagonal wind turbine spacing is either *9.4 D* or *10.4 D*. The wind farm comprises VESTAS V80 turbines, which are *2 MW* pitch controlled, variable speed wind turbines with a diameter of *80 m* and *70 m* hub height. It has been in operation since 2004 and the SCADA statistics from 2005-2007 is available for the wake analysis [14] .

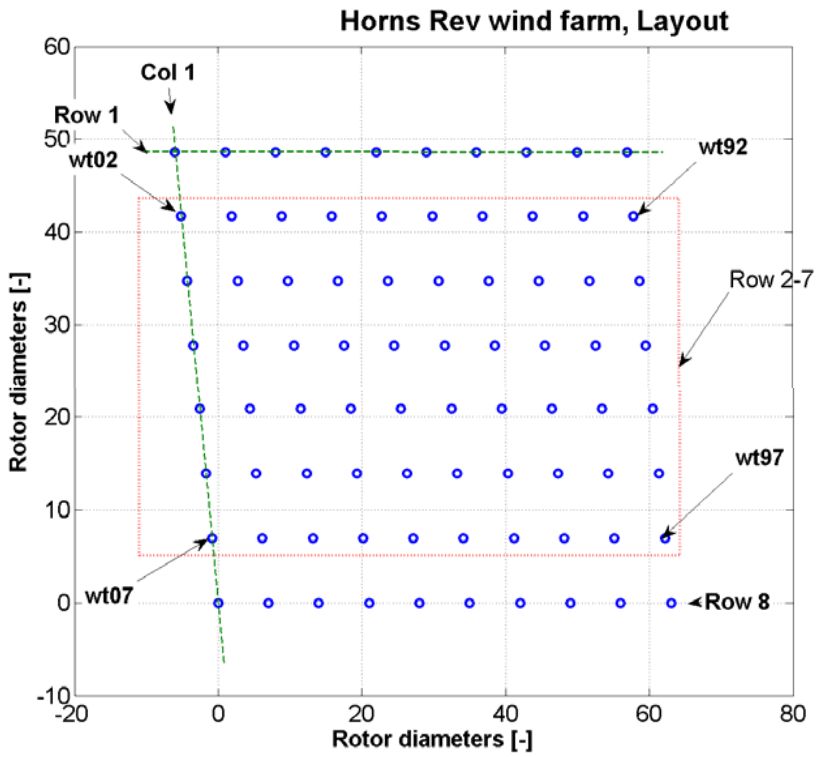


Figure 2: Layout of the Horns Rev offshore wind farm

## 3.2 Definition of power deficit

For westerly inflow, the power deficit is determined with respect to the reference wt07:
Power Deficit= *(Pwt07- Pwt)/Pwt07*
For easterly inflow, the power deficit is determined with respect to the reference wt95:
Power Deficit= *(Pwt9 - Pwt)/Pwt95*
The mean power deficit is determined by averaging the results for rows *2-7* as function of spacing (see Figure 2). In order to model the wind turbines the official thrust and power curves, were used.

## 3.3 Numerical simulation

In order to simulate the western wind directions *(270°±15°)*, *12* sub-sectors of *2.5°* were considered. For each one of the sub-sectors the mean wind direction was simulated, e.g. for the sub-sector *270°-2.5°*, the simulated mean wind direction was *268.75°*. Next, two sub-domains, marked with blue lines in Figure 3, were considered. The first one including rows *1-3* was used for the simulation of the wind directions *268.75°-283.75°* and the second one including rows 6-8 was used for the simulation of the wind directions *256.25° -266.25°*. It was found that when the

first sub-domain was used, rows *1-3* were not affected by the wind turbine wakes from rows *4-8*. In addition, the flow field at the *4th-8th* rows was similar to the flow field at the *3rd* row. In the same way, when the second sub-domain was used, rows *6-8* were not affected by the wind turbine wakes from rows *1-5* and the field at the *1st-5th* rows was similar to the flow field at the *6th* row. Thus, simulation of one sub-domain instead of the whole wind farm is acceptable and saves significant computational cost.

For each simulation, the x-axis of the computational domain was aligned to the wind direction resulting in a transformation of the coordinates of the W/T positions. A successive refinement and coarsening of the grid lines was made in order to achieve a fine mesh close to the W/T positions (Figure 4). The minimum grid size in both *x* and *y* directions was between *0.1 D* and *0.15 D.*

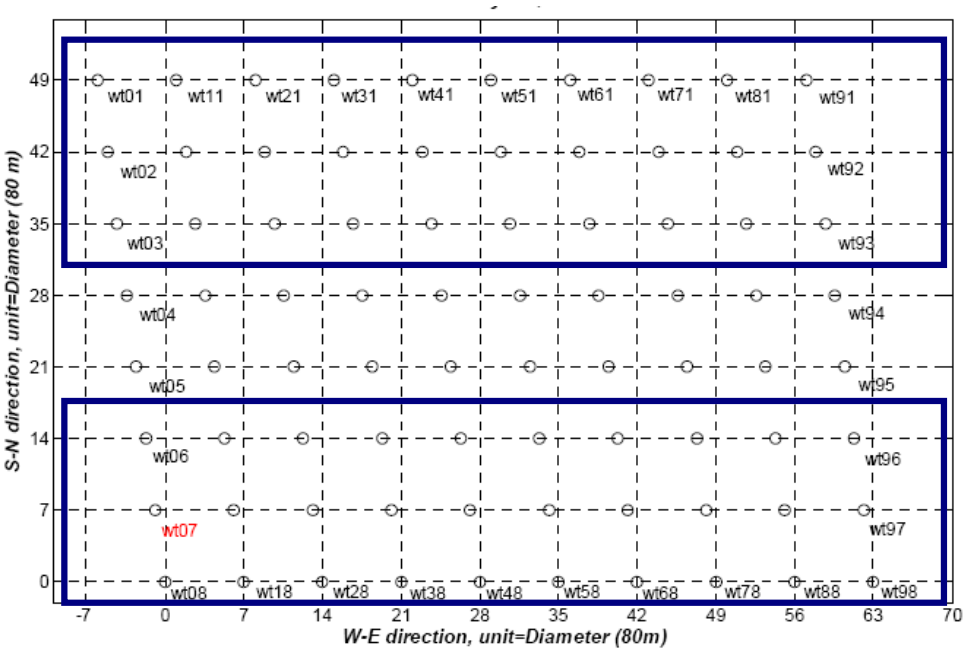


Figure 3: The two sub-domains used for the simulation of the western wind directions. The sub-domain including rows *1-3* is used for the simulation of the wind directions *268.75°-283.75°* and the sub-domain including rows *6-8* is used for the simulation of the wind directions *256.25 ° - 266.25 °.*

Estimation of the reference velocities at the wind turbine positions, required for the thrust and power calculation is performed using the parabolic procedure described in Section 2.1.1. The convergence of the momentum equations for the *273.75°* wind direction is shown in Figure 5. The appearance of peaks indicates the activation of each wind turbine column.

### 3.4 Wind speed sector size variation

The inflow mean velocity at hub height (*70 m*) was *8 m/s* and the inflow turbulence intensity at hub height was *7%*. Three cases were defined to validate the influence of the flow sector size for western wind directions: *270°±2.5°*, *270°±7.5°* and *270°±15°*. Numerical simulations were performed with a step of *±2.5°* starting from *270°±1.25°*. In order to estimate the power output for the flow sector *270°±2.5°*, the average of the *270°+1.25°* (middle of the *270°+2.5°* sector) and *270°-1.25°* (middle of the *270°-2.5°* sector) simulations was calculated. Accordingly, to estimate the power output for the flow sector *270°±7.5°*, the average of the *270°±1.25°*, *270°±3.75°* and *270°±6.25°* simulations was calculated. The predicted mean power deficits are compared with measurements in Figure 6. It is observed that the agreement between predictions and measurements is improved as the flow sector size increases. For a size of *±15°* predictions well agree with the measurements.

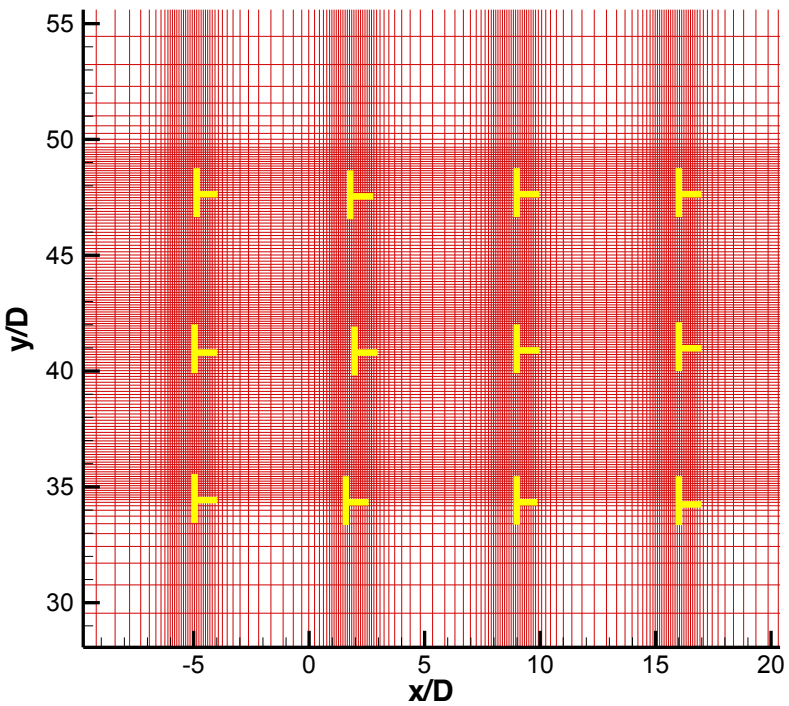


Figure 4: Grid construction for the Horns Rev wind farm. Grid refinement is made close to the wind turbine rotors in both *x,y* directions.

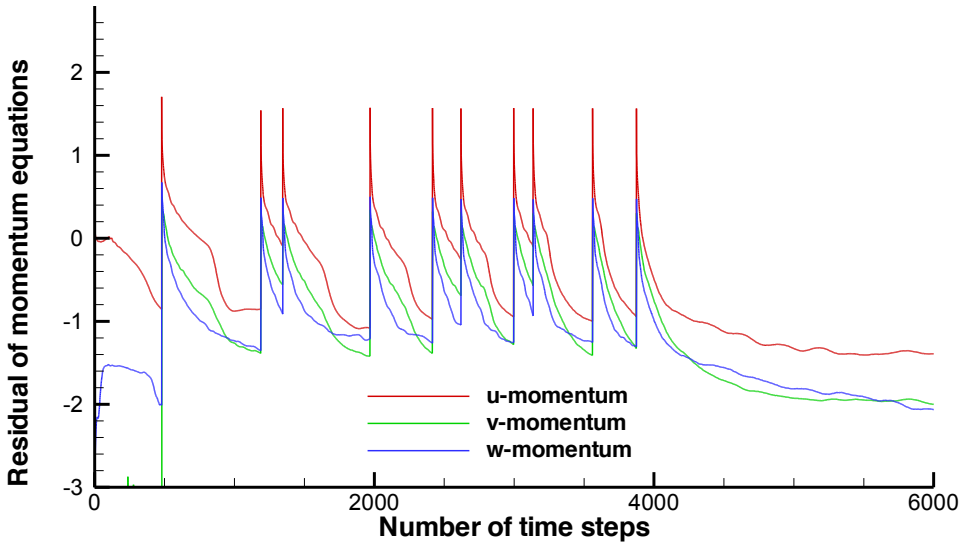


Figure 5: Convergence of the momentum equations for the *273.75°* wind direction. The appearance of peaks indicates the activation of each wind turbine column.

### 3.5 Wind speed direction variation

For the same inflow mean velocity at hub height (*8m/s*) and turbulence intensity (*7%*), the mean power deficit between wind turbines wt07 and wt17 was caclulated. For each wind direction a flow sector of *±2.5°* size was considered. Measurements refer to a 5° moving window technique. In Figure 7, it is observed that predictions significantly overestimate the mean power deficit for wind directions in the range *270°±7°* which is consistent with the comparison between predictions and measurements for different flow sector sizes.

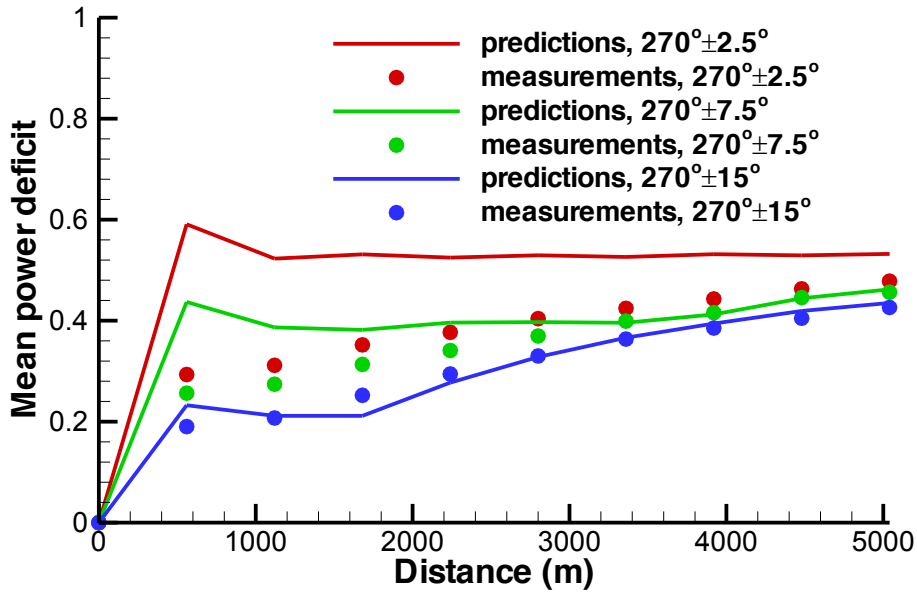


Figure 6: Mean power deficit along the rows 2 to 7, obtained by averaging the power output from wind turbines wt02 to wt97 within each row. Predictions and measurements are plotted for three different flow sectors around the *270°* wind direction. The level of turbulence intensity is *7%*.

### 3.6 Turbulence variation

For the same inflow mean velocity (*8m/s*) and a mean wind direction of *270°* (flow sector *±2.5°*), the mean power deficit along rows *2-7* was estimated. Again, there is a systematic over-prediction of the measurements for all values of the inflow turbulence intensity (Figure 8). From Figures 6-8 can be concluded that averaging of the results in a wide flow sector is needed *(±15°)* in order to have a meaningful comparison between predictions and measurements.

### 3.7 Atmospheric stratification

For the same inflow mean velocity (*8m/s*) and a mean wind direction of *270°* (flow sector *±5°*) the mean power deficit is estimated along rows *2-7* for various stratification conditions. Predictions again overestimate measurements (Figure 9). Overestimation is higher for stable conditions and decreases for unstable conditions. The trend of increasing power deficit as stratification changes from unstable to stable is reproduced by the simulations.

### 3.8 Spacing

The inflow mean velocity at hub height (*70 m*) was *8 m/s* and the inflow turbulence intensity at hub height was *7%*. The mean power deficit was estimated for different wind directions corresponding to different main spacings between wind turbine rows. The *270°* wind direction corresponds to a main spacing of *7 D*, the *221°* wind direction corresponds to a main spacing of *9.4 D* and the *312°* wind direction corresponds to a main spacing of *10.4 D*. The first one is the horizontal spacing between wind turbines, whereas the other two are the diagonal spacings. Comparison with measurements shows again an overestimation of the mean power deficit (Figure 10). The increase in power deficit with distance beyond *2000m* is not reproduced by predictions which exhibit a constant power deficit. The ongoing increase of power deficit with distance is predicted only when averaging over a wide flow sector is performed (Figure 6). It can be concluded that the estimation of the mean power deficit in large offshore wind farms should be made by averaging predictions and measurements over a wide wind speed direction sector (*±15 °*).

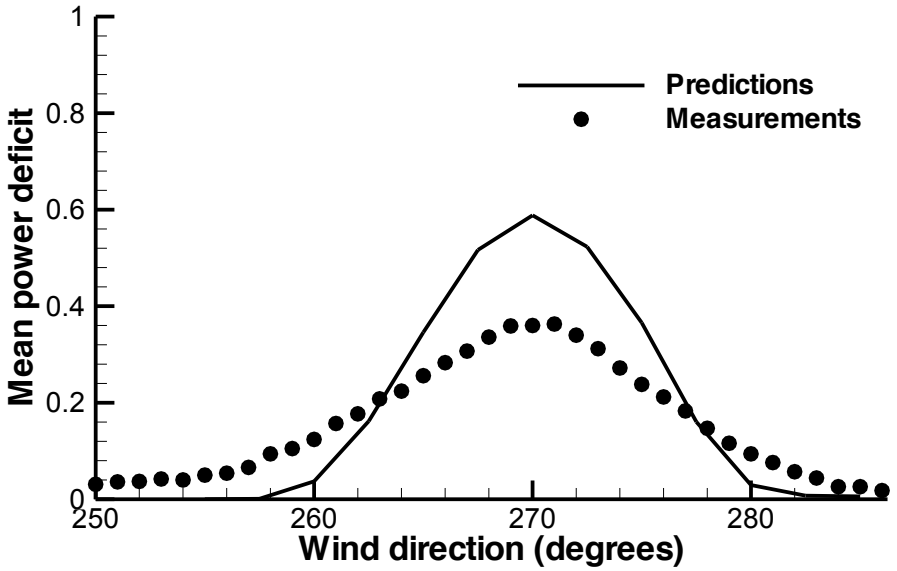


Figure 7: Mean power deficit between wind turbines wt07 and wt17 obtained by averaging the power output in sectors of ±2.5° around each wind direction. The level of turbulence intensity is 7%.

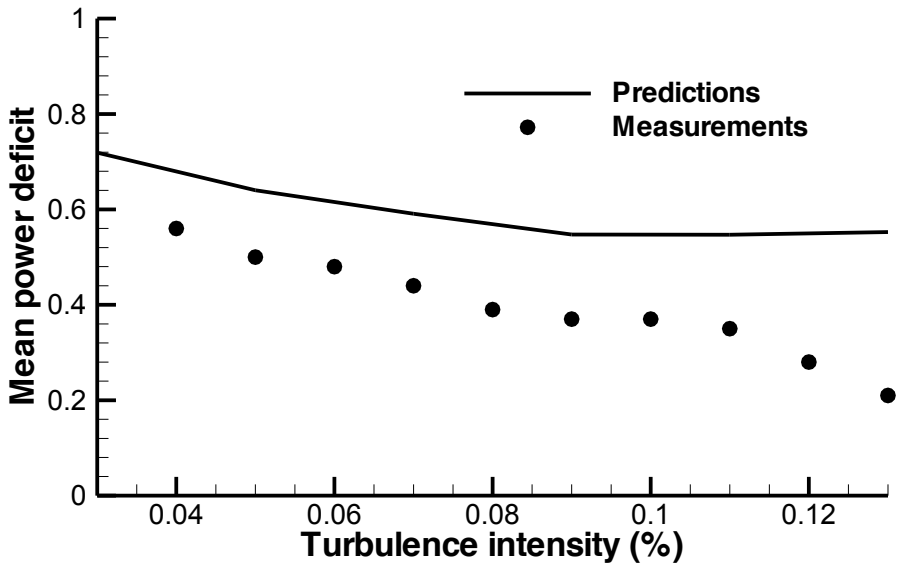


Figure 8: Maximum power deficit along the rows 2 to 7. Predictions and measurements refer to a flow sector of ±2.5° around the 270° wind direction.

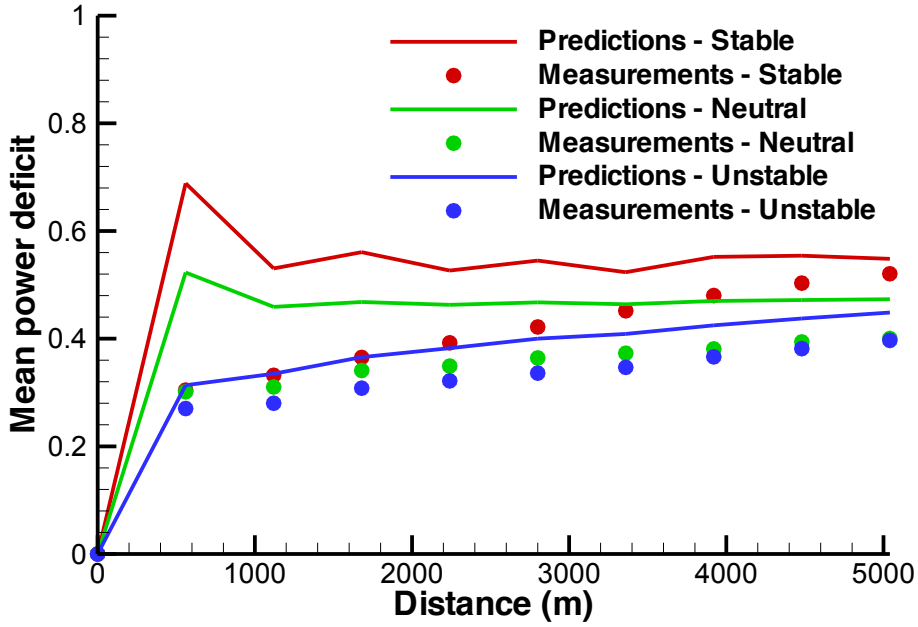


Figure 9: Mean power deficit along the rows 2 to 7 for different stratification conditions. Predictions and measurements refer to a flow sector of ±5° around the *270°* wind direction.

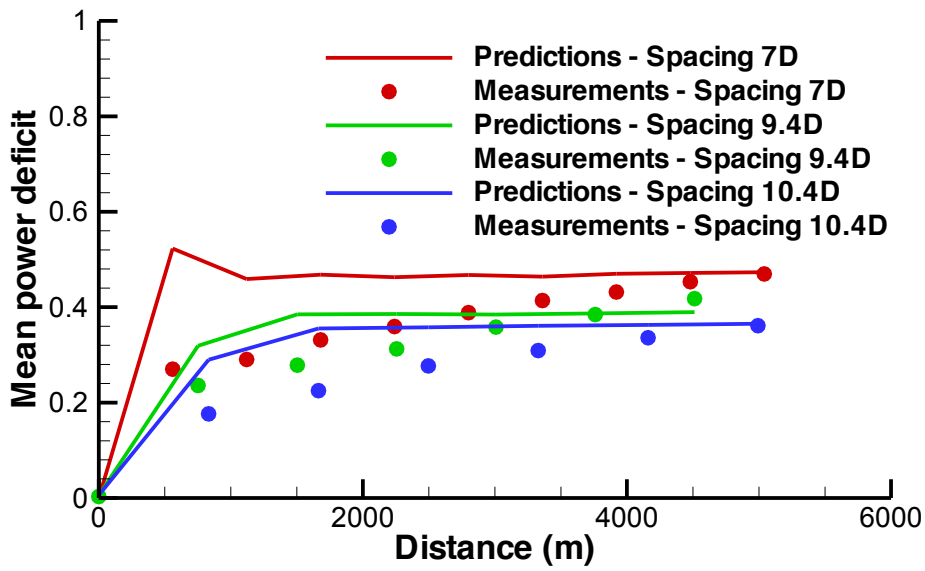


Figure 10: Mean power deficit for different spacing between the wind turbine rows. Spacing *7 D* refers to the *270°±5°* wind direction (mean value along rows *2-7*), spacing *9.4 D* refers to the *221°±5°* wind direction (mean value along the SW diagonals) and spacing *10.4 D* refers to the *312°±5°* wind direction (mean value along the NW diagonals). The level of turbulence intensity is *7%*.

### 3.9 Power polar

The objective was to determine the park power efficiency for *0 - 360°* inflow, where the efficiency is defined as the ratio between the park power and the power from 80 x one stand-alone wind turbines. The inflow mean velocity at hub height (*70 m*) was 8 m/s and the inflow turbulence intensity at hub height was *7%*. Calculations were performed with the amended GCL engineering

model [7], calibrated using the CRES-flowNS predictions for the *270°, 221°* and *312°* wind directions. In order to calibrate the engineering model, simulations were first performed for the *270°, 221°* and *312°* wind directions. For each wind direction *α,* the results of 5 simulations performed in the sector *α±2.5°,* with a step of *2.5°*, were averaged to be comparable to the CFD results.

According to the standard procedure, the velocity deficit at each wind turbine of the farm is estimated by summing up the inductions of the neighbouring turbines using the Euclidean norm as described in Section 2.2.3:

$$U_\infty - U_i = \sqrt{\sum_{j=1}^{N_T}\left[\left(U_j - u_{ij}\right)^2\right]}$$

where $N_T$ is the number of the neighbouring wind turbines where $U_j$, $U_j$ are the onset velocities of the *i-th*, *j-th* wind turbines respectively and $u_{ij}$ is the velocity induced to the *i-th* wind turbine by the wake of the *j-th* wind turbine. Using this approach, the predicted reference velocities along the wind turbine rows are shown in Figures 11-13, for the *270°, 221°* and *312°* wind directions respectively. For the *270°* wind direction, GCL results indicate a continuing increase of the velocity deficit at the downstream positions, not present in the CFD predictions. For the *221°* wind direction, GCL predicts a constant deficit along row *7.* CRES-flowNS predicts also an almost constant deficit, but at a different level. Going further inside the wind farm (row 6), GCL predicts a higher deficit level, not present in CRES-flowNS predictions. A similar comparison is observed for the *312°* wind direction.

An alternative formulation is to use maximum value of the velocity deficits at each position instead of the Euclidean norm summation. As observed in Figures 14-16 the results of the engineering model are closer to the CFD predictions for all three simulated wind directions. However, the overall representation of the wind farm is worse, as seen in Figure 17. Due to the nature of the algebraic models used it is seen that there is a concentrated drop in performance around *90°, 180°, 270°, 360°*, which is spread over a larger region in the CFD calculation. The simple approach of adopting the maximum velocity deficit seems to perform better in those wind directions, where the maximum shadowing between the wind turbines occur, but worst in the rest of wind directions. Therefore, a combined method can be adopted to calibrate the engineering model: the maximum velocity deficit approach is used for wind direction sectors centred to multiples of *45°* (works better for multiples of *90°*), whereas the Euclidean norm approach is used for the rest of wind directions. Comparison of the calibrated GCL predictions with measurements is shown in Figure 18.The size of the sectors where the maximum velocity deficit approach is implemented has been selected equal to *7.5°*, however, further investigation is needed to check if this choice is suitable for other wind farms also.

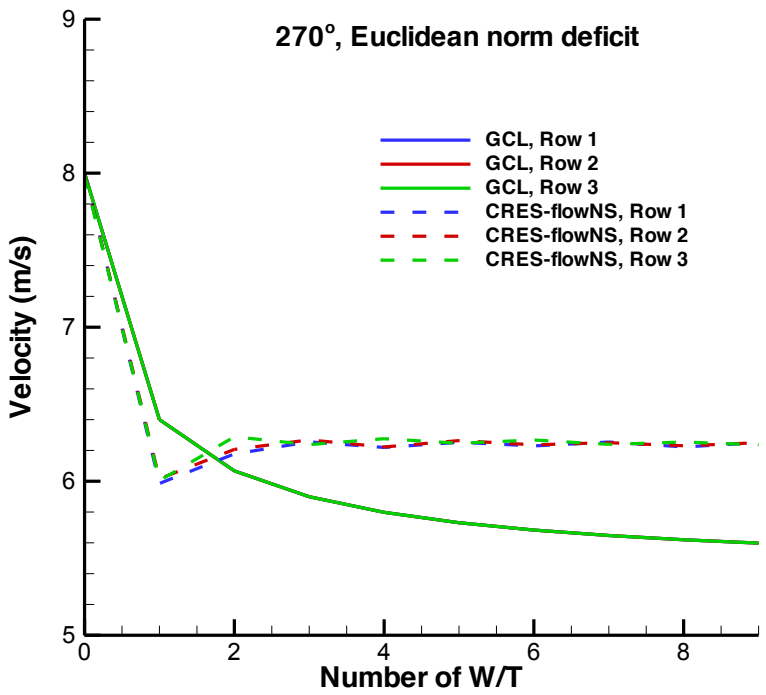


Figure 11: Comparison between CRES-flowNS and GCL predictions of the wind turbine reference velocity along rows *1-3* for the *270°* wind direction. The Euclidean norm is used to estimate the velocity deficit in GCL calculations.

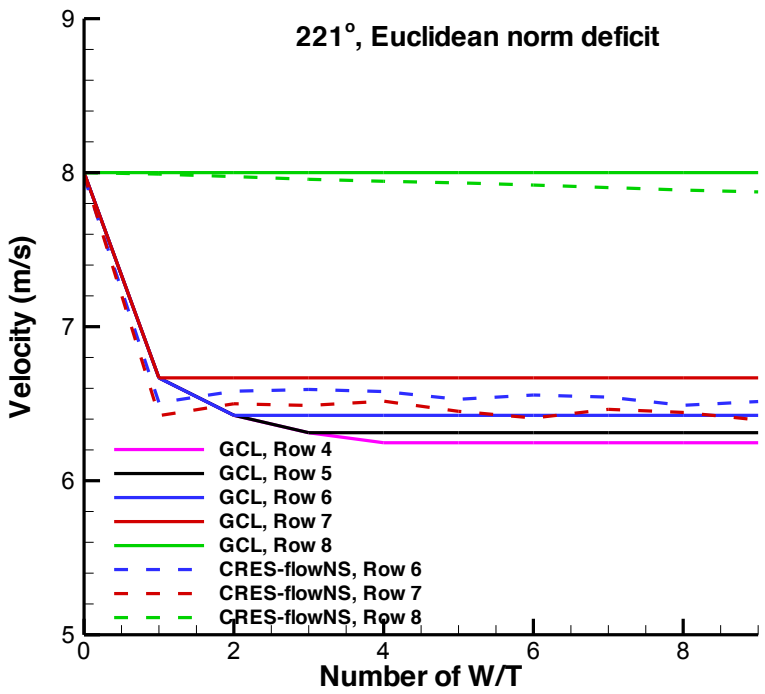


Figure 12: Comparison between CRES-flowNS and GCL predictions of the wind turbine reference velocity along rows *1-3* for the *221°* wind direction. The Euclidean norm is used to estimate the velocity deficit in GCL calculations.

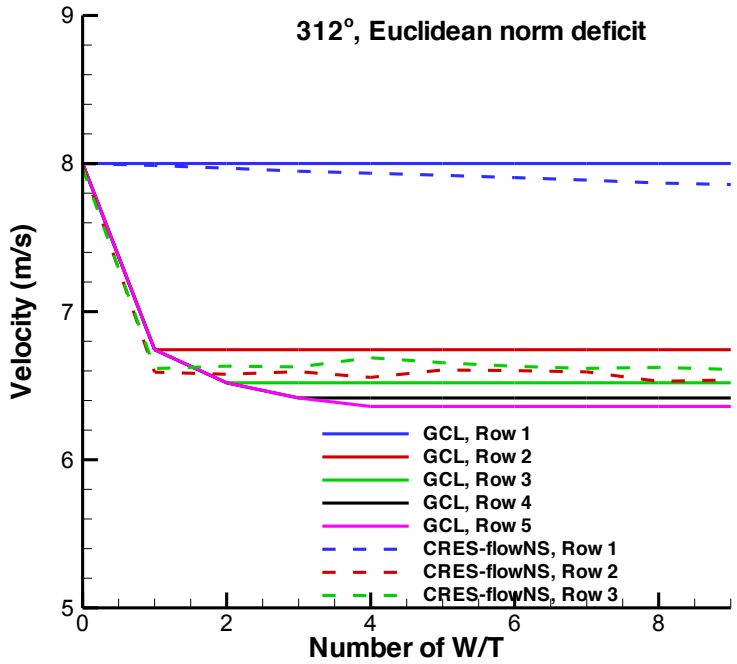


Figure 13: Comparison between CRES-flowNS and GCL predictions of the wind turbine reference velocity along rows *1-3* for the *312°* wind direction. The Euclidean norm is used to estimate the velocity deficit in GCL calculations

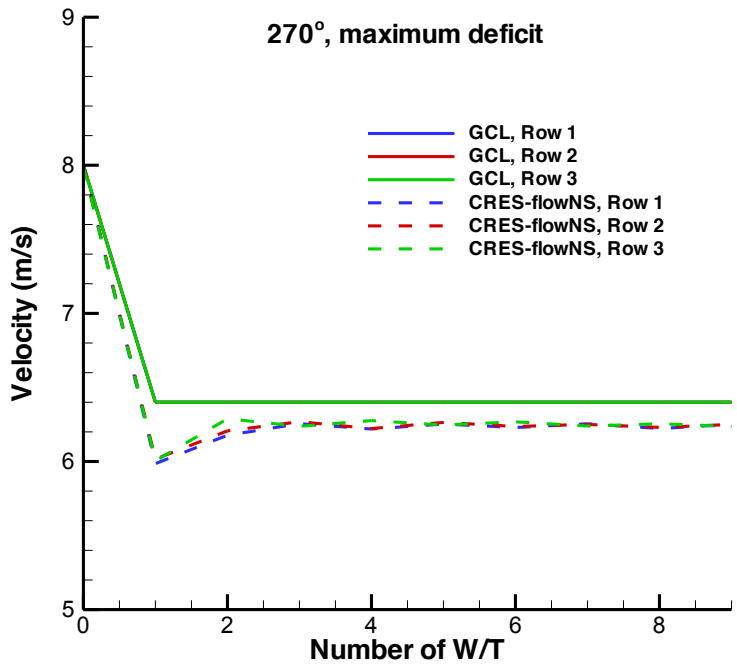


Figure 14: Comparison between CRES-flowNS and GCL predictions of the wind turbine reference velocity along rows *1-3* for the *270°* wind direction. The maximum velocity deficit at each position is used in GCL calculations.

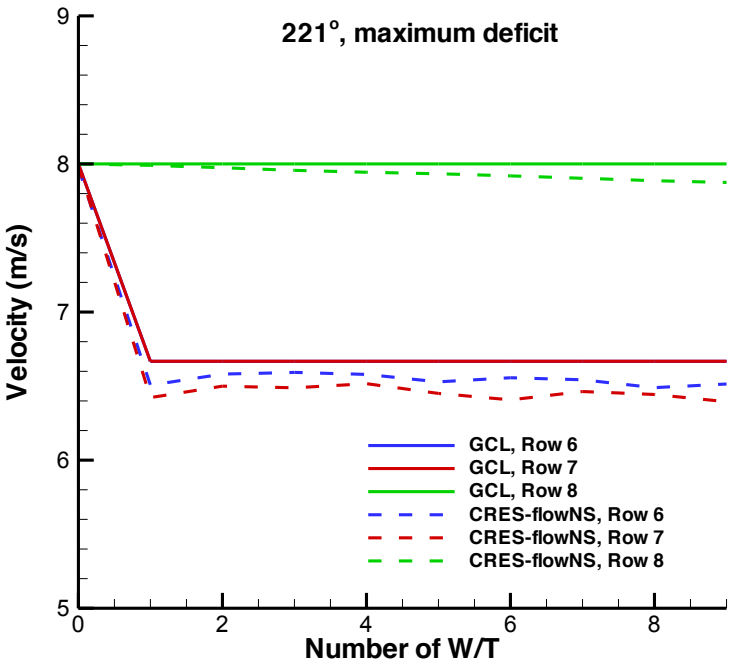


Figure 15: Comparison between CRES-flowNS and GCL predictions of the wind turbine reference velocity along rows *1-3* for the *221°* wind direction. The maximum velocity deficit at each position is used in GCL calculations

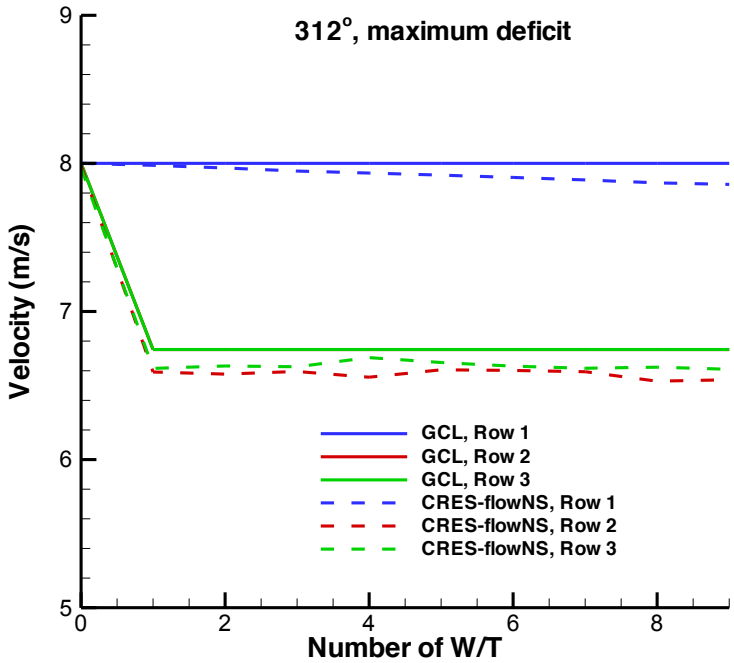


Figure 16: Comparison between CRES-flowNS and GCL predictions of the wind turbine reference velocity along rows *1-3* for the *221°* wind direction. The maximum velocity deficit at each position is used in GCL calculations

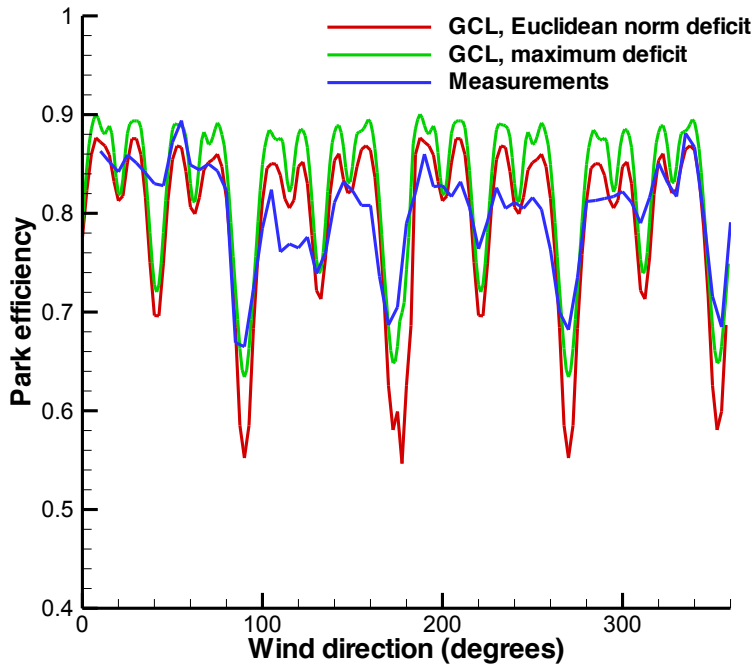


Figure 17: GCL polar predictions of park efficiency using two different approaches for the estimation of the velocity deficit at the wind turbine positions, the Euclidean norm summation and the maximum velocity deficit

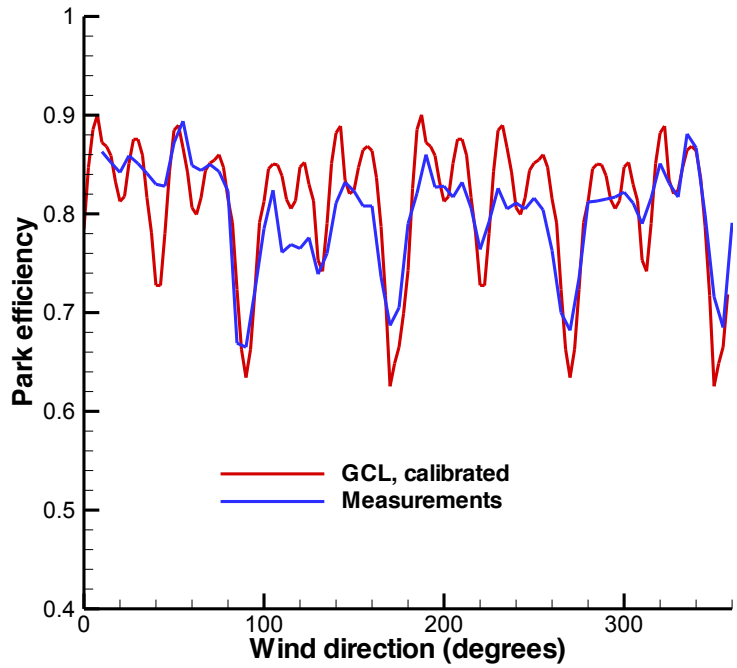


Figure 18: GCL polar predictions of park efficiency using the calibrated GCL model. The maximum velocity deficit approach is used when the maximum shadowing effect occurs, i.e, when wind direction is a multiple of *45º*.

# 4 LILLGRUND OFFSHORE WIND FARM

## 4.1 Wind farm description

The Lillgrund wind farm is located between in Øresund, 6-8 km from the swedish west coast and south of Malmö, with small water depth. The wind farm comprises 48 wind turbines arranged in 8 SW-NE rows (Figure 19). The internal spacing along the directions *180, 222 & 120°* is *4.8D, 4.3D* and *3.3D*, respectively. The layout is dominated by the triangular shape and two "missing" turbines inside the wind farm

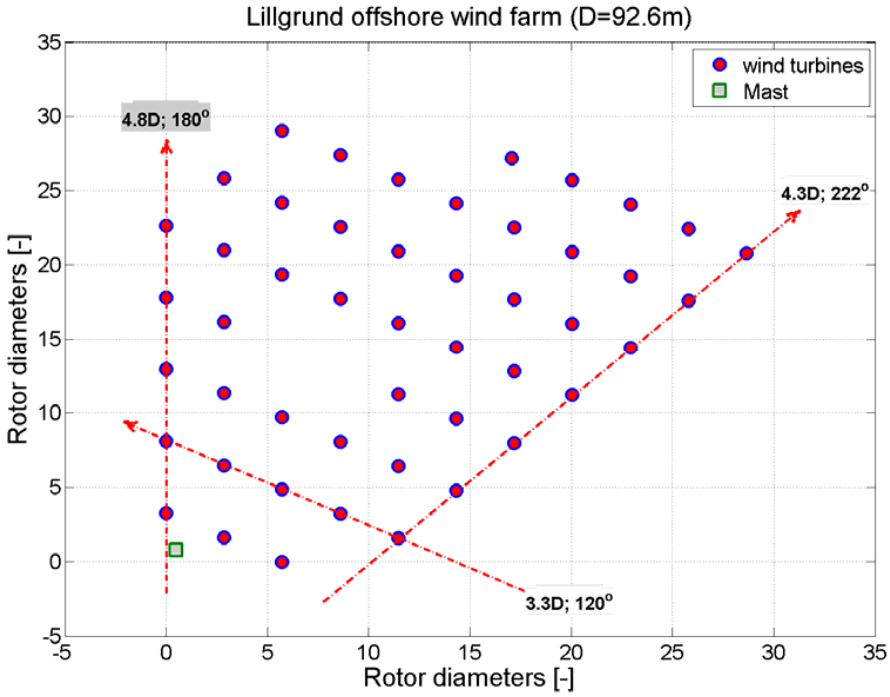


Figure 19: Layout of the Lillgrund offshore wind farm [15]

The wind turbines are SWT-2.3-93 (2.3 MW), with *92.5m* diameter and *65m* hub height, operating at variable ospeed and variable pitch. Simulations of wind turbine rotors were made using the official thrust coefficient and power curves

## 4.2 Numerical simulation

The *222±15°* and *120±15°* wind direction sectors were simulated. A procedure similar to that of the Horns Rev wind farm case was followed, considering 12 sub-sectors of *2.5°* for each one of the wind sectors and simulating the mean wind direction. However, in this case, all 48 wind turbines were included in each computational run, since there is no repetitive pattern as in the Horns Rev wind farm.

A successive refinement and coarsening of the grid lines was made in order to achieve a fine mesh close to the wind turbine positions. The minimum grid size in both *x* and *y* directions was between *0.08 D* and *0.125 D.* Again, the parabolic activation of wind turbine rows was used for the estimation of reference velocity $U_{ref}$ at the turbine positions.

## 4.3 Sector variation

The inflow mean velocity at hub height (*65 m*) was *9 m/s* and the inflow turbulence intensity at hub height was *6%*. *2x7* principal cases were defined to evaluate the influence of the flow sector. The first set of 7 cases referred to the *120±15°* sector, each case corresponding to a *2.5°* sub-sector around a mean wind direction varying from *105°* to *135°*. The power deficit was estimated

along a single row of 8 turbines, with an internal spacing of *3.3D*. The second set of 7 cases referred to the *222±15°* sector, each case corresponding to a *2.5°* sub-sector around a mean wind direction varying from *207°* to *232°*. The power deficit was estimated along a single row of 8 turbines, with an internal spacing of *4.3 D*

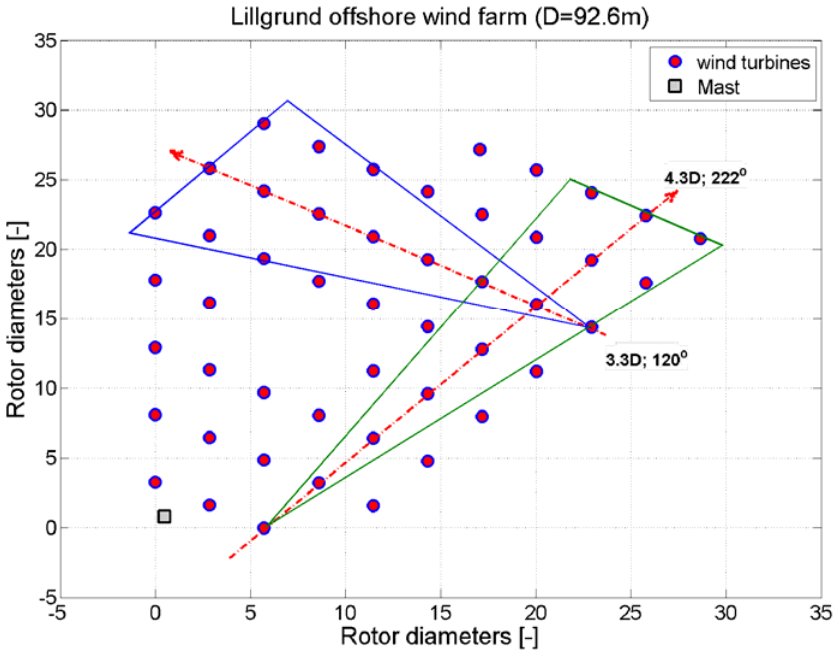


Figure 20: *30°* inflow sector along complete rows of wind turbines [15]

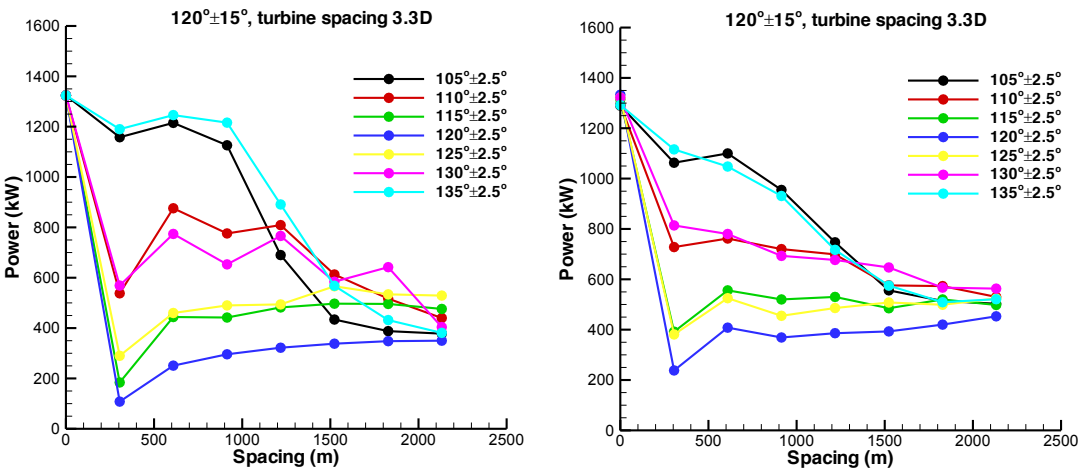


(a) (b)

Figure 21: Power variation along the complete wind turbine rows of Figure 20 for the *±2.5°* wind sub-sectors around the *120°* wind direction (*30°* wind sector, *3.3 D* internal turbine spacing) (a) Predictions and (b) Measurements

The predicted power along the complete wind turbine row marked in Figure 20 for the *120±15°* wind sector (*3.3 D* internal spacing) is shown in Figures 21-22. Figure 21 depicts the power variation for each one of the *2.5°* sub-sectors, whereas Figure 22 depicts the averaged results. CFD predictions over the *2.5°* sub-sectors show a larger variation of the power deficit in comparison to the measurements, as the wind direction changes from *105°*to *120°*. Both predictions and measurements present a nearly symmetrical behaviour around the *120°* direction, justified by the arrangement of the neighbouring wind turbines. When averaging is performed over the wider sector of *±15°*, the agreement between predictions and measurements is quite satisfactory (Figure 22), which is similar to what was found in the Horns Rev wind farm

case. The same observations can be made for the *222±15°* wind sector (Figures 23-24). Again, there is a larger variation of the predicted power deficit around the central wind direction of *222°* in comparison to the measurements, especially at the front wind turbines (Figure 23a,b). However, the agreement becomes good when averaging is performed over the wider sector of *±15°* (Figure 24).

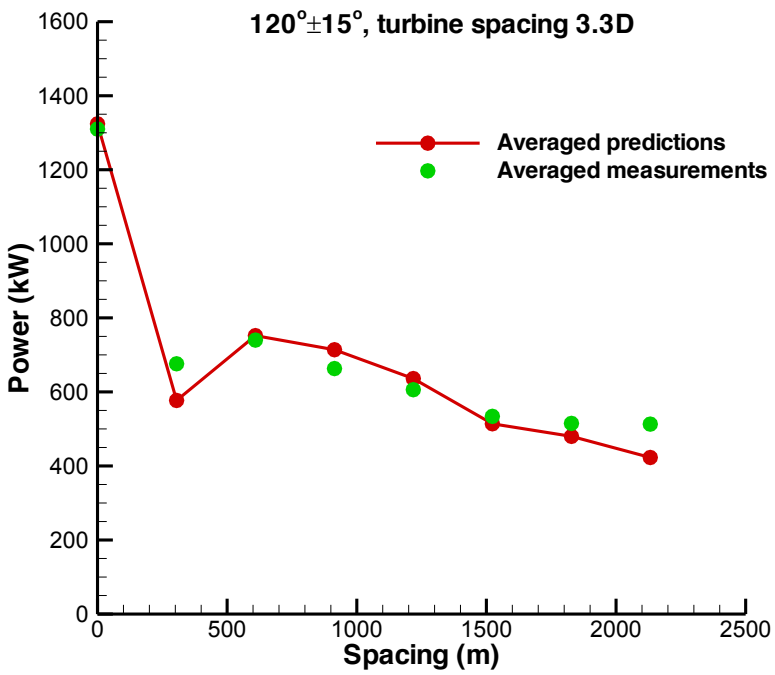


Figure 22: Average power variation along the complete wind turbine rows of Figure 20 for the *120°±15°* sector with *3.3 D* internal turbine spacing

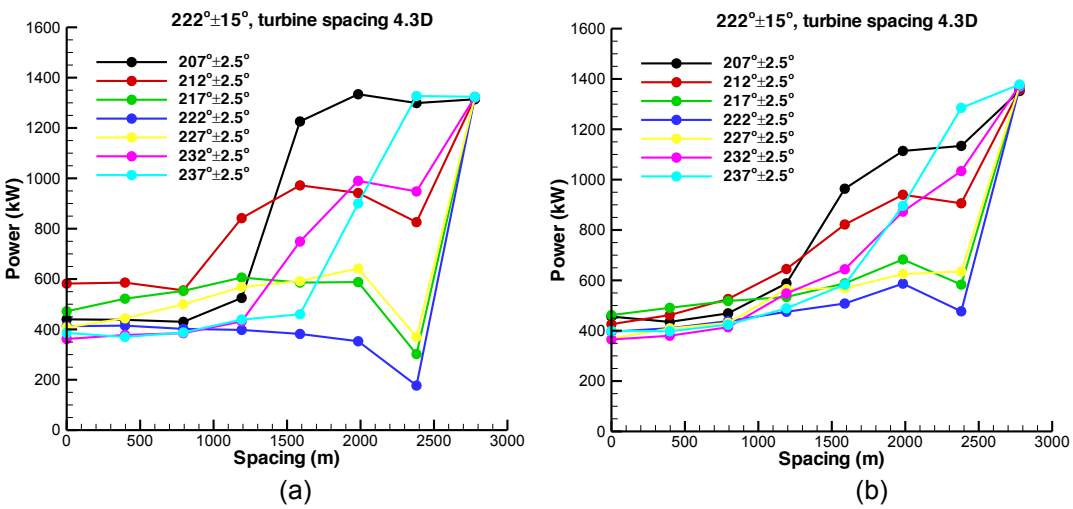


Figure 23: Power variation along the complete wind turbine rows of Figure 20 for the *±2.5°* sub-sectors around the *222°* wind direction (*30°* wind sector, with *4.3 D* internal turbine spacing (a) Predictions and (b) Measurements

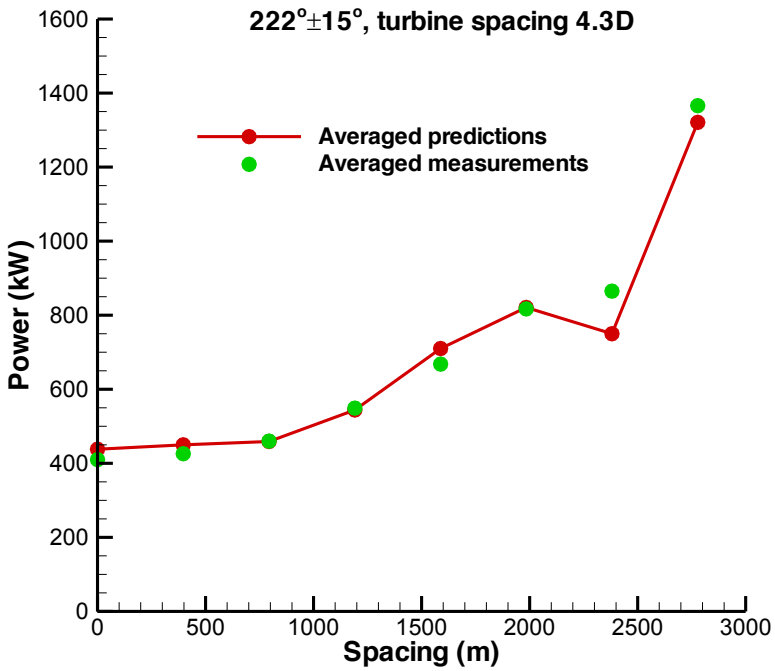


Figure 24: Average power variation along the complete wind turbine rows of Figure 20 for the *222°±15°* sector with *4.3 D* internal turbine spacing

## 4.4 Wind speed recovery

The inflow mean velocity at hub height (*65 m*) was *9 m/s* and the inflow turbulence intensity at hub height was *6%*. *2x7* principal cases were defined to evaluate the sensitivity of the model performance to the flow direction and the speed recovery. The first set of 7 cases referred to the *120±15°* sector, each case corresponding to a *2.5°* sub-sector around a mean wind direction varying from *105°* to *135°*. The power deficit was estimated along a single row of 5 wind turbines (2 turbines are missing), with an internal spacing of *3.3D* (in the region of the missing wind turbines the spacing becomes *9.9D*). The second set of cases referred to the *222±15°* sector, each case corresponding to a *2.5°* sub-sector around a mean wind direction varying from *207°* to *232°*. The power deficit was estimated along a single row of 6 turbines (1 turbine missing), with an internal spacing of *4.3 D* (in the region of the missing turbine the spacing becomes *8.6 D*).

The predicted power along the incomplete wind turbine row marked in Figure 25 for the *120±15°* wind sector (*3.3 D* internal spacing, 2 turbines missing) is shown in Figures 26-27. Figure 26 depicts the power variation for each one of the *2.5°* sub-sectors, whereas Figure 27 depicts the averaged results. CFD predictions over the *2.5°* sub-sectors again show a larger variation of the power deficit in comparison to the measurements, as the wind direction changes from *105°*to *120°*. The averaged predicted values over the *±15°* sector are close to the measurements. As expected, the effect of the 2 missing wind turbines is the significant power increase of the turbine which is located *9.9 D* behind its neighbouring upstream machine. Measurements indicate a 86.2% power increase in comparison to the complete wind turbine case, whereas predictions show a 80.6% increase. It should be noted though that this seems to be the only turbine significantly affected by the absence of the 2 turbines.

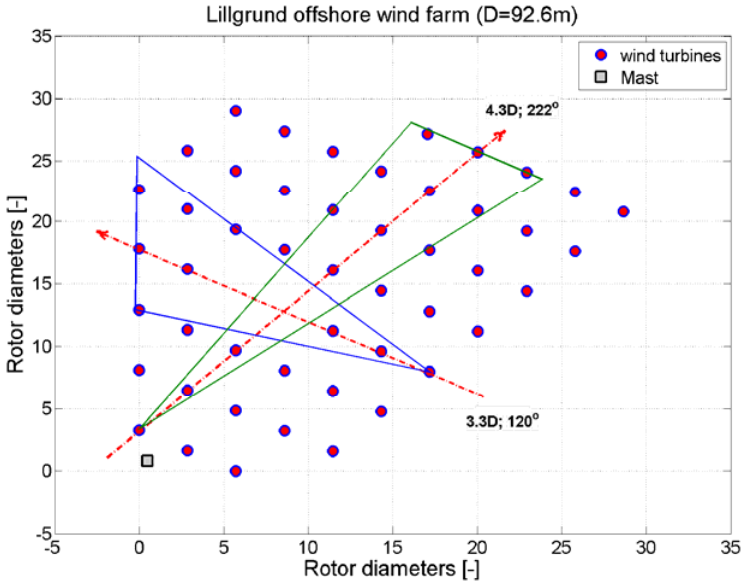


Figure 25: *30°* inflow sector along rows with missing wind turbines [15]

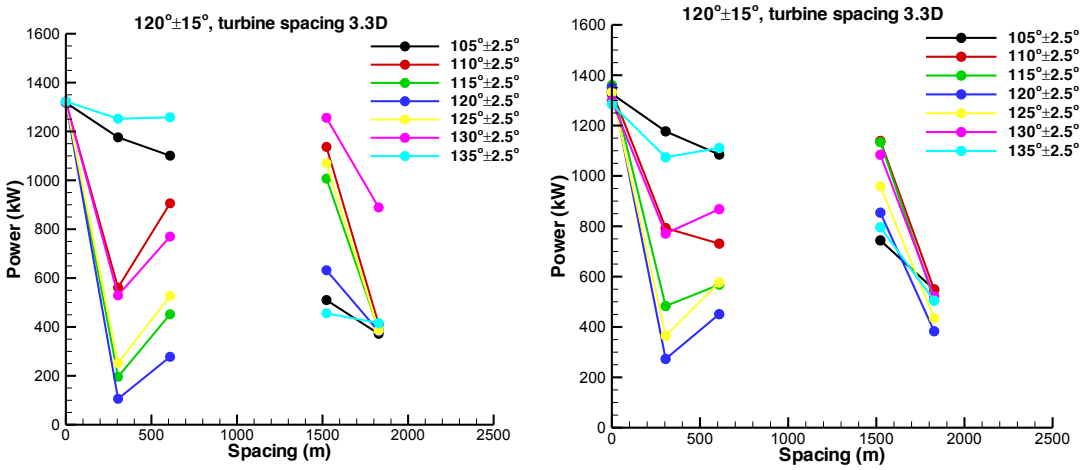


(a) (b)

Figure 26: Power variation along the incomplete wind turbine rows of Figure 25 (two missing wind turbines) for the *±2.5°* wind sub-sectors around the *120°* wind direction (*30°* wind sector, *3.3D* internal turbine spacing) (a) Predictions and (b) Measurements

Finally, the predicted power along the incomplete wind turbine row marked in Figure 25 for the *220±15°* wind sector (*4.3 D* internal spacing, 1 turbine missing) is shown in Figures 28-29. Conclusions regarding the behaviour of the predictions and the comparison against measurements remain the same. The effect of the absent wind turbine is a power increase in its downstream turbine, measured equal to 39.5% and predicted equal to 35.6%, which is less than half of the increase in the previous case (*3.3 D* internal spacing, 2 turbines missing).

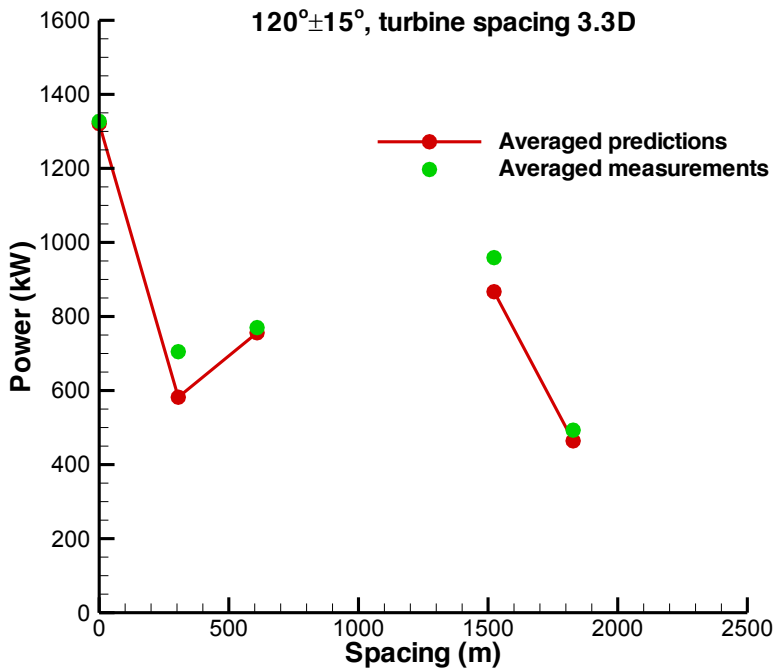


Figure 27: Average power variation along the incomplete wind turbine rows of Figure 25 (two missing wind turbines) for the *120°±15°* sector with *3.3 D* internal turbine spacing

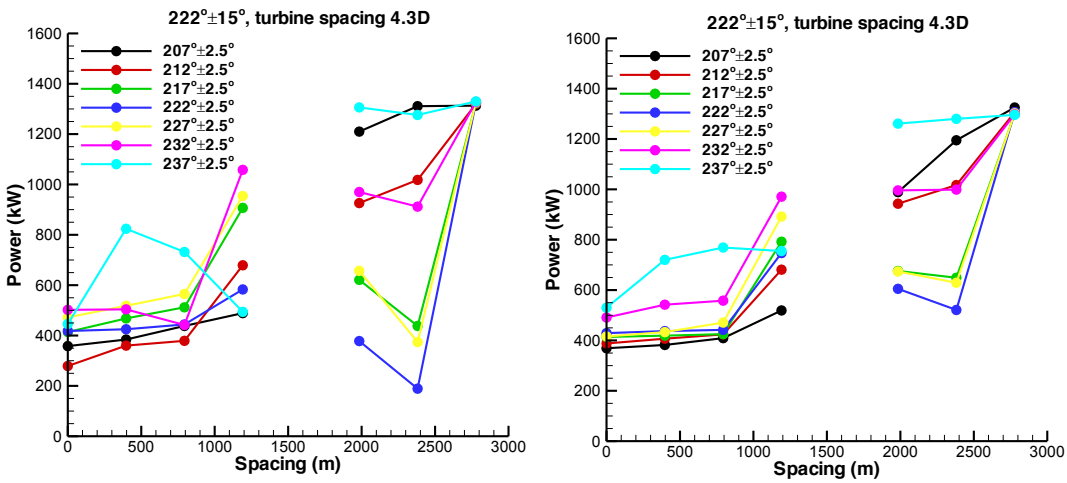


`(a) (b)

Figure 28: Power variation along the incomplete wind turbine rows of Figure 25 (one missing wind turbine) for the *±2.5°* wind sub-sectors around the *222°* wind direction (*30°* wind sector, *4.3 D* internal turbine spacing) (a) Predictions and (b) Measurements

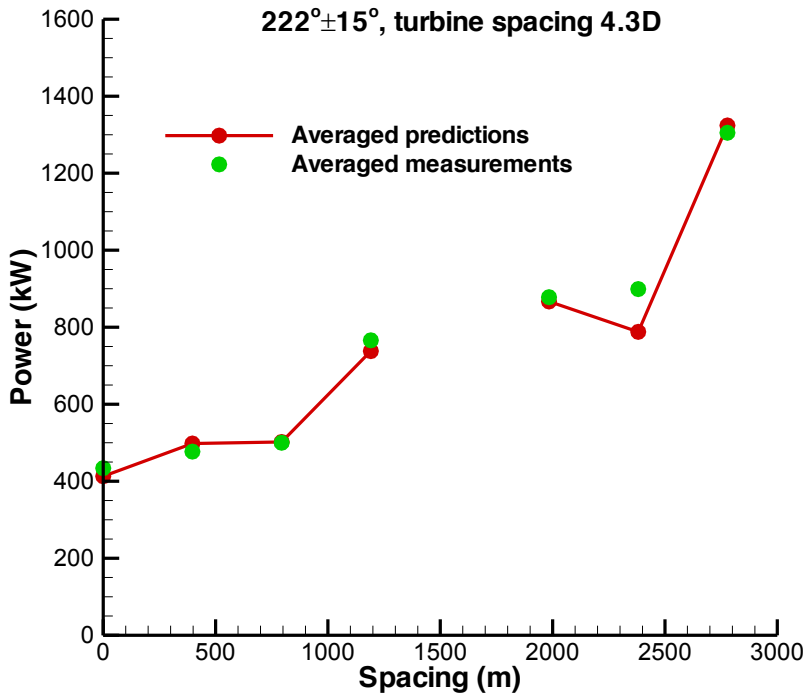


Figure 29: Average power variation along the incomplete wind turbine rows of Figure 25 (one missing wind turbine) for the *222°±15°* sector with *4.3 D* internal turbine spacing

# 5 CONCLUSIONS

A benchmark study using the CRES-flowNS wind farm model was performed. The predictions of the model were compared with experimental data sets from the Horns Rev and the Lillgrund offshore wind farms. The comparison for the Horns Rev wind farm indicated that predictions significantly overestimate the power deficit when the wind sector is narrow (*±2.5°).* As the size of the sector increases the agreement between predictions and measurements becomes better and for the wide sectors of *±15°* it can be considered quite satisfactory.

In the Horns Rev wind farm case, the systematic discrepancies between predictions and measurements for small size sectors did not allow the deduction of useful conclusions for the turbulence, spacing and stability variation, although the basic trends were captured. However, there is a possibility that part of these large differences are attributed to the uncertainty in the measurement of the wind direction. It should be further investigated if such an uncertainty produces artificially low power losses in the wake center because of direction variability.

The estimation of the park efficiency for the whole wind rose was performed using the amended GCL model calibrated with the CRES-flowNS predictions for the *270°, 221°* and *312°* wind directions. The maximum velocity deficit approach was used for wind sectors centred to multiples of *45°*, when the maximum shadowing between the wind turbines occur, whereas the Euclidean norm summation of velocity deficits was used for the rest of wind directions. The comparison with measurements was satisfactory and encouraged the prospect that the combination of fast engineering models with advanced CFD solvers can produce acceptable results reducing the computational cost.

For the Lillgrund wind farm, predictions showed a larger variation of the power deficit in comparison to the measurements, as the wind direction changes, when averaging was performed over small sub-sectors of *±2.5*. When averaging was performed over the wider sector of *±15°,* the agreement between predictions and measurements became quite satisfactory as also observed in the Horns Rev wind farm case. Both predictions and measurements predict a high power increase in the cases of incomplete wind turbine rows, but only for the single wind turbine which is located in a larger spacing due to the absence of the missing turbines. The increase in power is more than doubled in the case of two missing turbines in comparison to the case of one missing turbine.

# 6 REFERENCES

[1] Barthelmie, R.J., Hansen, K, Frandsen, S.T., Rathmann, O., Schepers, J.G., Schlez, W., Phillips, J., Rados, K., Zervos, A., Politis, E.S., and Chaviaropoulos, P.K., "Modelling and Measuring Flow and Wind Turbine Wakes in Large Wind Farms Offshore", *Wind Energy*, Vol. 12, No. 5, pp. 431-444, 2009

[2] Troen, I., Petersen, E.L., *European Wind Atlas*, Risø National Laboratory, Roskilde, Denmark, 1989:656

[3] Schepers, J.G., *ENDOW: Validation and Improvement of ECN's Wake Model*. ECN:ECN-C-03-034: Petten, The Netherlands, 2003: 113

[4] Crespo, A., Hernandez, J., Fraga, E., Andreu, C., "Experimental validation of the UPM computer code to calculate wind turbine wakes and comparison with other models", *Journal of Wind Engineering and Industrial Aerodynamics*, 1988, 27, pp. 77-88.

[5] Rados, K., Larsen, G., Barthelmie, R., Schelz, W., Lange, B., Schepers, G., Hegberg, T., Magnusson, M., "Comparison of wake models with data for offshore windfarms", *Wind Engineering*, 2002, 25, pp. 271-280

[6] Chaviaropoulos, P. K. and Douvikas, D. I., "Mean-flow-field Simulations over Complex Terrain Using a 3D Reynolds Averaged Navier–Stokes Solver," *Proceedings of ECCOMAS '98*, 1998, Vol. I, Part II, pp. 842-848

[7] Dekker, J.W.M, Pierik, J.T.G. (Editors), "European Wind Turbine Standards II", ECN-C--99-073, 1999

[8] Prospathopoulos, J.M., Politis, E.S., Rados, K.G., Chaviaropoulos, P.K., "Evaluation of the effects of turbulence model enhancements on wind turbine wake predictions", Wind Energy, 2011, 14, pp.285-300.

[9] Politis, E.S., Prospathopoulos, J.M., Cabezon, D., Hansen, K.S., Chaviaropoulos, P.K, Barthelmie,R.J., "Modeling wake effects in large wind farms in complex terrain: the problem, the methods and the issues", Wind Energy, 2012, 15, pp.161-182

[10] Prospathopoulos, J.M., Politis, E.S., Chaviaropoulos, P.K., "Modelling Wind Turbine Wakes in Complex Terrain", *Proceedings of EWEC 2008*, Brussells, Belgium, pp. 42-46

[11] Stull, R. B., "An introduction to boundary layer meteorology", ISBN 90-277-2768-6 ed. Kluwer Publications Ltd, 1988

[12] Panofsky H.A., Dutton J.A., Atmospheric Turbulence, Models and Methods for Engineering Applications, John Wiley & Sons, 1984

[13] Wilcox, D.C., (1993), Turbulence Modelling for CFD, DCW Industries Inc., La Canada, California, IBSN 0-9636051-0-0

[14] Hansen, K. "WP1.1 Wake model performance validations for Horns Rev offshore wind farm" Report: Eera-Dtoc, 2013.

[15] Hansen, K. "WP1.1 Wake model performance validations for Lillgrund offshore wind farm" Report: Eera-Dtoc, 2013.

Applied Energy 104 (2013) 834–844

Contents lists available at SciVerse ScienceDirect

Applied Energy

journal homepage: www.elsevier.com/locate/apenergy

# An overview of data for wake model evaluation in the Virtual Wakes Laboratory

R.J. Barthelmie *, S.C. Pryor

*Atmospheric Science Program, Department of Geological Sciences, Indiana University, Bloomington, IN 47405, United States*

## HIGHLIGHTS

- ▶ The Virtual Wakes Laboratory contains meteorological and wind farm data.
- ▶ Advantages and issues with different types of wind turbine wake data are given.
- ▶ Metrics for wake model evaluation are compared.
- ▶ Contributions of expansion and meandering to wake width are compared.

## ARTICLE INFO

*Article history:*
Received 6 August 2012
Received in revised form 27 November 2012
Accepted 4 December 2012
Available online 2 January 2013

*Keywords:*
Wind turbine
Wakes
Measurements
Wind farm
Modeling

## ABSTRACT

Improved prognostic models of wind turbine wakes are essential to improved design of offshore wind farms to maximized power production and minimize turbine fatigue loading. This paper describes the Virtual Wake Laboratory, an online open access resource that provides meteorological and wind farm data for use in wake characterization and wake model evaluation exercises. Specific examples of the types of analyses that can be conducted using these data are given, along with recommendations regarding appropriate metrics to be applied and considerations for wake model evaluation.

© 2012 Elsevier Ltd. All rights reserved.

## 1. Introduction

Development of offshore wind farms containing dozens to hundreds of wind turbines, means that very few turbines experience free-stream or ambient conditions and the majority have to operate in wakes from upstream turbines and thus experience complex wind and turbulence climates, leading to reduced power production and increased fatigue loading. However, it is difficult to fully optimize turbine layouts based on power output and load minimization because there are significant uncertainties in the physical understanding of wakes and thus wake characterization used in wind farm models.

Improved prognostic models of wind turbine wakes are thus an essential component of the drive towards optimizing multi-megawatt wind farm layouts to both maximize power production [1] and minimize turbine loading [2,3]. Total power output from existing large wind farms is suppressed by 5–20% due to wake losses depending on turbine spacing/placement and site climatology [4]. There is a demonstrable benefit, therefore, to be gained by improving pre-construction wake prediction and wind farm design optimization within the constraints arising from space and infrastructure (e.g. cable layouts and access roads). Although recent increases in wind farm size [5] have driven a need to understand multiple wake interactions, modeling individual wakes correctly is still a challenging issue, especially in complex terrain [6], and remains a key step towards improved understanding of wake behavior as discussed herein.

A number of field studies have been conducted to provide observational data necessary to develop improved physical understanding of the parameters that control the evolution and interactions of single or multiple wakes within small wind farms. The earliest studies used measurements from one or more meteorological masts placed in a position that will experience a direct wake from a nearby wind turbine e.g. [7,8]. In those early studies measurements were typically taken with standard cup anemometers and wind vanes deployed at more than one height. Some of the

* Corresponding author.
*E-mail addresses:* rbarthel@indiana.edu (R.J. Barthelmie), spryor@indiana.edu (S.C. Pryor).

0306-2619/$ - see front matter © 2012 Elsevier Ltd. All rights reserved.
http://dx.doi.org/10.1016/j.apenergy.2012.12.013

most well-known studies of this type include those from the Nibe turbine [9,10] and Vindeby wind farm [11,12]. In addition to meteorological wind speed/turbulence measurements, some studies included higher time resolution measurements with sonic anemometers such as those at Nørrkær Enge [13] and for larger turbines at the ECN test farm [14]. Further studies included instrumentation of turbines with strain gauges to measure forces on the blades and/or tower resulting from wakes e.g. [10,15]. More recent measurement campaigns have deployed sodar placed at different distances from the turbine both on-land [8] and offshore [16]. Understanding of the integrated effects of total wind farm wakes resulting from larger wind farms has used both meteorological masts deployed at large downwind distances [17] and remote sensing instrumentation deployed on satellite platforms [18,19], but probably the most significant advance in terms of the evolution of measurement technologies is application of lidar for both single turbine wake [20] and wind farm characterization [21]. The need to develop observations of whole wind farm effects on downstream flow has prompted use of a range of innovative remote sensing measurement approaches including satellite borne radiometers [22], radars [23] and lidar [24].

During the 1980s a number of wake models were developed and evaluated, mostly for small numbers of turbines [25], and most current generation wind farm wake models still leverage that work (see the review by Crespo et al. [26]). An array of models are currently available, including those that start by treating each wake with relatively simple analytical approaches (e.g. WAsP [27]) where the initial wake velocity deficit is calculated as a function of the turbine thrust coefficient, and wake expansion at downwind distances is described using a coefficient which is a function of the roughness/turbulence regime. More complex models such as the eddy viscosity wake model (e.g. [28]) are based on numerical solutions to Navier–Stokes equations applied with assumptions regarding an axisymmetric velocity deficit and disregarding pressure variations. This latter constraint means these models do not treat the near-wake but are applicable to wake development from a distance of about three wake diameters downstream from the rotor. This approach has been incorporated into a range of wind farm models including Windfarmer [29] and FlaP [30]. A less parameterized model [31] was shown to give good agreement with observations in the far wake and was used as the basis for WAKEFARM [32]. Computational fluid dynamics (CFD) models have more recently been applied to simulation of wake case studies in detail [33–40] including wake simulations using large eddy simulation (LES) for both single [41] and multiple wakes [42,43].

Most prognostic wind farm models for power production forecasting from large wind farms with many turbines (up to hundreds) utilize approaches that were developed for single wakes and then rely on fairly simple methods for combining multiple wakes, with or without parameterizations for unresolved interactions (e.g. WAsP does not account for turbine-added turbulence in wakes). These include 'the sum of squares' approach used in the WAsP model [44] that calculates the combined velocity deficit in merging turbine wakes as the square root of sum of the velocity deficits squared. Windfarmer uses a modified 'nearest neighbor' approach where the velocity deficit and wake width is determined by the nearest wind turbine in the direction of the flow. There is an additional optional correction for large offshore wind farms based on reduced wind speed over the area of the wind farm from applying additional roughness elements [29]. Some models are intended to incorporate physical interactions between wakes and the atmospheric boundary layer in a pseudo-explicit manner [45,46] accounting for the change of wake expansion in different regimes of the wind farm while others use empirical corrections for larger wind farms based on limited available data. The current state of the art with respect to the application of CFD to entire wind farms in wake studies [47] may require simplifying assumptions such as homogeneity in flow conditions across the wind farm [48], and thus neglect wind speed gradients across the wind farm [49].

A universal issue in wake modeling is access to wind farm or other relevant observational data sets for model evaluation and development. Some authors argue that data from wind tunnel experiments are the most appropriate for evaluation of near-wake models [50]. Wind tunnel experiments offer the ability to provide a highly controlled environment, and greater flexibility in terms of the position of both upstream and in-wake observations, particularly at very high frequency [51]. However, at least some of the limitations of field measurements can be overcome by the use of scanning and nacelle-based lidar [52,53]. Furthermore, some early studies illustrated that even single operating turbines introduce properties in the wake flow that are difficult to represent at the correct scales in wind tunnel data. These include turbulence added by the wind turbine [54] and stratification related to the vertical temperature gradient both of which impact wake development [8]. Given current interest is focused on large wind farms with multiple wakes that likely impact both the overlying and downwind atmosphere over distances at least twice the length of the wind farm [13,19,55], wind tunnel studies with their inherent scale limitations are likely less valid than studies using ambient data. Even given the inherent variability issues of field-based data and the difficulties of both making measurements in wind farms and/or accessing and using wind farm data, they are still required. Access to, and analysis of, high-quality ambient in situ data from operational wind farms remains central to efforts to improve both understanding of the meteorological variables that determine wind turbine wakes and physical descriptions thereof, and evaluation of wind farm (and specifically) wind turbine wake models. This paper focuses on in situ field data available from the free and open access Virtual Wakes Laboratory (VWL) hosted by Indiana University (http://mypage.iu.edu/~rbarthel/Welcome.pdf). To gain access to the site potential users are required to register but thereafter access to all data is provided freely.

The structure of this paper is as follows. In Section 2 the types of data included in the VWL are documented, their advantages and disadvantages are described and examples of their use for wake characterization are provided. In Section 3, issues and challenges pertaining to wind farm wake model evaluation are described and a variety of model skill metrics are presented which can be applied to improve detailed evaluation of models not only in a statistical sense but also in terms of a process-level perspective. This is necessary in order to transition from characterizing average wake losses to modeling of wake dynamics in specific events. Example criteria used for model evaluation of single wakes are given, and additional approaches for multiple wakes assessment are described. In Section 4 concluding remarks are provided.

## 2. Data types available in the Virtual Wakes Laboratory (VWL)

Table 1 shows the data currently (2012) contained with the VWL. These data and the types of analyses they are best suited to are described below.

### 2.1. SCADA data

Supervisory Control and Data Acquisition (SCADA) systems are used to collect a range of data from each individual wind turbine deployed in operational wind farms. These data are time synchronized and, in the context of using them for wake analysis, typically include key parameters such as; power production, wind speed from the nacelle mounted anemometer, turbine yaw angle, and a turbine status signal. SCADA data are particularly useful because

**Table 1**
Overview of data in the Virtual Wakes Laboratory.

| Site name | Data period | Brief description | Source |
|---|---|---|---|
| Horns Rev | Statistics from 2004 | Mean power output for all turbines for selected wind speeds and wind directions | Upwind project<br>Data credit to DONG Energy and Vattenfall |
| Middelgrunden 1 | 2001–2002 | 10 min averaged power, wind speed and yaw angle at all wind turbines for entire period | Data credit to Middelgrundens Vindmøllelaug |
| Middelgrunden 2 | 2001–2004 | Time series of 10 min values of multiple variables for each wind turbine | Data credit to Middelgrundens Vindmøllelaug |
| Nysted | Statistics from 2004 to 2006 | Mean power output for all turbines for selected wind speeds and wind directions | Upwind project<br>Data credit to DONG Energy and Vattenfall |
| Vindeby 1 | 1993–1996 | 30 min average time series of multiple variables from 3 meteorological masts and power from 2 turbines for entire period | Funded by SEAS, operated by Risø National Laboratory.<br>Data credit to DONG Energy, Vattenfall and DTU Wind |
| Vindeby 2 | 1996–2004 | 30 min average time series of multiple variables from 2 meteorological masts and limited turbine power output | Funded by SEAS, operated by Risø National Laboratory.<br>Data credit to DONG Energy, Vattenfall and DTU Wind |
| Vindeby 3 | 2001 | Case studies of wake measurements by sodar at Vindeby | ENDOW project<br>Operated by Risø National Laboratory.<br>Data credit to DTU Wind |

they are continuous through time and are present for every turbine location in an array. These data (that are typically made available with 10 min averaging periods) can therefore provide a degree of spatial information in wind farms that is very difficult to obtain from other methods, except perhaps scanning lidar [21], and provide a unique opportunity to assess wind farm performance over time. Apart from obvious issues regarding data confidentiality, the primary drawbacks of analyzing SCADA data for wake studies relate to the size of the databases that usually require extensive pre-processing, and the time averaging that is typically applied to the data prior to public release. Nevertheless, SCADA data are a direct representation of turbine operation and power production.

A number of SCADA data sets are available in the Virtual Wakes Laboratory (see Table 1) including data for 2001–2004 inclusive from Middelgrunden wind farm in Denmark [56]. The wind farm has a particularly interesting design with 20 turbines laid out in an arc, with turbine to turbine spacing along the arc of 2.4 rotor diameters ($D$) (see Fig. 1). Data from this site are thus extremely useful for conditional sampling based on wind direction to select whether the turbines are operating in 'no wake', single wake, partial wake, or multiple wake conditions. As shown in Fig. 1, the mean power output at each turbine is strongly determined by both its position in this wind farm and by the wind direction, which dictate whether individual wind turbines are operating in wake conditions. A key issue in analysis of wind turbine SCADA data for wake characterization and wake model evaluation pertains to whether it is preferable to use output from the anemometer mounted on the nacelle to represent the inflow wind speed, or whether it is better to derive the inflow wind speed from the turbine power production data and the turbine power curve [57]. Use of the power curve for a given turbine and power production data to calculate the wind speed introduces a level of uncertainty since typically only the manufacturer's power curve will be available rather than an individual onsite measured power curve and there may be discrepancies arising from the onsite conditions. However, the power output from a turbine represents an integrated wind signal across the area of the rotor rather than at one location just above the nacelle [53]. As has been reported by many studies, the flow around the nacelle is extremely complex and reported errors in wind speed are both large [58] and dependent on both wind speed and power output [59]. However, a study on an Australian wind farm found that "nacelle-based wind speed observations are more accurate than the on-site met mast wind speed observations" [57]. Fig. 2 shows an example of the discrepancy in derived freestream inflow wind speed from the nacelle-mounted anemometer and the power production data using SCADA data from the VWL for Middelgrunden data. Wind speeds are derived from a polynomial fit to the manufacturer's power curve between 4 and 15 m s$^{-1}$ using the power output from turbine 1 (see Fig. 1 for a site map) and selecting only conditions when it was operating in freestream conditions. The correlation coefficient between the wind speed from the nacelle anemometer and the wind speed derived from the power curve is greater than 0.985. However, on average the power curve derived wind speeds are 3% higher than those measured by the nacelle anemometer, and the root mean squared difference (i.e. a measure of the dispersion of the data cloud) is 0.48 m s$^{-1}$ (relative to a mean wind speed of 8.1 m s$^{-1}$), which implies the selection of the power production or nacelle anemometer can have a substantial impact on the implied inflow wind speed for any given 10 min period. The discrepancies illustrated in Fig. 2 may reflect physical causes (e.g. flow around the nacelle), integration of the flow field across the rotor diameter in determining power production (vs. a point measurement), discrepancies in the power curve (relative to the manufacturers power curve), or instrument bias/uncertainty.

### 2.2. Meteorological masts

Until relatively recently mast-based instrumentation was the only viable method of obtaining meteorological measurements from wind farms [8,60]. Use of data from instrumented meteorological masts for wake studies also has a number of advantages and disadvantages. The disadvantages derive principally from three sources; (i) the meteorological masts are in fixed positions and thus a truly 3-dimensional depiction of flow within the farm and its variation over time cannot be produced, (ii) data quality is a strong function of the quality of instruments deployed and maintenance there-of, in addition to the suitability of the mast structure and instrument booms [61] and (iii) the cost of installation of tall masts increases non-linearly with height, thus as turbine hub-heights have increased measurements from masts do not always extend across the rotor plane. Nevertheless, many prospective wind farm installation locations are equipped with meteorological masts for site characterization activities. Presuming those masts are maintained post-construction, and have at least one free-stream sector remaining after the wind farm is built, the

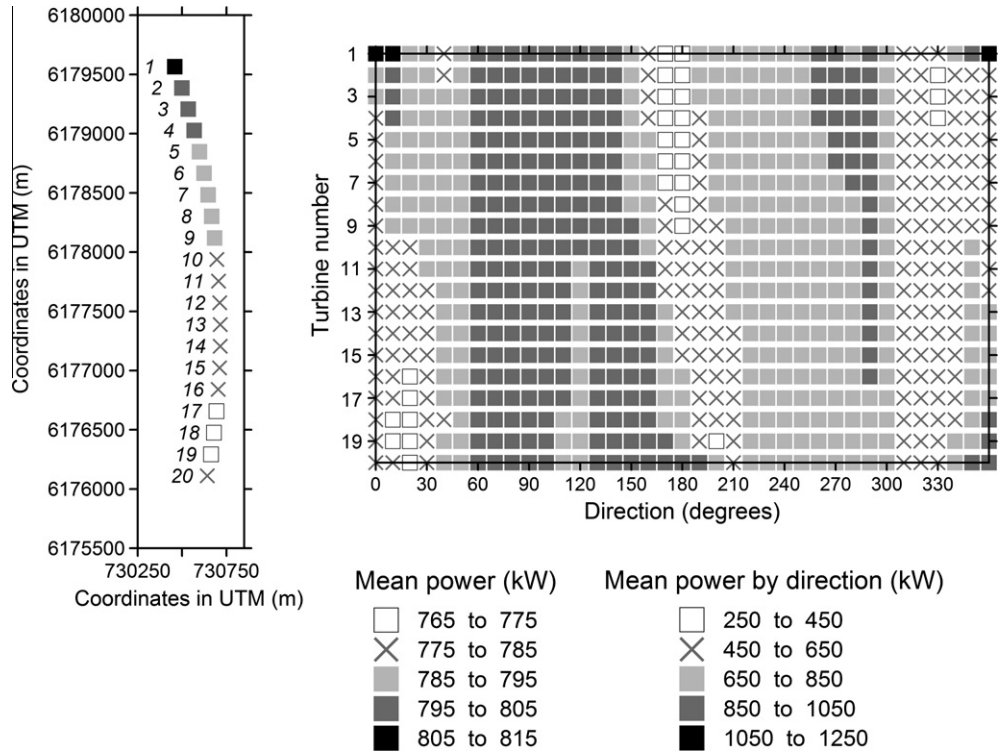


**Fig. 1.** Schematic of the layout of the Middelgrunden wind farm and mean power produced by each turbine for 2001–2004 (left) and mean total power produced at each turbine as a function of incident wind direction (right).

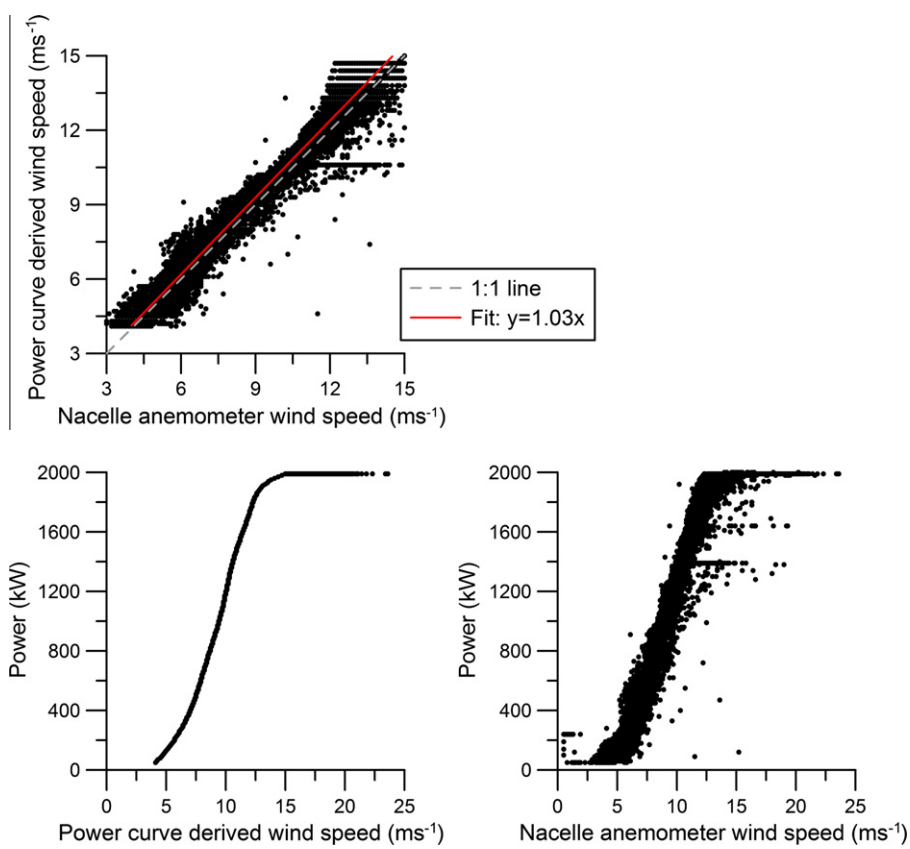


**Fig. 2.** Top. Comparison of wind speeds derived from the manufactures power curve ($U_p$) and from the nacelle anemometer ($U_a$) from turbine 1 at Middelgrunden based on data from 2001 to 2004. The red line is the best fit where $U_p = U_a * 1.03$, the gray dashed line is the 1:1 line. Bottom left: Power output plotted against $U_p$. Bottom right: Power output plotted against $U_a$.

resulting data can be analyzed to assess wind farm performance over time, and used in wake studies, although obviously this depends on the position of the mast in relation to the wind turbines/wind farm [62]. Meteorological masts have some advantages in wake studies in that masts can be instrumented at many heights and, if carefully installed and maintained they can provide a long-term record that includes vertical profiles of wind speed, turbulence and temperature.

Data from high-grade meteorological instrumentation deployed on meteorological masts in offshore wind farms are also provided in the VWL. For example, data from three meteorological masts installed close to the Vindeby wind farm in Denmark (see Fig. 3) are available from the VWL continuously for 1993–2002 with only one major change in 1996 when one of the offshore masts was closed (mast SMS in Fig. 3) and some of the measurement heights were changed. Selection of meteorological mast type and instrumentation, in addition to the placement of the meteorological masts at Vindeby was carefully chosen to augment wake studies. The mast located southwest of the turbines (mast SMW) was placed in the position of a third row giving measurement of two direct double wakes, while the mast located south of the turbines (mast SMS) was placed in the sixth position of the first row giving a single direct wake and a multiple wake with five turbines (see Fig. 3). A further mast was located on the coastline 1.5 km to the south of the wind farm (mast LM in Fig. 3). This data set has been extensively analyzed [11,12,63] and used for model evaluation [64], and remains the longest publically available time series of wake measurements. One issue with this (and other) datasets is that turbine power production data were not collected concurrently with that from instruments deployed on the meteorological mast, thus careful time synchronization between meteorological and SCADA data must be carried out. However, availability of such long data sets facilitates a wide array of statistical analyses and options for conditional sampling to resolve the physical processes controlling wind turbine wake behavior [64]. For example, Fig. 4 shows the average ratio of wind speeds as measured by mast-mounted anemometers at hub-height (38 m) for mast SMS to those at mast LM. The presence of the coastline leads to quite complex flows across the wind farm and spatial gradients of wind speed at Vindeby. This is evident from the high ratios of wind speed associated with wind directions from the east and the south–southwest, when the mast SMS has a relatively long offshore fetch, but flow to mast LM is over land. However, the presence and magnitude of the wind turbine wakes are also clearly evident as the minima in the wind speed ratios associated with wind directions when the mast LM was experiencing free-stream (undisturbed) flow and the mast SMS was in the wake of the wind farm. For example, the mast SMS is clearly impinged upon by a single wake (i.e. a wake deriving from only one upstream turbine) for wind directions of about 22°. That is, for this wind direction, data from the mast SMS indicate lower wind speeds and higher turbulence (as manifest as increased standard deviation of the wind direction) relative to the mast LM. Conditions in a multiple wake condition are evident at the mast SMS for wind directions ~320°.

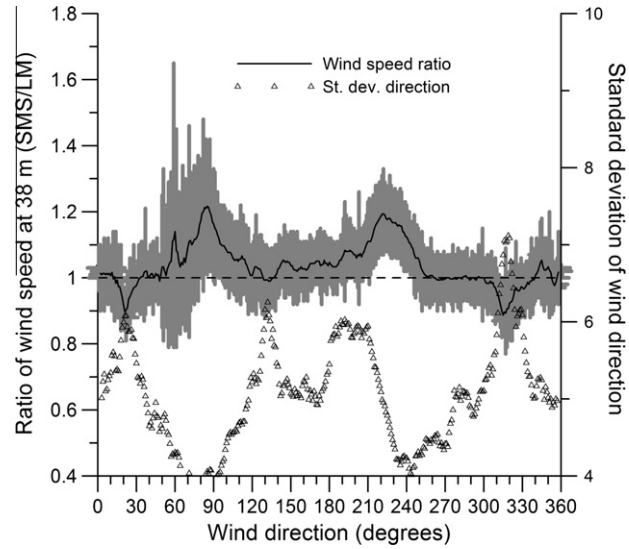


**Fig. 4.** Ratio of the wind speed at 38 m (i.e. hub-height) at the mast SMS relative to the mast LM for the Vindeby wind farm as a function of wind direction. The locations of the mast are as shown in Fig. 3. The solid black lines show the mean ratio in each 1° wind direction bin as a running average. The gray shading shows the standard deviation of the ratio around the mean. Also shown is the mean standard deviation of the wind direction (black triangles).

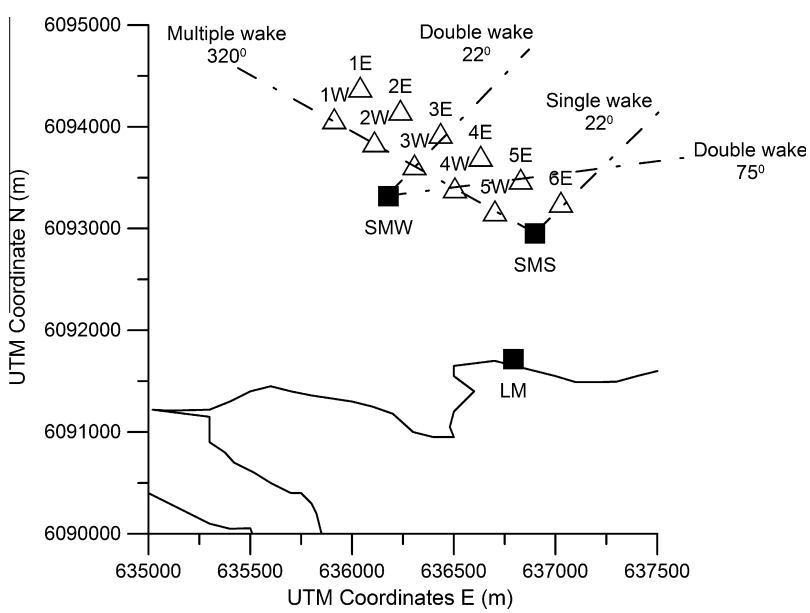


**Fig. 3.** Schematic of the layout of the Vindeby wind farm (turbine locations shown by triangles) and meteorological masts (solid squares). Distance between the turbines in each row is 300 m (8.6 *D*) and the distance between the two rows is also 300 m. Also shown are the wind directions associated with direct single, double and multiple wake measurements at the masts.

### 2.3. Remote sensing data

The obvious advantages of moving from in situ instrumentation to ground-based remote sensing for quantifying characteristics of wind turbine wakes are that (i) measurements can be made to turbine height and beyond and (ii) lidar and sodar are more mobile than traditional masts and thus can be deployed at specific downwind distances from turbines. The disadvantages largely derive from the much larger power demands for operation of the systems (relative to standard meteorological equipment), the challenges in analysis of the resulting large and complex data sets, the precision and accuracy of the measurements and difficulties in mounting these instruments on moving platforms (e.g. ships) for offshore measurements. Nevertheless, a boat-mounted sodar was able to capture and quantify wind turbine wakes at the Vindeby wind farm [16,65]. The experimental design of this campaign included a series of prescribed measurements in which during a period of forecast wind speed stationarity, a turbine(s) was selectively halted and the sodar was deployed to measure 'freestream' conditions, and then restarted so the sodar could measure the wake at an identical location.

Data are presented in the Virtual Wake Laboratory for a number of sodar experiments conducted at the Vindeby wind farm. During these experiments the sodar was operated on a ship moored at distances between 1.4 and 7.1 rotor diameters ($D$) from the wind turbines [16]. The resulting data can be used to calculate the velocity deficit profile with unprecedented vertical detail. For the case shown in Fig. 5 the sodar was deployed at a downwind distance of 2.8 $D$. In this case the near-wake classic 'double bell' shape is clearly visible with maximum relative velocity behind the turbine close to hub-height (38 m) and wake expansion to just over 50 m diameter ($D_w$) from the initial turbine diameter ($D_0$) of 35.5 m.

Following the equation given by Jensen [44] (and used in the WAsP program) the wake diameter $D_W$ at any distance downstream of a turbine comprises the initial rotor diameter $D_0$ plus expansion $D_E$ [27]:

$$D_w = D_0 + D_E \tag{1}$$

where $D_E$ is given in WAsP by:

$$D_E = 2kX \tag{2}$$

where $k$ is the wake expansion coefficient (0.05 is suggested for offshore [66]) and $X$ is the distance downstream from the turbine.

Following equation [2] the wake expansion coefficient ($k$) for the example shown in Fig. 5 is calculated to be 0.07, which is higher than the value suggested for offshore of 0.04–0.05 [66] that is likely due to slightly higher turbulence intensity at Vindeby due to its proximity to the coast.

Since predicting loads in wakes is also of interest, a tremendous advantage of remote sensing techniques is that they are also able to quantify the profiles of turbulence intensity. Fig. 5 shows profiles of turbulence intensity (calculated here as the standard deviation of the measured horizontal wind speed divided by the wind speed at the same height) from the sodar measurements at Vindeby for this case study. Measurements of ambient turbulence intensity profiles for typical turbine hub- and tip heights generally indicate decreasing values with height (Fig. 5) due to increasing wind speed with height and the decreasing impact of surface roughness [67]. When turbine-induced turbulence is superimposed on the ambient values, turbulence intensity profiles vary according to whether they are measured in the near-wake (where a non-Gaussian (double-bell) wind profile is present [16]) or in the far wake where the wake is broadly Gaussian in form. Model and wind tunnel results [50] suggest that the peak in turbulence intensity in the near-wake is evident at heights 0.5 $D$ above hub-height, but this feature is less pronounced in the sodar observations (Fig. 5). Although there remain challenges in accurately estimating turbulence intensity from sodar measurements, the wake profile clearly has higher turbulence intensity than the non-wake profile. Applying the Frandsen model [68]:

$$I_{total}^2 = I_{ambient}^2 + I_{turbine}^2 \tag{3}$$

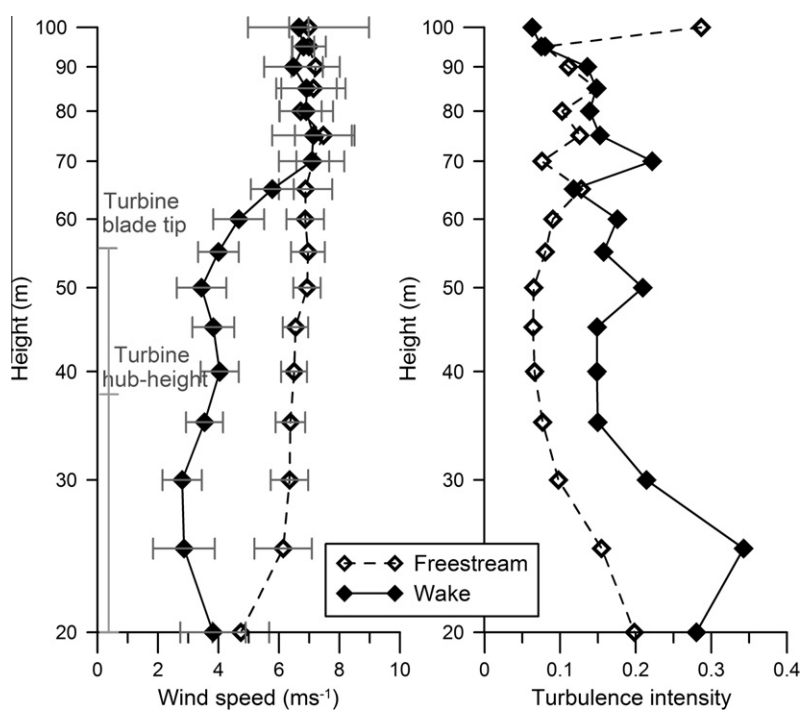


**Fig. 5.** Wind speed and turbulence profiles from an experiment at Vindeby using boat mounted sodar [16]. Turbulence intensity is calculated as the standard deviation of the horizontal wind speed divided by the horizontal wind speed in a 30 min period. The solid symbols denote the wake condition (at a distance of 2.8 $D$) while the open symbols show the free-stream values (both half hour averages). The gray bar on the left shows the original turbine hub-height and blade tips.

where $I_{total}$ is the total turbulence intensity, $I_{ambient}$ is freestream turbulence intensity, $I_{turbine}$ is the turbulence intensity added by the turbine to the sodar observations, and integrating $I_{total}$ across the rotor plane (20–70 m) indicates the wake influenced $I_{total}$ is 0.197, the freestream value ($I_{ambient}$) is 0.100, thus the turbine-added turbulence ($I_{turbine}$) is 0.169. Added turbulence intensity at hub-height for this case was previously estimated to be 0.087 (see Case 4 in Table 3 in [16]), which is due to the fact that the turbine-added turbulence is not maximized at hub-heights in the near-wake.

These examples illustrate the utility of data such as those contained in the Virtual Wakes Laboratory for examining characteristics of wind turbine wakes, but the majority of current users of VWL access the data for model evaluation. Use of appropriate metrics to further wake model evaluation and improvement are discussed in the next section again using examples from the VWL.

## 3. Tools for, and approaches to, evaluation of wake models

### 3.1. Wake model evaluation approaches and metrics

Much of the data presented in the Virtual Wakes Laboratory have previously been used in evaluation of wake and wind farm models of varying complexity. There is likely no one metric or variable that can serve to assess whether wake models are performing adequately, but a series of quantitative metrics should serve as a basis for assessing whether model performance is improving. Below we briefly describe the types of metrics and evaluation approaches that have been adopted to date, and their relative strengths and weaknesses.

As the demands for improved accuracy of wake models has increased and the need for characterization of conditions beyond the mean hub-height wind speed have become obvious, the level of sophistication of these wake model evaluation exercises has also increased. Nevertheless, the majority of wake model evaluation exercises that have been conducted to date have tended to focus on comparison of centerline velocity deficits at hub-height and, where quantitative evaluation has been attempted, have used metrics such as mean absolute error or root mean square error model vs. observations [65]. However, this approach reduces the evaluation of model skill to comparison of a single point on the wake profile for a single metric (wind speed). As shown in Fig. 6, beyond the near-wake region (i.e. for downstream distances beyond approximately 3–4 $D$), wakes are typically near-Gaussian in shape. While most wake models use a Gaussian or near-Gaussian distribution to depict the wake [69], some (e.g. WAsP) use a top-hat distribution, hence while the integrative momentum deficit in the wake may be correct in WAsP simulations, the maximum velocity deficit should be systematically underestimated relative to observations [65]. Thus, other studies have compared integrated variables across the rotor plane from models and observations. For example, boat-mounted sodar data at the Vindeby wind farm were used to evaluate range of models of varying complexity using a range of diagnostics including the relative velocity deficit and the cumulative velocity deficit over the wake profile [65]. Despite some obvious differences in the model types, this evaluation of model predictions for single wakes did not find any systematic bias for any particular model, regardless of its complexity. However, the absolute discrepancies between the models and the measurements were large. For the six wake models evaluated [65], the mean absolute error (expressed as a fraction of the free-stream wind speed) at hub-height between the predictions and the observations for single wakes in the six wake cases at downwind distances of 1.7–7.1 $D$ ranged from 11% to 17%. Other studies have evaluated wake models in terms of the power output from individual turbines. However, given power

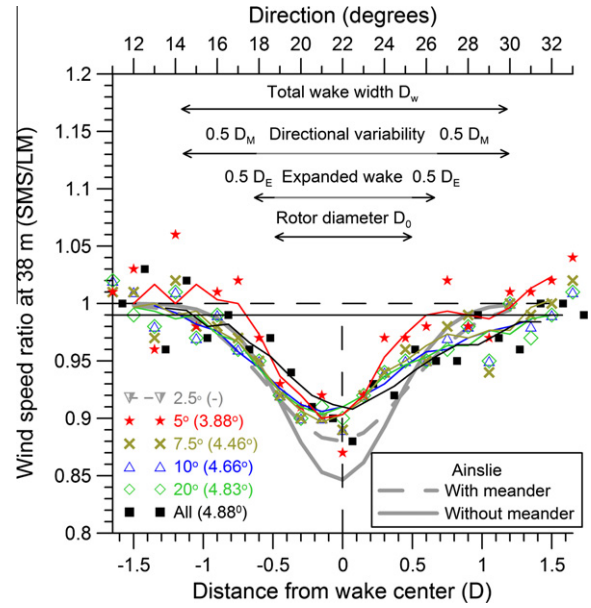


**Fig. 6.** The ratio of wind speed at Vindeby mast SMS to mast LM by direction. The colored symbols show averages of wind speed ratio in 1° direction bins while solid lines are running means. The color coding shown in the legend denotes the ratios conditionally sampled by the standard deviation of observed wind direction i.e. the black line and symbols show the observed ratios and the running means for all observations while the red symbols and line show those conditionally sampled for standard deviations less than ±5°. The number in brackets in the legend is the calculated standard deviation of direction for the sample shown i.e. using all observations the standard deviation of direction is 4.88°, while the standard deviation of direction for observations conditionally sampled for standard deviations of less than ±5° is 3.88°. Once the standard deviation of the direction is less than ±5° there are too few observations in each 1° direction bin to define the wake width. The lines at the top of the graph indicate the approximate contributions of $D_0$, $D_E$ and $D_M$ to the total wake width $D_W$ as indicated from Eq. (4). Also shown (as gray lines) on the graph are the wake profiles determined using the approximation of Ainslie [28] for a case with and without wake meandering.

production is determined by the integrated wind speed across the rotor plane [70], the accuracy of the turbine power curve is critical to use of modeled wind speeds to predicted power output.

A key issue in all model evaluation studies is the relatively small signal to noise ratio in wake detection. For the generation of sodar used in the Vindeby experiment contained in VWL and with the confounding influence of corrections for boat motion, the 30 min average measurements of wind speed and turbulence intensity were estimated to have accuracy of ±20%. In Fig. 5, the average wake wind speed from 20 to 65 m height is 3.88 $ms^{-1}$. Measurement uncertainty quantified as the average standard deviation of consecutive measurements within the 30 min periods is 0.80 $ms^{-1}$. The wake wind speed at 2.8 $D$ is 66% of the freestream wind speed, thus the reduction in velocity in the turbine wake is larger than the measurement uncertainty.

It is important to note that irrespective of the specific metric used to evaluate wake model performance for individual or multiple wakes a key source of uncertainty pertains to defining the free-stream wind speed and turbulence profiles (see Section 2) [65]. Even if accurate free-stream wind and turbulence profiles can be established, a second issue in comparing models and measurements is to reconcile the fundamental differences in the physical variables being measured and observed. As discussed in the following section, wake width can be objectively determined from observations for single and double wakes. It provides a useful tool for evaluating models (and quantifying the role of wake expansion vs. wake meandering), but also illustrates the challenges of make model-observations comparisons. Focusing on the single wake at Vindeby shown in Fig. 6, the center of the wake is evident for wind

**Table 2**
Wake widths for the case study from Vindeby shown in Fig. 6 expressed in degrees, meters and rotor diameters. Note these measurements pertain to a single wake case at Vindeby in which the distance between the turbine and the measurements is 8.6 *D*.

| | Width (°) | Width (m) | Width in rotor diameters, *D* |
|---|---|---|---|
| Turbine rotor diameter $D_0$ | 6.7 | 35.5 | 1.0 |
| Wake diameter with expansion ($D_0 + D_E$) but limited meandering (wake width when standard deviation of direction <5°) | 9 | 47.2 | 1.3 |
| Wake diameter including expansion and meandering ($D_0 + D_E + D_M$) (i.e. total wake width measured using all observations) | 16 | 84 | 2.4 |
| Ainslie wake diameter for $D_0 + D_E + D_M$ | 15 | 79 | 2.2 |
| Ainslie wake diameter excluding meandering | 12 | 63 | 1.8 |

directions of ~22° where the measured velocity at mast SMS is ~0.9 of the free-stream velocity. This wind direction is thus associated with direct flow from the upstream wind turbine to the meteorological mast. However, for slight variations in wind direction from 22°, the meteorological mast is impinged upon by a peripheral part of the wake. Thus a plot, like that shown in Fig. 6, can be developed by conditionally sampling the wind speed data for slight variations in the wind direction. Using an arbitrary threshold that the wind speed must exceed 0.99 of the freestream to represent the edges of the wake, the wake width using all observations at this downstream distance of 8.6 *D* is estimated to be 16° (which equates to a distance of 2.4 *D* or 86 m, see Table 2). Note that a challenge of applying the assumption of axisymmetric wakes to infer wake vertical profiles from wake widths (as determined herein) is that the vertical profiles are strongly impacted by the non-uniform inflow vertical wind speed profile.

For multiple wakes, and indeed wake effects at the wind farm scale, the model evaluation process becomes more complex. As indicated in [4], as wakes move through wind farms they are subject to inhomogeneity in the flow, and wakes from individual turbines impact the ground, impinge upon downstream turbines and merge with wakes from laterally displaced turbines. For sufficiently large wind farms the behavior of wind turbine wakes is additionally controlled by the characteristics of the whole boundary-layer (e.g., atmospheric stability, turbulence intensity, boundary-layer height, and wind shear). The VWL also provides case study data from the large offshore wind farms at Horns Rev and Nysted that can be used to quantify these effects and have already been used for wake model evaluation [48,71]. Wind farm efficiency is one integrative metric that can be used to evaluate model performance at the wind farm scale and is readily expressed using a range of error statistics [71].

The studies and approaches described above assume that power output is the desired quantity. If fatigue loads are to be modeled then the demands on model performance are even more stringent given the difficulties in measuring and modeling turbulence intensity [72]. The need to integrate power output and fatigue loading for wind farm optimization has prompted a more dynamic, case-study approach, with only limited evaluation of model skill [73].

### 3.2. Wake width as a metric of model performance

The actual width of a wind turbine wake is a function of three components;

(i) the turbine rotor diameter (this determines the volume of air from which momentum was extracted, $D_0$),
(ii) the wake expansion due to mixing in of higher momentum air at the lateral boundaries of the wake, and
(iii) meandering of the wake due to variations in the wind direction over the measurement period.

However, deconvoluting these terms has proved challenging and represents a major source of uncertainty in comparing observations and models. Using equation [1], and assuming a wake expansion coefficient of 0.05, the wake width at 8.6 *D* is predicted to be 1.86 $D_0$. From simple geometry we can convert this to a width in degrees (~12°). As indicated above this is similar to, but smaller than, the wake width derived from the observations. However, the observationally derived estimate is for all 10 min data periods without sub-selection for the degree of meteorological stationarity and thus the degree of wake meandering due to variations in the wind direction. Based on the discussion above, the wake width at a specific distance downstream $D_w$ can be assumed to consist of three additive components by expanding Eq. (1). As shown in Fig. 7, the total wake width includes not just the initial rotor diameter ($D_0$) and the expansion ($D_E$, where $D_E = 2kX$ as shown in Eq. (2)) but also an additional component that arises from the directional variability ($D_M$) that is also called wake meandering and arises from the variability of direction in the freestream flow:

$$D_W = D_0 + D_E + D_M \tag{4}$$

Using sub-sets of the Vindeby observations, selected with smaller standard deviations of wind direction, the width of the wake reduces because $D_M \to 0$. When the data are conditionally sampled to select only periods in which the standard deviation of wind direction <5°, the wake is approximately 9° wide. For the single wake case at Vindeby, at a downwind distance of 300 m, the original rotor diameter $D_0$ (35.5 m) corresponds to an angle $\alpha = 3.35°$ that would be observed as a wake width of 6.7° (Fig. 6). Assuming that the case in which the wind directional variability <5° represents the case where the wake expansion component from meandering is negligible (i.e. $D_M = 0$) for $D_W = 9°$, then from above $D_0 = 6.8°$ and $D_E = 2.2°$ (Fig. 6). Further, assuming that $D_E$ is invariant with the standard deviation of direction (although wake expansion depends on stability and turbulence [74]), the relative contribution of $D_M$ can be estimated (using the wake width for all observations $D_W = 16°$) from Eq. (4) $D_M = 7°$. In other words, assuming the

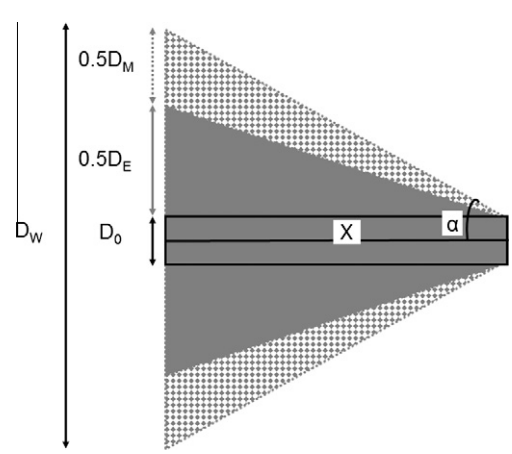


**Fig. 7.** Illustration of the components comprising the wake width at a distance *X* from the turbine.

assumption of linear expansion is approximately correct, for the single wake case at Vindeby, $D_M$ makes a larger contribution to total wake expansion than $D_E$. Thus, comparing observations that include both $D_E$ and $D_M$ with models that do not include variability in the wind direction (and thus set $D_M = 0$) may erroneously lead to the inference that $D_E$ is under-estimated.

Ainslie [28] proposed the following approximation to determine the contribution of wake meandering to the centerline wake velocity deficit:

$$v_c = v_0\left[1 + 7.12\left(\frac{X\sigma_\theta}{D_w}\right)^2\right]^{-0.5} \tag{5}$$

where $v_c$ is the velocity deficit including wake meandering, $v_0$ is the velocity deficit without meandering, $\sigma_\theta$ is the standard deviation of wind direction, and $X$ is downwind distance

Here, we invoke the assumption of a Gaussian wake shape to evaluate this approximation in terms of the implied meandering contribution to wake, based on the following:

The standard deviation of wind direction ($\sigma_\theta$) at Vindeby is 4–7° (Fig. 4) if calculated using [75]:

$$\sigma_\theta = sin^{-1}(\varepsilon)[1 + b\varepsilon^3] \tag{6}$$

where $b = \left(\frac{2}{\sqrt{3}}\right) - 1$, $\varepsilon = \sqrt{1 - \overline{\sin\theta}^2 - \overline{\cos\theta}^2}$

When expressed in radians $\sigma_\theta$ is comparable to values for turbulence intensity calculated as the ratio of the standard deviation of wind speed to freestream wind speed (0.07–0.16) for different heights and surface types [28], thus validating one of the assumptions employed by Ainslie [28]. Based on the observations from Vindeby summarized in Fig. 6, $D_w = 2.4\ D_0$, $X = 8.6\ D$, the centerline velocity deficit including meandering (expressed as SMS/LM) is 0.88. The increase in velocity deficit is 5% when determined from Eq. (5) for a case in which the meandering component is minimized (i.e. the maximum deficit in that case would equate to SMS/LM = 0.84). Using a Gaussian distribution to describe the wake form:

$$f(x) = \left[\frac{1}{(\sigma(2\pi)^{0.5}}\right]\exp\left[-\frac{(x-\overline{x})^2}{2\sigma^2}\right] \tag{7}$$

an increase in $f(x)$ computed at $x$ = centerline (i.e. the wake depth) as a result of setting $D_M = 0$, can be mapped onto the necessary reduction in wake width ($\sigma$) since the momentum deficit must be conserved.

Using this approach (see Fig. 6 and Table 2), the implied change in wake width due to wake meandering is smaller than the value for $D_M$ inferred from the observations. However, there are a number of caveats to this analysis and the inferences drawn there-from. This analysis is illustrative of a specific downwind distance (8.6 $D$), naturally, as the downwind distance increases, the impact of directional variability increases. Wake expansion ($D_E$) is strongly determined by the wind turbine thrust coefficient (and thus incident wind speed) and the prevailing atmospheric stability and turbulence (which may manifest themselves as increased directional variability). $D_M$ is determined in the empirical analysis as a residual term and thus is subject to considerable uncertainty. Nonetheless, this case study illustrates an additional reason why it is difficult to find an equal basis on which to compare models and measurements. Empirical wake models use expansion coefficients based on observations and these include elements of both wake expansion and meandering due to turbulence on all scales while most CFD (and LES) models include inflow turbulence that imparts only some part of directional variability [42].

Many comparisons of observations and model predictions assume that both are exactly observing/predicting the wake center and thus the maximum velocity deficit. In reality, a wider sector

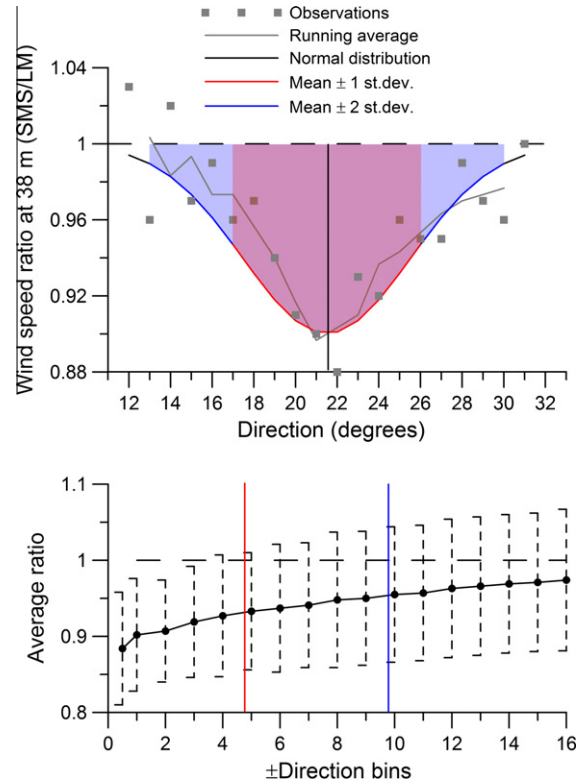


**Fig. 8.** Top: Wake width at Vindeby showing observations of the wind speed ratio (gray squares and line) compared with a fitted Gaussian distribution (black line). The area in red shows the observations that are included if the mean direction ± one standard deviation of direction in the calculation of the wind speed ratio, the area in blue includes observations included with the mean ± two standard deviations of direction. Below: The average wind speed ratio for the center of the wake (22°) ± the number of direction bins shown. The red line indicates the average at ± one standard deviation, the blue line the average at ± two standard deviations. The error bars on the ratio are ± one standard deviation (black dashed lines). (For interpretation of the references to colour in this figure legend, the reader is referred to the web version of this article.)

width has to be used to determine the wake velocity deficit from observations, in part because of observational uncertainty and atmospheric non-stationarity. The observational uncertainty derives from issues such as bias or offset in the wind direction measurement due to the initial calibration of the instrument (that is notoriously difficult to perform in the field) or drift. Either of these will result in an offset between the observed and modeled wake center. In addition, wind directional variability in the atmosphere is known to be related to stability conditions, indeed the standard deviation of wind direction is used in some versions of stability classifications, particularly in plume dispersion modeling [76]. Thus selection of the wind direction sector for conditionally sampling the observational data to determine parameters such as the total momentum deficit, or wake width, or the wake intensity (i.e. wake depth in terms of the velocity deficit) is also a critical determinant of model/measurement comparisons. For the example in Fig. 8, and following the logic expressed above (Eq. (5)), assuming a narrow central direction sector (i.e. 22° ± 0.5°) captures the largest velocity deficit, while expanding the directional sector (i.e. conditionally sampling over wind direction of 20–24°) decreases the size of the maximum velocity deficit derived from the observations. That is, if the velocity deficits are averaged over a larger wind direction sector, this leads to a smaller derived average velocity deficit. Assuming the wake conforms to a Gaussian distribution, approximately 68% of the wake lies within one standard deviation of the wake centerline (i.e. the wind direction is

within ±5°), 95% of the total wake is within two standard deviations and 99.7% within three standard deviations. Thus an alternative to using a fixed width approach to defining sectors for model validation is to use one standard deviation of the observed wind direction measurements or a fraction of the standard deviation to include a prescribed amount of the wake width. This is illustrated in Fig. 8 which shows the single wake at Vindeby for a downwind distance of 8.6 *D* marking the area for one and two standard deviations from the mean. Obviously the width of the wake varies with the distance from the turbine but so does the velocity deficit. As shown in Fig. 8, the average wind speed ratio (wake/freestream) at the center of the wake is 0.88 if the narrowest possible directional sector is chosen. Increasing the number of direction bins to 22° ± 1° increases the implied wind speed ratio to 0.90 and so on until including a wind direction sector of 22° ± 15° increases the ratio to 0.97 (i.e. if the data are conditionally sampled to center on a wind direction of 22° but include directions ±15°, the wake wind speed is 97% of the incident freestream wind speed). It is common to use conditional data sampling applying a screening threshold of ±2°, ±5° or ±10° to the wind direction sector included. Use of these data screening tools would decrease the wake wind speed to freestream ratio from 0.907 (in a sector with wind directions ±2° around the centerline) to 0.933 and 0.955, respectively. As indicated in Fig. 8, in this case choosing a wind direction ±5° is close to ±one standard deviation and ±10° close to two standard deviations. Thus, wake model evaluation studies must incorporate consideration of the wake shape, treatment of wind directional variability and incorporate consideration of the width of the direction sector used to compute the observed wake characteristics.

## 4. Concluding remarks

Accurate prediction of power losses from wind turbine wakes in large wind farms remains elusive. At present there are a number of approaches to modeling power losses due to wind turbine wakes in large wind farms that range in complexity, but all require further evaluation and refinement. Significant issues limiting the improvement of models are the lack of appropriate data for evaluation, limited application of evaluation metrics to quantify model skill and very limited attempts at attribution of model error. This paper outlines some of the issues involved in using different types of data for evaluating wind turbine wake modeling and shows how these data can be used to characterize wake properties using examples based on data from the open access Virtual Wakes Laboratory. The paper also describes some of the issues involved in using data to evaluate models, with a focus on wake width.

## Acknowledgements

The Virtual Wake Laboratory is funded in part by the National Science Foundation (#1067007) the Department of Energy (#DE-EE0005379), NREL through DOE Wind and Water Power Program (DE-AC36-08GO28308), the European Union (EERA-DTOC 282797) and is hosted by Indiana University. Data are provided by permission of Vattenfall, DONG Energy and the Middelgrunden Wind Cooperative. We would like to acknowledge the anonymous reviewers for their help in clarifying the paper.

## References

[1] Barthelmie RJ, Jensen LE. Evaluation of power losses due to wind turbine wakes at the Nysted offshore wind farm. Wind Energy 2010;13:573–86.
[2] Frandsen S, Thøgersen ML. Integrated fatigue loading for wind turbines in wind farms by combining ambient turbulence and wakes. Wind Eng 1999;23:327–39.
[3] Larsen GC. Offshore fatigue design turbulence. Wind Energy 2001;4(3):107–20.
[4] Barthelmie RJ, Hansen KS, Pryor SC. Meteorological controls on wind turbine wakes. In: Proceedings of the IEEE, 2012. doi: 10.1109/JPROC [accepted 5.06.12].
[5] Barthelmie RJ, Murray F, Pryor SC. The economic benefit of short-term forecasting for wind energy in the UK electricity market. Energy Policy 2008;36(5):1687–96.
[6] Politis ES et al. Modeling wake effects in large wind farms in complex terrain: the problem, the methods and the issues. Wind Energy 2012;15:161–82.
[7] Taylor GJ. Wake and performance measurements on the Lawson–Tancred 17 m horizontal-axis windmill. IEEE Proc 1983;130(A9):604–12.
[8] Hogstrom U et al. A field study of the wake behind a 2 MW wind turbine. Atmos Environ 1988;22(4):803–20.
[9] Taylor GJ. Wake measurements on the Nibe wind turbines in Denmark, 1990, National Power ETSU WN 5020.
[10] Hansen KS et al. Evaluation of test results from the two Danish Nibe turbines in European wind energy conference and exhibition proceedings vol. 2. Rome; 1986.
[11] Frandsen S et al. Measurements on and modelling of offshore wind farms; 1996. p. 101. doi: Risø-R-903(EN).
[12] Barthelmie RJ et al. Meteorological aspects of offshore wind energy – observations from the Vindeby wind farm. J Wind Eng Ind Aerodyn 1996;62(2–3):191–211.
[13] Højstrup J. Spectral coherence in wind turbine wakes. J Wind Eng Ind Aerodyn 1999;80:137–46.
[14] Schepers JG, Obdam TS, Prospathopoulos J. Analysis of wake measurements from the ECN Wind turbine test site Wieringermeer. EWTW. Wind Energy 2011;15:575–91.
[15] Lundsager P, Petersen H, Frandsen ST. The dynamic behaviors of the stall regulated Nibe A wind turbine. In: Measurements and a model of stall induced vibrations. Roskilde: Risoe National Laboratory; 1981. p. 70.
[16] Barthelmie RJ et al. Offshore wind turbine wakes measured by SODAR. J Atmos Ocean Technol 2003;30:466–77.
[17] Jensen L. Wake measurements from the Horns Rev wind farm. In: European wind energy conference; 2004. EWEA (on CD).
[18] Hasager CB et al. Remote sensing observation used in offshore wind energy. IEEE J Select Top Appl Earth Observ Remote Sens 2008;1(1):67–79.
[19] Christiansen MB, Hasager C. Wake effects of large offshore wind farms identified from satellite SAR. Remote Sens Environ 2005;98:251–68.
[20] Bingöl F, Mann J, Larsen GC. Light detection and ranging measurements of wake dynamics part I: one-dimensional scanning. Wind Energy 2010;13(1):51–61.
[21] Krishnamurthy R, Calhoun R, Fernando H. Large-Eddy simulation-based retrieval of dissipation from coherent doppler Lidar data. Bound-Layer Meteorol 2010;136(1):45–57.
[22] Christiansen MB, Hasager C. Using airborne and satellite SAR for wake mapping offshore. Wind Energy 2006;9:437–55.
[23] Hirth BD et al. Measuring a utility-scale turbine wake using the TTUKa mobile research radars. J Atmos Ocean Technol 2012;29(6):765–71.
[24] Kasler Y et al. Wake measurements of a multi-mw wind turbine with coherent long-range pulsed doppler wind Lidar. J Atmos Ocean Technol 2010;27(9):1529–32.
[25] Milborrow DJ. Wake and cluster research: past, present and future. Phys Sci, Measur Instrum, Manage Edu, Rev, IEE Proc A 1983;130(9):566–73.
[26] Crespo A, Hernandez J, Frandsen S. Survey and modelling methods for wind turbine wakes and wind farms. Wind Energy 1999;2:1–24.
[27] Mortensen NG et al. Getting started with WAsP 9. Roskilde, Denmark: Risø National Laboratory; 2007. p. 72. ISBN 978-87-550-3607-9 [353 topics].
[28] Ainslie JF. Calculating the flow field in the wake of wind turbines. J Wind Eng Ind Aerodyn 1988;27:213–24.
[29] Schlez W, Neubert A. New developments in large wind farm modelling. In: European wind energy conference; 2009. Marseilles.
[30] Lange B et al. Improvement of the wind farm model FLaP (Farm Layout Program) for offshore applications. Wind Energy 2003;6:87–104.
[31] Crespo A et al. Experimental validation of the UPM computer code to calculate wind turbine wakes and comparison with other models. J Wind Eng Ind Aerodyn 1988;27:77–88.
[32] Henneman B. Numerical aspects of the WAKEFARM program; 2003. ECN. p. 31.
[33] Sanderse B, van der Pijl SP, Koren B. Review of computational fluid dynamics for wind turbine wake aerodynamics. Wind Energy 2011;14(7):799–819.
[34] Réthoré PE et al. A CFD model of the wake of an offshore wind farm: using a prescribed wake inflow. J Phys Conf Ser 2007. . 75 p. 012047 (7 p.).
[35] Ivanell S et al. ACL modelling of wake interaction in Horns Rev wind farm. In: European offshore wind energy conference; 2009. Stockholm, September 2009.
[36] Politis ES et al. CFD modeling issues of wind turbine wakes under stable atmospheric conditions. In: European wind energy conference, 2009. Marseille, March 2009.
[37] Cabezón D et al. CFD modelling of the interaction between the Surface Boundary Layer and rotor wake. Comparison of results obtained with different turbulence models and mesh strategies. In: European wind energy conference and exhibition, 2009. Marseille, March 2009.
[38] Troldborg N et al. Numerical simulations of wake interaction between two wind turbines at various inflow conditions. Wind Energy 2011;14(7):859–76.
[39] Troldborg N, Sørensen JN, Mikkelsen R. Numerical simulations of wake characteristics of a wind turbine in uniform in flow. Wind Energy 2010;13:86–99.

[40] Ivanell S et al. Analysis of numerically generated wake structures. Wind Energy 2009;12(1):63–80.
[41] Jimenez A et al. Large-eddy simulation of spectral coherence in a wind turbine wake. Environ Res Lett 2008;015004:9.
[42] Churchfield MJ et al. A large eddy simulation of wind-plant aerodynamics. In: 50th AIAA aerospace sciences meeting, 2012. Nashville, Tennessee January 9–12, 2012.
[43] Churchfield MJ et al. A numerical study of the effects of atmospheric and wake turbulence on wind turbine dynamics. J Turbul 2012. http://dx.doi.org/10.1080/14685248.2012.668191.
[44] Jensen NO. A note on wind turbine interaction. Roskilde, Denmark: Risø National Laboratory; 1983. p. 16.
[45] Frandsen S et al. Analytical modelling of wind speed deficit in large offshore wind farms. Wind Energy 2006;9(1–2):39–53.
[46] Frandsen S et al. The making of a second-generation wind farm efficiency model-complex. Wind Energy 2009;12:431–44.
[47] Cabezón D, Migoya E, Crespo A. Comparison of turbulence models for the computational fluid dynamics simulation of wind turbine wakes in the atmospheric boundary layer. Wind Energy 2011;14(7):909–21.
[48] Barthelmie RJ et al. Modelling and measuring flow and wind turbine wakes in large wind farms offshore. Wind Energy 2009;12(5):431–44. http://dx.doi.org/10.1002/we.348.
[49] Barthelmie RJ et al. Wind speed gradients in the coastal offshore environment: Issues pertaining to design and development of large offshore wind farms. Wind Eng 2007;31(6):369–82.
[50] Vermeer L, Sørensen J, Crespo A. Wind turbine wake aerodynamics. Prog Aerosp Sci 2003;39:467–510.
[51] Schepers JG et al. Final report of IEA AnnexXVIII: Enhanced Field Rotor Aerodynamics Database; 2002, ECN-C-02-016: Petten. p. 353.
[52] Rettenmeier A et al. Wind field analyses using a nacelle-based LiDAR system. In: European wind energy conference; 2010.
[53] Wagner R et al. Power performance measured using a nacelle LiDAR. In European wind energy conference; 2011. Brussels.
[54] Hassan U, Taylor G, Garrad A. The dynamic response of wind turbines operating in a wake flow. J Wind Eng Ind Aerodyn 1990;27:113–26.
[55] Frandsen ST et al. Summary report: The shadow effect of large wind farms: measurements, data analysis and modeling. Roskilde: Risø National Laboratory/DTU; 2007. p. 34.
[56] Barthelmie RJ et al., Modelling and measurements of power losses and turbulence intensity in wind turbine wakes at Middelgrunden offshore wind farm. Wind energy; 2007. 10. doi: 10.1002/we.238. p. 217–28.
[57] Cutler NJ, Outhred HR, MacGill IF. Using nacelle-based wind speed observations to improve power curve modeling for wind power forecasting. Wind Energy 2012;15:245–58.
[58] Smaili A, Masson C. On the rotor effects upon nacelle anemometry for wind turbines. Wind Eng 2004;28:695–714.
[59] Frandsen ST et al. The generics of wind turbine nacelle anemometry. In: European wind energy conference; 2009.
[60] Ganader H et al. Medium term evaluation of meteorological conditions, power performance and loads on the first Swedish offshore wind farm at Bockstigen. In: European wind energy association offshore wind energy conference; 2001. Brussels.
[61] Lindelöw-Marsden P et al. Flow distortion on boom mounted cup anemometers. Risø-R-1738(EN): Risø National Laboratory; 2010. p. 39.
[62] Barthelmie RJ et al. Meteorological aspects of offshore wind energy: Observations from the Vindeby wind farm. J Wind Eng Ind Aerodyn 1996;62:191–211.
[63] Motta M, Barthelmie RJ, Vølund P. The influence of non-logarithmic wind speed profiles on potential power output at Danish offshore sites. Wind Energy 2005;8:219–36.
[64] Schlez W et al. ENDOW: Improvement of wake models within offshore windfarms. Wind Eng 2002;25:281–7.
[65] Barthelmie RJ et al. Comparison of wake model simulations with offshore wind turbine wake profiles measured by sodar. J Atmos Ocean Technol 2006;23(7):888–901.
[66] Jørgensen HE et al. Modelling offshore wind resources and wind conditions. In: Copenhagen offshore wind. Copenhagen, October; 2005.
[67] Barthelmie R et al. Ten years of meteorological measurements for offshore wind farms. J SolEnergy Eng 2005;127(2):170–6.
[68] Frandsen S, Thomsen K. Changes in fatigue and extreme loading when moving wind farms offshore. Wind Eng 1997;21:197–214.
[69] Larsen GC et al. Wake meandering: a pragmatic approach. Wind Energy 2008;11(4):377–95.
[70] Moriarty P, Barthelmie RJ, Frandsen ST. Universal benchmarks for wind turbine wake and wind farm models. In: Euromech wind turbine wakes. Madrid 20–22 October, 2009.
[71] Barthelmie RJ et al. Quantifying the impact of wind turbine wakes on power output at offshore wind farms. J Atmos Ocean Technol 2010;27(8):1302–17.
[72] Mücke T, Kleinhans D, Peinke J. Atmospheric turbulence and its influence on the alternating loads on wind turbines. Wind Energy 2011;14(2):301–16.
[73] Larsen TJ et al. Validation of the Dynamic Wake Meander Model for Loads and Power Production in the Egmond aan Zee Wind Farm. Wind Energy 2012. http://dx.doi.org/10.1002/we.
[74] Hansen KH et al. The impact of turbulence intensity and atmospheric stability on power deficits due to wind turbine wakes at Horns Rev wind farm. Wind Energy 2012;15(1):183–96. http://dx.doi.org/10.1002/we.512.
[75] Yamartino RJ. A comparison of several "single-pass" estimators of the standard deviation of wind direction. J Climate Appl Meteorol 1984;23(9):1362–6.
[76] Weber RO. Estimators for the standard deviations of lateral, longitudinal and vertical wind components. Atmos Environ 1998;32:3639–46.